Ultramicroporous Metal-Organic Frameworks and Porphyrin Linker Design toward Gas-based Applications

by

© Ellan K. Berdichevsky

A thesis submitted to the School of Graduate Studies in partial fulfillment of the requirements for the degree of Master of Science.

Department of Chemistry

Memorial University of Newfoundland

August 2022

St. John's, Newfoundland and Labrador, Canada

Abstract

Metal-Organic Frameworks (MOFs) are a class of materials characterized by their highly porous nature. MOFs are ordered structures made up of well-defined metal 'nodes' that are bridged to each other through coordinating organic 'linkers'. These frameworks have been an appealing area of research in recent years thanks to their numerous applications.

Regarding gas separation in MOFs, a conventional approach is to develop a material that has a high affinity for one gas of interest, and lower affinities for other gases that may appear in a mixture. A typical example is the removal of carbon dioxide from flue gas exhaust. MOFs have been developed that can strongly and selectively bind carbon dioxide while in the presence of gases such as nitrogen, oxygen, and nitrogen oxides, and even water vapour. These separations can be challenging when the gases to be separated are low in abundance (e.g., atmospheric sequestration) or when they cannot be bound selectively over other gases. An alternative approach to separation is a method that relies on the differences in molecular size of the gases in a mixture, so-called molecular sieving. Chapter 2 describes two such MOFs (**Zn_2M; M = Zn or Cd**), whose ultramicropores (pore width $< 0.7\,\text{nm}$) make them capable of molecular sieving. The crystal structures of these MOFs were examined at different temperatures (100 and 273 K) and with different solvent molecules in the pores (DMSO and methanol) to help better understand the structural effects on their gas adsorption and

separation properties. Critically, changing from Zn to Cd in the trimetallic node of the MOFs results in a sub-Å change in the pore opening. At the molecular scale, this change resulted in a drastic difference in gas adsorption between the two MOFs. $\mathbf{Zn_3}$ only allows carbon dioxide to enter its framework, whereas $\mathbf{Zn_2Cd}$ permits carbon dioxide, argon, nitrogen, and methane to enter the pores. The data suggest that $\mathbf{Zn_3}$ could be an excellent sieve for separating carbon dioxide from mixtures, even at environmental concentrations.

Regarding the synthesis of MOFs, one of the ways to obtain MOFs with new topologies and unique properties is to design novel organic linkers. One class of organic molecules that lends itself well to creativity and modification is porphyrins. As the ‘pigments of life’, porphyrins are found everywhere in nature and have been used in applications ranging from catalysis to optics to therapeutics, and of course have been used as linkers in MOFs. Porphyrins in MOFs offer an additional dimension to the tuneability of the framework, as the porphyrin linker itself can coordinate a metal through the central nitrogens, changing the properties of the framework without affecting its structure. To date, porphyrin linkers have been predominantly made to coordinate to MOF nodes through substituents on their *meso* methine regions. Porphyrin MOF linkers where the linking moieties extend from the β-positions are as of yet unknown, leaving plenty of room for exploration. Chapter 3 discusses the synthetic methods that could give access to these linkers, as well as the progress made towards these linkers. Although ultimately the desired porphyrins could not be isolated and used in MOF synthesis due to the delays associated with the COVID-19 pandemic, Chapter 3 illustrates that the chemistry works and puzzles out the synthetic route necessary to obtain β-subsituted porphyrin linkers.

To my parents, Marina and Konstantin.

Acknowledgements

A few years ago, I never would have thought that my graduate school journey would take me to the opposite side of Canada from my home back in Vancouver. Had it not been for my then supervisor Dr. Jeffrey Warren telling me about a certain Dr. Michael Katz doing cool materials chemistry research in Newfoundland, I don't think I ever would have made my way to this province. But I'm glad that I did.

First and foremost, I would like to thank my supervisor Dr. Michael Katz for his incredible mentorship and dedication. Throughout my degree, Mike encouraged me to think deeply about the finer details while keeping the bigger picture in mind. Being fellow SFU alumni, we could share memories and make references to things that only the two of us would understand. Mike really helped to make me feel like I was in my second home, and for that I thank him. A huge shout-out to the entire Katz research group who were there to support me when I needed help. Thank you in particular to my 'cubicle-mates'. Mason for the daily banter, stimulating scientific discussions, and ingenious problem solving. Amanda for always asking the right questions and having a work ethic that I could only strive for. Craig for his wild ideas and ability to make us all laugh. Thank you to everyone in the inorganic chemistry student office for creating a sense of collaboration and comradery.

I would like to thank my supervisory committee members, Dr. Christopher Kozak and Dr. Sunil Pansare. A sincere thank you to Dr. Céline Schneider on NMR and Dr. Jian-Bin Lin on XRD, whose expertise and facilities were invaluable to my research. Thank you to Dr. Graham Bodwell and Dr. Erika Merschrod for their examination of this thesis. Thank you to the Department of Chemistry and to the School of Graduate Studies for all the academic and financial support.

Lastly, I want to extend a heartfelt thanks to my partner, Yuka. Her positivity and work ethic motivated me to no end. She may not think she did much, but seeing your loved ones striving towards a goal only makes you want to work that much harder for your own.

Table of Contents

3 Linker Design towards Novel Porphyrinic MOFs 58

List of Tables

List of Figures

List of Schemes

List of Symbols and Abbreviations

δ	chemical shift
J	coupling constant
s	singlet
bs	broad singlet
d	doublet
dd	doublet of doublets
t	triplet
q	quartet
m	multiplet
Ac	acetyl
atc	1,3,5,7-adamantanetetracarboxylate
BCPP	5,15-bis(4-carboxyphenyl)porphyrin
BDC	1,4-benzenedicarboxylate
BET	Brunauer-Emmett-Teller

BHT	butylated hydroxytoluene
Bn	benzyl
BPDC	4,4’-biphenylenedicarboxylate
4,4’-bpy	4,4’-bipyridine
BTC	1,3,5-benzenetricarboxylate
btctb	4,4’,4”-[benzene-1,3,5-triyltris(carbonylimino)]trisbenzoate
BZ	Barton-Zard
CALF	Calgary Framework
CCS	carbon capture and sequestration
COF	covalent organic framework
DABCO	1,4-diazabicyclo[2.2.2]octane
DBU	1,8-diazabicyclo[5.4.0]undec-7-ene
DCDPP	5,15-bis(4-carboxyphenyl)-10,20-bis(4-pyridyl)porphyrin
DCM	dichloromethane
DDQ	2,3-dichloro-5,6-dicyano-1,4-benzoquinone
diH_2O	deionized water
DMF	*N*,*N*-dimethylformamide
DMSO	dimethylsulfoxide
dobdc	2,5-dioxido-1,4-benzenedicarboxylate

DSLM	Dual-Site Langmuir adsorption model
Et	ethyl
Fu	fumarate
H_2ox	oxalic acid
HKUST	Hong Kong University of Science and Technology
Htz	triazole
i-Pr	isopropyl
IAST	ideal adsorbed solution theory
ICA	isocyanoacetate
KAUST	King Abdullah University of Science and Technology
LJ	Lennard-Jones 12-6 potential
Me	methyl
MMM	mixed-matrix membrane
MOF	metal-organic framework
2,6-NDC	2,6-naphthalenedicarboxylate
$(NH_2)_2$BPDC	3,3'-diaminobiphenyl-4,4'-dicarboxylate
NMR	nuclear magnetic resonance
NU	Northwestern University
OEP	2,3,7,8,12,13,17,18-octaethylporphyrin

Pc	phthalocyanine
PCN	porous coordination network
PCP	porous coordination polymer
PIM	polymer of intrinsic microporosity
PMMA	polymethyl methacrylate
PSA	pressure swing adsorption
PVDF	polyvinylidene difluoride
PXRD	Powder X-ray diffraction
pyr	pyrazine
r.t.	room temperature
SSLM	Single-Site Langmuir adsorption model
t-Bu	*tert*-butyl
TBAPy	1,3,6,8-tetrakis(*p*-benzoato)pyrene
TCP	5,10,15,20-tetrakis(4-cyanophenyl)porphyrin
TCPC	5,10,15-tris(4-carboxyphenyl)corrole
TCPP	5,10,15,20-tetrakis(4-carboxyphenyl)porphyrin
Tf	triflyl
TFA	trifluoroacetic acid
THF	tetrahydrofuran

TLC	thin-layer chromatography
TosMIC	tosylmethyl isocyanide
TPP	5,10,15,20-tetraphenylporphyrin
TPyP	5,10,15,20-tetrakis(4-pyridyl)porphyrin
Ts	toluenesulfonyl
TSA	temperature swing adsorption
UiO	Universitetet i Oslo
XRD	X-ray diffraction
ZIF	zeolitic imidazolate framework

Chapter 1

Introduction

1.1 Porous Materials

A porous material can be described as a medium that contains accessible void spaces in its structure (pores). Examples of such materials vary widely, including natural zeolites,[1] microporous carbons,[2] porous liquids,[3] polymers of intrinsic microporosity (PIMs),[4] porous coordination polymers (PCPs),[5,6] covalent organic frameworks (COFs),[7] etc.[8,9] Porous materials have been the focus of numerous researchers for applications such as, but not limited to, gas storage,[10,11] gas separation,[12,13] gas sequestration,[14] catalysis,[15] drug delivery,[16,17] semiconductors,[18,19] fuel cells,[20] and nonlinear optics.[21]

1.1.1 Metal-Organic Frameworks

Metal-organic frameworks (MOFs; sometimes used interchangeably with PCPs), a ubiquitous class of porous materials characterized by their high surface areas and tunable nature, have increased in popularity over the last few decades.[22–25] MOFs are built from nodes and linkers. The nodes are metal ions or inorganic clusters, such as Cu^{2+}, Fe^{3+}, $[Zn_4O]^{6+}$, or $[Zr_6O_4(OH)_4]^{12+}$. Linkers are organic ligands (Figure 1.1) with two or more coordinating functionalities that bridge nodes to one another. These functional groups are often carboxylic acids or nitrogen-based donor groups (e.g., pyridine, imidazole, triazole), though linkers featuring phosphonates,[26] sulfonates,[27] and thiolates[28] have also been used in the synthesis of MOFs. By choosing different nodes and linkers (or even mixtures of linkers), diverse structures and properties can be obtained.

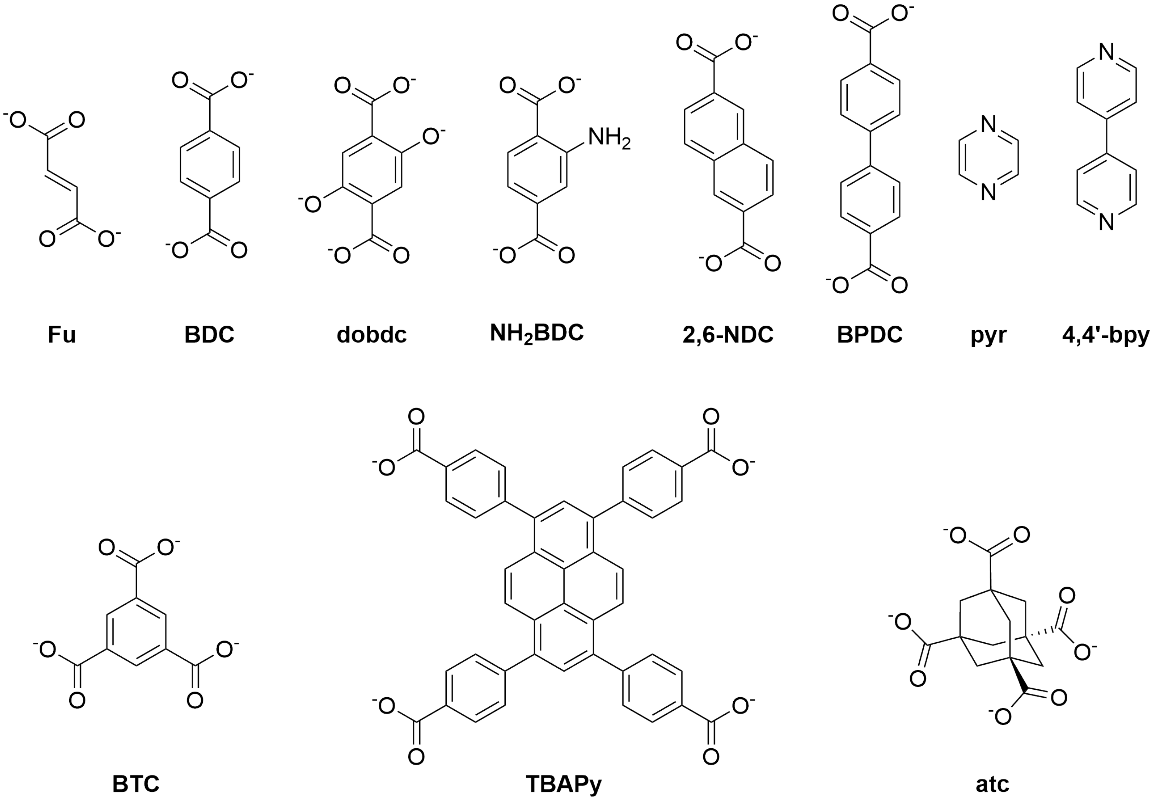

Figure 1.1: Examples of linkers used in MOF synthesis.

MOF synthesis is a rather straight forward operation, typically performed by dissolving a metal salt and the chosen linker in a solvent, optionally adding a 'modulator', placing the mixture in a sealed vessel, and heating over the course of hours to a few days. The modulator is a coordinating, monodentate acid, and it aids in the formation of a more pristine (i.e., phase-pure) material through competitive binding of the metal node.[29] This shifts the chemical equilibria within the solution, and reduces errors in the crystallization of the framework. While this solvothermal method is highly prevalent, MOF synthesis featuring microwave irradiation,[30] sonochemistry,[31] electrochemistry,[32] and mechanochemistry[33] have also been developed.

As a short aside, the naming conventions for MOFs may be somewhat confusing for those who are unfamiliar. There is no systematic naming system for MOFs like there is for organic molecules. Instead, one will frequently see an alphanumeric abbreviation; the letters can represent the university where the material was made (e.g., UiO–Universitetet i Oslo, MIL–Materials of the Institute Lavoisier, HKUST–Hong Kong University of Science and Technology), or the type of material (e.g., PCN–Porous Coordination Network, ZIF–Zeolitic Imidazolate Framework), and the numbers following help to further distinguish the materials. Although these abbreviations are arbitrarily assigned, and perhaps more frustrating is the fact that different abbreviations occasionally refer to the same MOF (the first MOF to be reported in the literature is MOF-5, though it is also called IRMOF-1), they allow MOF chemists to rapidly communicate the structure of their materials. For example, if HKUST-1 is mentioned in a report, our familiarity with this abbreviation tells us that the MOF is composed of Cu^{2+} nodes and benzene-1,3,5-tricarboxylate (BTC) linkers in a particular topology (Figure 1.2).

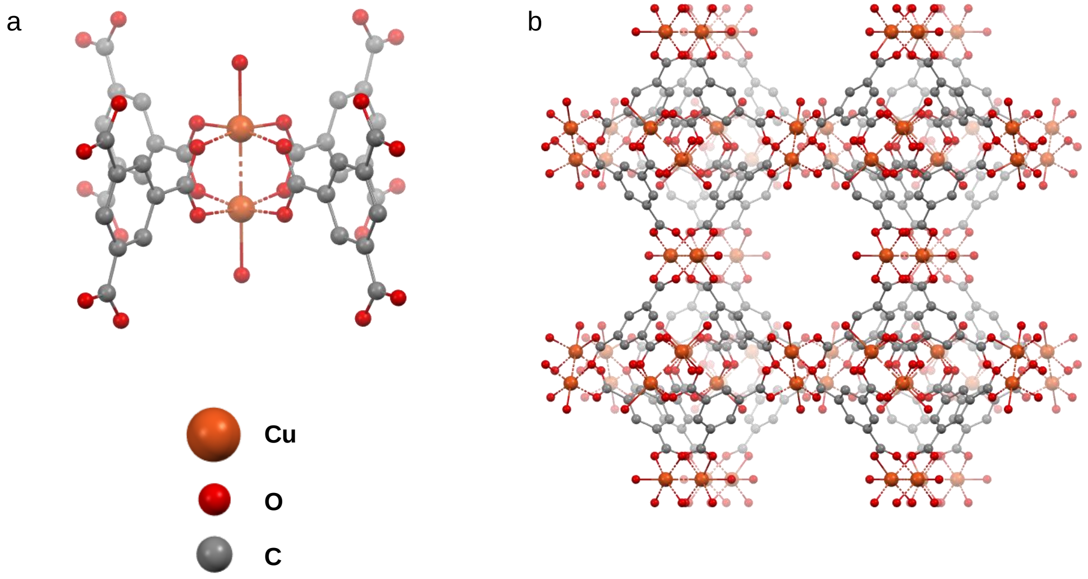

Figure 1.2: a) Node geometry of HKUST-1, with Cu^{2+} and BTC in a ‘paddlewheel’ ($Cu_2(COO)_4$) arrangement. b) 3D extended structure of HKUST-1.

1.2 Adsorption of Gases in MOFs

The process by which gas molecules adsorb, or ‘stick’, to the surface of a material like a MOF can be categorized in one of two ways: chemisorption or physisorption.[34] Chemisorption, as the name implies, involves the formation of chemical bonds between the adsorbate gas molecules and the adsorbent surface. This can lead to selective, strong binding of an analyte to the framework. This type of adsorption is commonly achieved by appending reactive functionalities within the pore of the MOF. The Katz group has shown that the zirconium-based MOF, UiO-66-NH_2, shows promise in the sequestration of nitrous acid (HONO), an atmospheric pollutant, at environmentally-relevant concentrations.[35] By a cooperative mechanism between the linker and the zirconium cluster, HONO reacts with the amine moiety to form a hydroxyl group and liberate water and dinitrogen (Figure 1.3a). In another study, Long et al. delved into the adsorption/desorption kinetics of CO_2 in various diamine-appended analogues of Mg_2(dobpdc) (also known as Mg-MOF-74; dobpdc = 4,4'-dioxidobiphenyl-3,3'-dicarboxylate; Figure 1.3b).[36] By tuning the alkyl-chain composition of the diamines, the thermodynamics and kinetics of the system could be optimized to allow for strong and fast adsorption at lower temperatures, while release of CO_2 could be achieved with only moderate temperature increase, making this MOF a good candidate for temperature-swing adsorption (TSA)-based processes.

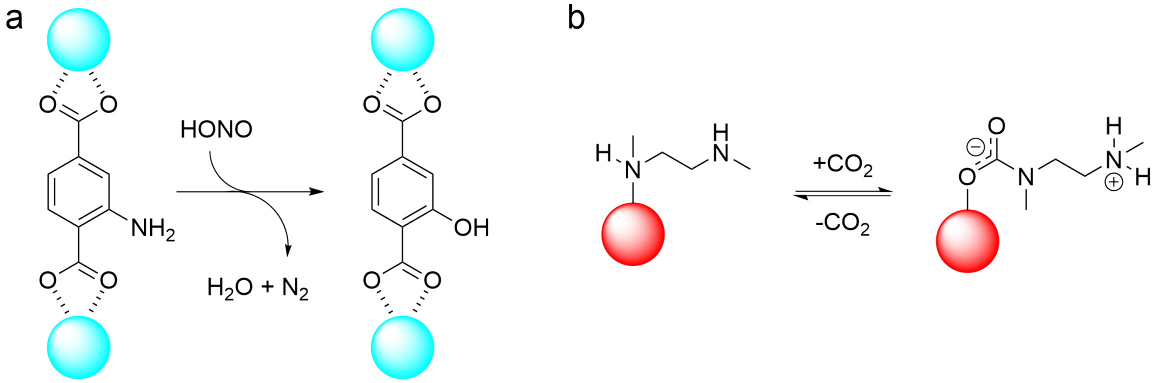

Figure 1.3: a) Chemisorption of HONO on UiO-66-NH_2. Cyan spheres represent the rest of the node. b) Chemisorption of CO_2 on m-2-m–Mg_2(dobpdc) (m-2-m = N,N'-dimethylethylenediamine). Red spheres represent MgO_5 units, which are arranged in an infinite chain.

On the other hand, physisorption relies on non-covalent (i.e., van der Waals) interactions between gas and framework. Physisorption is by far the mechanism of adsorption most often observed in porous solids, and can be tuned in MOFs by altering electronics and sterics through linker/node selection. With this tailorability in mind, Eddaoudi and co-workers designed a MOF, NbOFFIVE-1-Ni, for efficient adsorption of CO_2 gas.[37] The name of this MOF comes from the $NbOF_5{}^{2-}$ pillaring units, which join together square Ni^{2+}-pyrazine sheets. The efficacy of the material for CO_2 capture stems from the purpose-built pocket in which CO_2 molecules align themselves within the pores; the hydrogens of the pyrazine linkers point toward the electronegative oxygens of CO_2, while the electropositive carbon is positioned near the pillar's equatorial fluorines (Figure 1.4a). Recent work by Zhou et al. showed, through modification of the polarity and flexibility of pendant groups within a MOF pore, that adsorption, and ultimately separation, of acetone and methanol could be tuned.[38] Specifically, in their MOF built of Zn^{2+} and isophthalic acid analogues (Figure 1.4b), it was observed that ethoxyl pendant moieties possessed the best combination of properties to preferentially adsorb acetone at lower pressures.

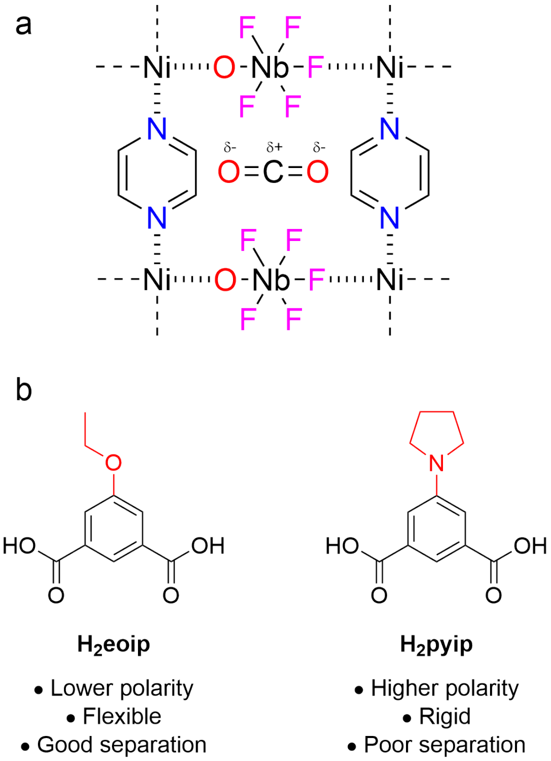

Figure 1.4: a) Adsorption pocket of CO_2 within NbOFFIVE-1-Ni. b) Linkers with different pendant groups, H_2eiop = 5-ethoxyisophthalic acid, H_2pyip = 5-(pyrrolidin-1-yl)isophthalic acid.

1.2.1 Enthalpy of Adsorption

The energy associated with the adsorption of molecules onto a surface allows for the determination of the affinity that a framework has for a particular analyte (Equation 1.1). Of particular interest in most studies is the enthalpy term, ΔH_{ad}, as gas adsorption is frequently an entropically disfavoured process. ΔH_{ad}, often referred to as the 'heat of adsorption', Q_{ST} (where $Q_{ST} = -\Delta H_{ad}$), gives a measure of the 'stickiness' of a gas to a surface.

$$\Delta G_{ad} = \Delta H_{ad} - T\Delta S_{ad} \tag{1.1}$$

While ΔH_{ad} can be measured directly via calorimetric methods,[39,40] the most common method is to fit gas adsorption isotherms to a model, from which the fitting parameters can be used to determine ΔH_{ad}. There are many adsorption models to choose from, though for the sake of simplicity, the popular Single-Site Langmuir adsorption model (SSLM) will be used as an example here. First, a brief derivation of SSLM from equilibrium principles. Take an adsorption process where a free gas A_B adsorbes onto a open adsorption site s_n to form an adsorbed species A_{ad}:

$$A_B + s_n \underset{k_d}{\overset{k_{ad}}{\rightleftharpoons}} A_{ad}$$

The rates of the corresponding forward and reverse reactions can be written as

$$r_{ad} = k_{ad} s P$$
$$r_d = k_d[A_{ad}]$$

where the forward adsorption process depends on the partial pressure of the gas, P, and the number of free adsorption sites, s, whereas the reverse desorption process depends on the amount of adsorbed gas, $[A_{ad}]$. At equilibrium, the forward and reverse rates are equal ($r_{ad} = r_d$) and thus an expression for the equilibrium constant K can be written as follows:

$$K = \frac{k_{ad}}{k_d} = \frac{[A_{ad}]}{sP} \tag{1.2}$$

Next, we need to know the total number of adsorption sites, s_0. Intuitively, the total number of sites would be equal to the sum of occupied and unoccupied sites:

$$s_0 = s + [A_{ad}] \tag{1.3}$$

By combining Equations 1.2 and 1.3, the following is obtained:

$$s_0 = \frac{[A_{ad}]}{KP} + [A_{ad}] = [A_{ad}]\left(\frac{1 + KP}{KP}\right) \tag{1.4}$$

Lastly, the fraction of occupied sites over the total number of sites is defined as the surface coverage θ, where $\theta = \frac{[A_{ad}]}{s_0}$. This leads to the familiar form of the SSLM given in Equation 1.5a. Oftentimes, MOF chemists will take θ to be the fraction of the quantity of gas adsorbed, q, over the saturation (maximum) quantity adsorbed, q_m, such that $\theta = \frac{q}{q_m}$ and the SSLM is rewritten as 1.5b.

$$\theta = \frac{KP}{1 + KP} \tag{1.5a}$$

$$q = \frac{q_m KP}{1 + KP} \tag{1.5b}$$

The SSLM, as with all models that attempt to describe gas adsorption, makes certain assumptions about the system and manner of adsorption.[34] The assumptions made by Langmuir are such that:

1. The adsorbent surface is homogeneous and contains only one type of adsorption site, such that only one molecule of adsorbate can occupy each adsorption site.
2. There are no interactions between adsorbate molecules as they are being adsorbed.
3. Adsorption occurs in a monolayer, where adsorbate molecules do not begin to stack and form multilayers until the previous monolayer is complete.

While assumptions such as these may be somewhat unrealistic at high surface coverage, where the number of free adsorption sites is low and it is more likely for gas molecules to stack on one another, this model is sufficient in fitting adsorption data at low loading (i.e., small θ). Other models such as the Brunauer-Emmett-Teller (BET) model are often used when adsorption is carried out to high surface coverage.[34] For many gases (e.g., CO_2, N_2, CH_4), their saturation pressure at room temperature is many times above atmospheric pressure, so adsorption experiments done at this temperature would almost always be considered to be occurring at low surface coverage and thus the SSLM can be applied.

With a model in hand that can fit isotherm data, it can then be used to calculate ΔH_{ad}. This is done by collecting a minimum of two isotherms, but often three, at different temperatures, usually 5–10 °C apart to avoid any change in the adsorption mechanism. Next, recall that in the SSLM, K is the equilibrium constant of this process and that it can be written in the form,

$$K = e^{\frac{-\Delta G_{ad}}{RT}} = e^{\frac{-(\Delta H_{ad} - T\Delta S_{ad})}{RT}} = Ae^{\frac{-\Delta H_{ad}}{RT}} \tag{1.6}$$

where R is the gas constant, and T is temperature. With the fits of the isotherm data and this expression for K, simply plotting lnK vs. $\frac{1}{RT}$ (i.e., a van't Hoff plot) can be done to obtain $-\Delta H_{ad}$ from the slope. In a more general case, where other isotherm models may be used, $-\Delta H_{ad}$ can be obtained by solving expression 1.7, or by using a common form of the Clausius-Clapeyron Equation 1.8 and plotting lnP vs. $\frac{1}{T}$ at a constant loading.

$$-\Delta H_{ad} = RT^2 \frac{\partial lnP}{\partial T}\bigg|_q \tag{1.7}$$

$$lnP = \frac{-\Delta H_{ad}}{R}\left(\frac{1}{T}\right) + \Delta S_{ad} \tag{1.8}$$

Now, a measure of the affinity of a particular gas to a material can be determined. In many cases, it is desirable to tune the magnitude of ΔH_{ad} to meet the requirements of a particular application. Physisorption tends to be in the range of -10 to $-40\,\mathrm{kJ\,mol^{-1}}$, while chemisorption may be $-80\,\mathrm{kJ\,mol^{-1}}$ or larger.[37]

1.3 Gas Separation in MOFs

The process of separating one gas from a complex mixture is of great importance both environmentally (e.g., carbon capture and sequestration (CCS) and desulfurization)[12,41] and economically (e.g., purification of commodity chemicals and fuels).[42] However, high efficiency and efficacy of these separations remain a challenge. Porous materials such as MOFs are an appealing solution, as the kinetics and thermodynamics of analyte adsorption onto the framework can be tuned through pre-synthetic (e.g., choice of node/linker, modifying synthetic procedures) and post-synthetic (e.g., composite mixtures, membrane incorporation)[43] methodologies.

For separations where the gas being adsorbed is to be later released (e.g., a purified commodity gas), a balance must be struck such that analyte affinity is high enough to afford good selectivity, while the energy to regenerate/use the material is not overly high. For capture/sequestration of gases (e.g., pollutants/toxic gases), oftentimes a high analyte affinity (high Q_{ST}) is prioritized over material regeneration. The latter application typically requires chemisorption, while the former is often performed by physisorption. In general, separation processes can be split into two categories: thermodynamic separations and kinetic separations.

1.3.1 Thermodynamic Separation

Predominantly thermodynamic separations are those that rely on a difference in adsorption enthalpies between the different analytes in a mixture. Simply put, taking an equal-parts mixture of two gases, the gas with the greater adsorption enthalpy (i.e., more exothermic) would adsorb onto the material preferentially over the other gas, and thus would be separated from the mixture. A common example would be the separation of CO_2 from N_2. In practice, CO_2 is already considered a 'stickier' gas than nitrogen, as can be rationalized by its higher boiling point (195 K vs. 77 K for N_2) and larger electric quadrupole ($-13.4 \times 10^{-40}\,\mathrm{C\,m^{-2}}$ vs. $-4.72 \times 10^{-40}\,\mathrm{C\,m^{-2}}$ for N_2).[44] This 'stickiness' can be further exploited through open metal sites or Lewis-basic groups within a MOF,[45,46] creating a greater difference in adsorption enthalpies between CO_2 and N_2, and ultimately separating them.

1.3.2 Kinetic Separation

Predominantly, kinetic separations take advantage of a difference in diffusivity between component gases in a mixture. For example, take a mixture of propane (C_3H_8) and propene (C_3H_6), the separation of which is relevant for the petrochemical industry. Chen and co-workers have shown that a microporous MOF, ELM-12 ($Cu(bpy)_2(OTf)_2$), displays highly effective kinetic separation of these two gases, even though the adsorption uptakes are similar ($60\,\mathrm{mg\,g^{-1}}$ and $62\,\mathrm{mg\,g^{-1}}$ for propane and propene, respectively).[47] The authors attribute the faster diffusion of C_3H_6 (and complementary slow diffusion of C_3H_8) to the 2D-zigzag channels of the framework, whose size better matches the molecular size of C_3H_6. In a breakthrough experiment, where a MOF is packed into a column and gas is flowed through to test real-world separation behaviour, the authors observed an early breakthrough (i.e., gas exiting the column) of C_3H_8, whereas C_3H_6 was retained much longer in the column. This implies that C_3H_8 is primarily moving *around* the MOF particles as that would be the path of least resistance, while C_3H_6 is diffusing into the pores and is retained in the MOF.

1.3.3 Ideal Adsorbed Solution Theory

In an effort to evaluate and compare adsorbents for separation applications, a common practice is to calculate theoretical separation selectivities. This is done by using Ideal Adsorbed Solution Theory (IAST), developed by Myers and Prausnitz.[48] IAST is reminiscent of Raoult's law, whereby it treats gases adsorbed on a surface as an ideal mixture, and the amount of a particular gas adsorbed is proportional to the mole fraction of that gas in the bulk (Equation 1.9a). In the equations below, P is the total pressure, P_i^o is the equilibrium pressure of pure component i, y_i and x_i are the mole fractions of component i in the bulk gas and adsorbed phases, respectively, which may then be related to the spreading pressure, π_i, by Equation 1.9b. Spreading pressure at the gas–surface interface can be thought of as the opposite to what is know as surface tension at a liquid–air interface; surface tension acts to minimize the surface area of the interface, while spreading pressure acts to maximize the surface area. By taking single-component (pure) gas adsorption isotherms and fitting them to an appropriate model, F_i, such as the SSLM described above, spreading pressure π_i for each component i is obtained.

$$Py_i = P_i^o x_i \tag{1.9a}$$

$$\pi_i = \frac{RT}{A} \int_0^{\frac{Py_i}{x_i}} \frac{F_i(P)}{P} \partial P \tag{1.9b}$$

$$S_{a/b} = \frac{x_a/x_b}{y_a/y_b} \tag{1.9c}$$

In the end, the goal is to take a given gas mixture composition (such that $\sum y_i = 1$), and predict the adsorbed quantities (i.e., x_i) of each component. This requires numerically solving a large system of equations, so it is often performed using purpose-designed software, such as IAST++ or pyIAST.[49,50] From this, the separation selectivity of a mixture can be estimated (Equation 1.9c, where $S_{a/b}$ is the selectivity of component a over component b). Materials with large $S_{a/b}$ values, in the range of 100s–1000s, are promising for the efficient separation of gases, though values that are too large may be more representative of a system that deviates from the ideality assumed by IAST, and should be taken with a grain of salt. Furthermore, it should be noted that selectivities calculated through the use of IAST are *adsorptive* selectivities, as they are derived from adsorption isotherms. Other methods, both computational and empirical that involve determining gas diffusivities, are available when the mechanism of separation is not necessarily based on thermodynamic processes.[51,52]

1.4 Motivation

1.4.1 Molecular Sieving

In addition to the separation methods mentioned in Section 1.3, there is another mode of separation that could be said to take the idea of kinetic separation to the extreme. Given a binary gas mixture, it would be noticed that in the majority of cases the two gases differ in molecular size, even if only by a few tenths of an angstrom. In much the same way that a tennis ball would not fit through a golf ball-sized hole, precise design of pore openings (apertures) in MOFs would allow for the separation of gases by completely excluding a species from entering the MOF. This method of separation, termed ‘molecular sieving’, can allow for highly selective separations, even when a gas being separated has similar framework affinity as other constituents of the mixture, or is in low abundance.

On the subject of molecular size, often in MOF-based gas separation literature, the reader will come across so-called 'kinetic diameters' of gases. These dimensions are then used to determine the appropriate size for a pore aperture towards separation.

$$\phi(r) = 4\epsilon\left[\left(\frac{\sigma}{r}\right)^{12} - \left(\frac{\sigma}{r}\right)^{6}\right] \tag{1.10}$$

The kinetic diameters of many common gases were tabulated in the mid 20th century by Breck,[53] found by applying both his own data and that of his contemporaries to the equation of the Lennard-Jones 12-6 (LJ) potential (Equation 1.10). The LJ potential describes the attractive and repulsive interactions of two species as they approach one another.[54] In this equation, ϵ is a constant and relates to the depth of

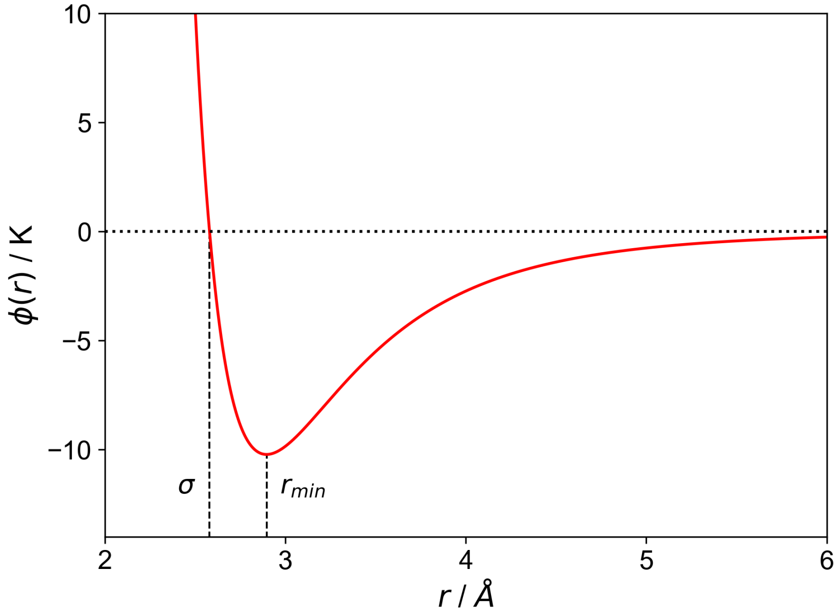

Figure 1.5: Graph of the Lennard-Jones 12-6 potential for helium, where $\epsilon = 10.22$ K, $\sigma = 2.58$ Å, and $r_{min} = 2.9$ Å.

the minimum of $\phi(r)$, r is the distance between the two species, and σ is the kinetic diameter such that $\phi(r) = 0$ and $r_{min} = 2^{1/6}\sigma$. Diameters of certain gases are given in Table 1.1, column one. These are the diameters often seen discussed in the literature, though reference to Breck is frequently omitted. More importantly, the accuracy and reliability of these values are rarely questioned. For example, in Breck's original calculations using the LJ potential, the diameter of CO_2 was found to be 4.05 Å. However, this contradicted his experimental work with zeolite adsorbents, where a particular adsorbent (zeolite KA) would adsorb CO_2 but not N_2. This led Breck to use a different r_{min} (i.e., the minimum Pauling width, 3.7 Å) in his calculations to obtain a diameter for CO_2 of 3.3 Å, which more favourably agreed with empirical results. While the lower value is likely nearer to the true kinetic diameter, such arbitrariness in the calculations should be avoided. More recently, others have also taken issue with the diameters tabulated by Breck, and have set out to provide more precise values.

In 2008, Dal-Cin commented on the accuracy of the original Breck diameters during his re-examination of gas diffusion in polymeric membranes.[55] While many of Breck's reported diameters are adequate, all the values suffer from a low number of significant figures, and in particular the diameters of CO_2, N_2, CH_4, and O_2 were questioned. Take for example the decision to use the Pauling width of CO_2 to obtain a result which better agrees with experimental observations. Applying the same treatment to N_2 (minimum Pauling width of 3.0 Å) would give a kinetic diameter of 2.7 Å, making it smaller than CO_2 and inconsistent with Breck's hypothesis that zeolite KA excludes N_2. Thus, in order to obtain kinetic diameter values of higher precision and accuracy, Dal-Cin took a statistical error analysis approach, which he applied to the Robeson upper bound, a theoretical upper bound on gas-pair separation in permeable polymer membranes. Simply put, the Robeson upper bound describes how membranes with high selectivity for a particular gas must then also have low diffusivity (slow kinetics), while high diffusivity membranes must sacrifice gas selectivity. It was found that the slope of the upper bound also correlates well with the difference in kinetic diameters between a particular gas pair. The revised kinetic diameter values are shown in Table 1.1, column two. A key revelation that is particularly poignant regarding the design of new molecular sieving materials is the change in kinetic diameters of CO_2 and O_2. CO_2 being somewhat larger (from 3.3 Å to 3.43 Å), along with N_2 being marginally smaller, means that the margin for pore aperture design is smaller than previously thought for this gas pair. With the second largest change, the new O_2 diameter means it may in fact be smaller than CO_2, which is an important consideration when looking at sieving separations of complex, multi-component gas mixture. These new kinetic diameters, while only few have been re-examined compared to Breck's original list, give increased precision and are more consistently obtained than the previous values.

Table 1.1: Kinetic diameters of select gases. σ_B are kinetic diameters tabulated by Breck, σ_R are kinetic diameters calculated via correlation with the Robeson upper bound. σ_QM are kinetic diameters calculated via quantum mechanical methods by Jiang in 2014, which show reasonable agreement with those obtained by Dal-Cin.[56]

	σ_B / Å	σ_R / Å	σ_QM / Å
He	2.60	2.55488	2.557
H_2	2.89	2.83406	2.877
CO_2	3.30	3.42667	3.469
O_2	3.46	3.37414	3.340
N_2	3.64	3.58760	3.578
CH_4	3.80	3.88178	4.046

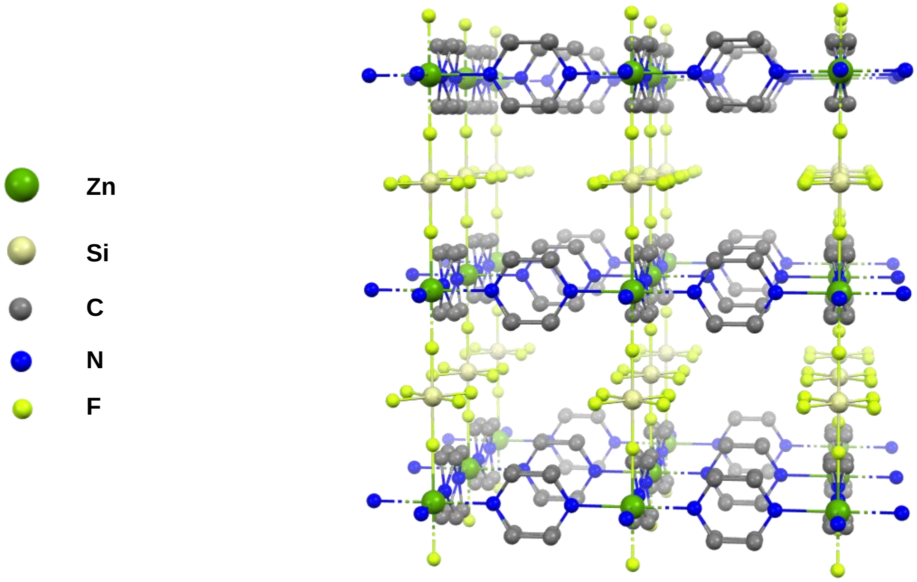

Figure 1.6: 3D extended structure of SIFSIX-3-Zn. The pyrazine pillars show slight disorder. H atoms have been omitted for clarity.

A pioneering example of MOFs designed for molecular sieving is the SIFSIX family. The predecessors to NbOFFIVE family of MOFs mentioned previously in Section 1.2, SIFSIX MOFs are constructed via metal dications (e.g., Zn^{2+}, Cu^{2+}), hexafluorosilicate dianions (from which the name of this MOF family is derived), and linear nitrogen-based pillars (Figure 1.6). The resulting pillared square grids have easily defined channels, which can be rationally tuned by substitution of the pillar or the metal ion, and thus can be tailored to specific separations. In 1995, Zaworotko and Subramanian reported the first structure of this family, $Zn(4,4'\text{-bpy})_2(SiF_6)$ (with work partly conducted at the MUN Grenfell campus!).[57] Later, Kita et al. presented a contracted analogue, $Zn(pyr)_2(SiF_6)$, whose 4.5 Å-wide channels were shown to strongly adsorb H_2 due to their small size and greater gas—framework interaction. Moreover, size-exclusion effects were noted for the separation of alcohol vapours, where diffusion of *i*-PrOH was hindered in comparison to MeOH and EtOH.[58] Further work motivated by the separation of small gas molecules has since lead the groups of Zaworotko and Eddaoudi to design SIFSIX analogues with even smaller channels: SIFSIX-3-Ni ($Ni(pyr)_2(SiF_6)$) and SIFSIX-3-Cu ($Cu(pyr)_2(SiF_6)$), with channel widths of 3.8 and 3.5 Å, respectively.[59,60] SIFSIX-3-Cu, with its particularly restrictive channel width, attains an impressive level of selectivity for CO_2 over N_2 (S_{CO_2/N_2} of 10500, derived from column breakthrough). In addition, new materials related to SIFSIX with varied anions such as ${CrO_4}^{2-}$, ${MoO_4}^{2-}$, and ${WO_4}^{2-}$ have also been synthesized.[61,62]

While development of MOFs for molecular sieving has progressed, there remains a tendency to frame their use in separations as an adsorptive one. Although their often purposefully designed small pore apertures would completely exclude one species from another as a sort of filter, the capacity and affinity towards the gas that enters the framework is frequently emphasized. This is likely a result of MOFs being the target of temperature- and pressure-swing adsorption (TSA and PSA) processes, which are reliant on the working capacity of the MOF to be able to cycle between capture and release of an analyte. However, considering how they might function purely as filters, it should be noticed that for molecular sieving MOFs the capacity is not the most important metric, but instead the diffusivity through the framework becomes the main driver for separations. This would allow MOFs to perform separations in low analyte concentration or low analyte affinity situations very efficiently.

In Chapter 2, the adsorptive properties of two MOFs with very small pores which may be of particular interest for CO_2 separation are described. The intended goal is to better understand adsorption and molecular sieving in these small pore MOFs by examining the effects of minute pore aperture changes on their observed properties.

1.4.2 Porphyrinic MOFs

A particular sub-category of MOFs that have garnered interest for their catalytic,[63] optical,[64] and pharmaceutical[65] properties are porphyrinic MOFs (Por-MOFs), so called as they feature a porphyrin as their organic linker. Porphyrins, with their ubiquitous roles in nature, would undoubtedly be brought into MOF chemistry, owing to the decades of development on their synthesis and modification.[66] In 1991, Robson reported on the first example of a 3-dimensional coordination framework to feature porphyrin linkers.[67] The framework was formed from palladium 5,10,15,20-tetra(4-pyridyl)porphyrin (TPyPPd) and monoatomic Cd(II) centers. Soon after, the same group added two more frameworks to this family, featuring metalloporphyrin linkers TPyPCu and TCPCu (TCP = 5,10,15,20-tetrakis(4-cyanophenyl)porphyrin) and monoatomic Cu(I) nodes.[68] Since then, the field of Por-MOFs has seen rapid expansion and development. Some examples of porphyrin linkers seen today are given in Figure 1.7, with the most common by far being 5,10,15,20-tetrakis(4-carboxyphenyl)porphyrin (TCPP). Some example MOFs featuring TCPP are the zirconium-based PCN-222,[69] MOF-525,[70] NU-902,[71] the iron-based PCN-600,[72] and vanadium based V-MOF-10.[73] Furthermore, porphyrin linkers may also coordinate a metal in the center of the porphyrin ring, increasing the overall design space for tuning Por-MOFs to specific applications.[74] Recently in their exploration of non-standard porphyrinoid linkers, Shangqian Ma and coworkers have shown how the development of a corrole-type linker, along with metallation of the linker, can produce a MOF with both good stability as well as activity towards catalysis.[75] 5,10,15-Tris(4-carboxyphenyl)corrole (TCPC) is, at first glance, an unusual MOF linker, as it is relatively less symmetric than typical linkers. Indeed, greater symmetry is often preferred as the resulting MOF topology can be more intuitively predicted, though by investigating lower-symmetry

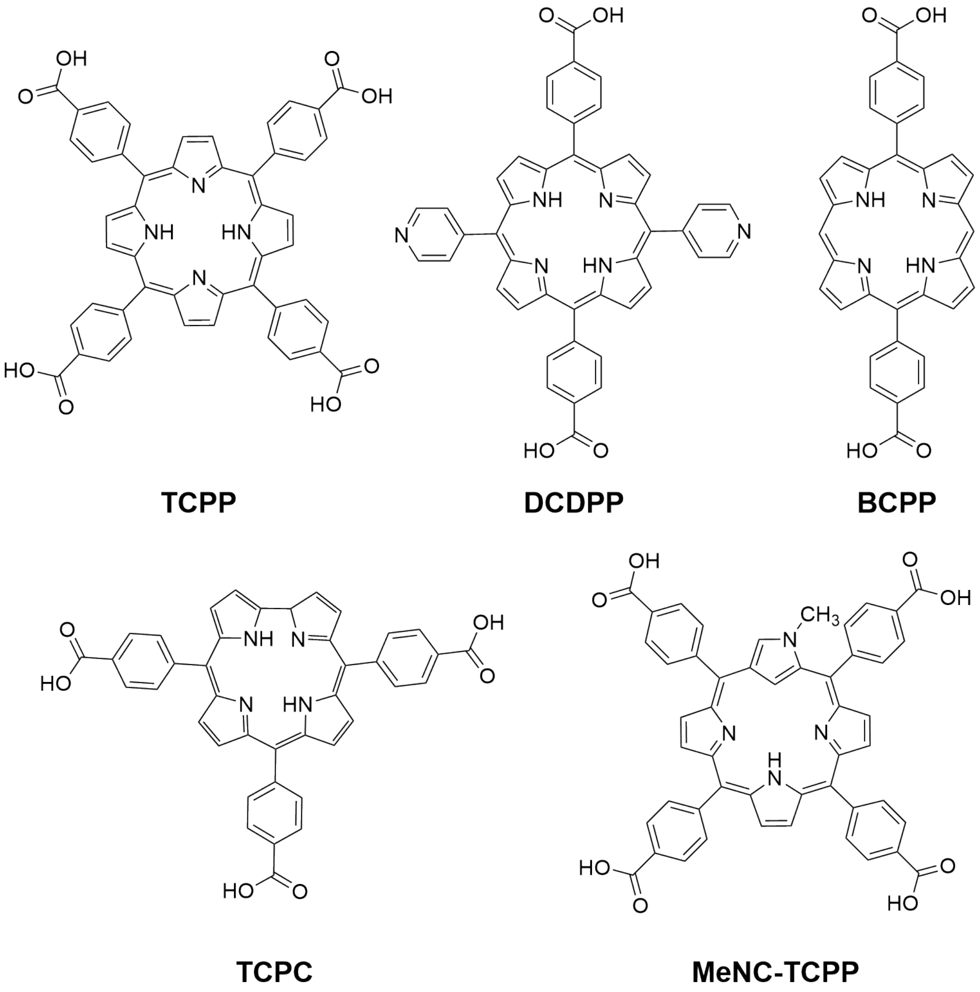

TCPP **DCDPP** **BCPP**

TCPC **MeNC-TCPP**

Figure 1.7: Examples of porphyrins (and related molecules) used as linkers in MOFs.

linkers, new and unexpected structures with interesting properties may be found. TCPC was reacted with a zirconium salt to form Corrole-MOF-1, with the structural formula $Zr_6(\mu_3\text{-}O)_4(\mu_3\text{-}OH)_4(OH)_3(H_2O)_3(TCPC)_3$. Taking advantage of the open coordination site in the corrole, Corrole-MOF-1(Fe) was synthesized using the iron-metallated corrole as the linker. This resulted in not only a robust framework, but also an efficient heterogenous hetero-Diels-Alder catalyst when the iron sites were incorporated.

Although the prospects are promising, exploratory work on Por-MOFs with novel linkers is rather limited, with many reports often focusing on the same few known MOFs. Furthermore, although there is a rich body of literature on porphyrin synthesis, porphyrin linkers for MOFs seem to be confined to only those which are modified at the interpyrrolic methine (*meso*) carbons. Perhaps one of the few exceptions to this would be the foray of the physical-organic group of Furuta into the realm of MOFs. Applying their expertise in porphyrinoid chemistry, they successfully synthesized MeNCP-MOF-525, a MOF featuring the N-confused porphyrin linker, MeNC-TCPP (Figure 1.7).[76] This MOF, analogous to MOF-525, exhibited noticeably different optical properties to the parent MOF, a result of the perturbed π-electron system of the N-confused porphyrin core.

In an effort to expand the repertoire of linkers for Por-MOFs, Chapter 3 of this thesis will provide some insight on the available synthetic strategies towards as yet unexplored porphyrinic linkers, and progress towards some such linkers is reported. In particular, focus is turned to linkers where the coordinating moieties (oftentimes phenylcarboxylate groups) would be on the pyrrolic backbone, which are referred to as the β-positions (Figure 1.8). Such β-substituted porphyrin linkers are as of yet unseen in the MOF literature, though they are the predominant type of substituted porphyrin found naturally, such as the O_2-binding site of hemoglobin and the enzymatic active site of cytochrome P450 monooxygenases.[77]

Although the intended synthesis of porphyrinic linkers/MOFs was unable to be completed due to delays caused by the COVID-19 pandemic, it is nonetheless important to highlight the significance of this endeavor. Not only could interesting topologies arise in these β-Por-MOFs, but due to their modified electronic structure, such MOFs could exhibit biomimetic catalytic activity that is otherwise unattainable using typical, *meso*-substituted linkers. Furthermore, with the ‘linking’ aspect of the

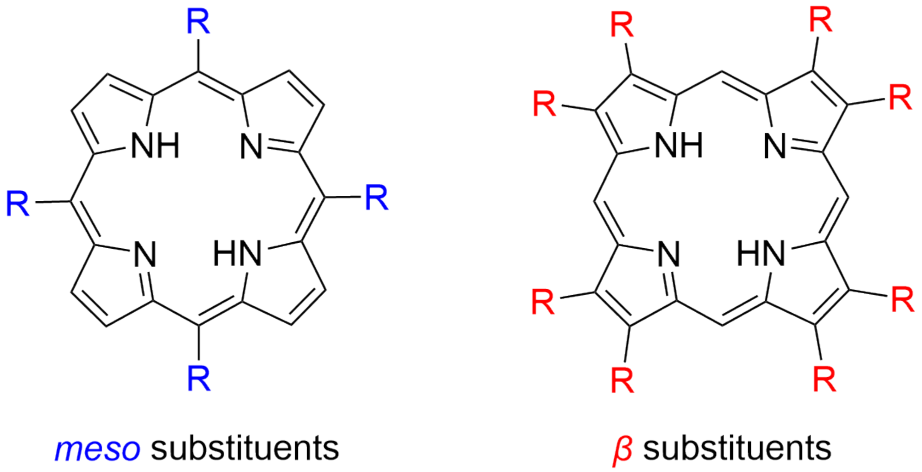

Figure 1.8: Possible substituent positions on the porphyrin macrocycle.

linker left to the pyrrole subunits, the gas adsorption behaviour of the Por-MOFs can be tuned by using different aldehyde precursors to modify the now-free *meso* positions (see Chapter 3). Substituents in these positions are much closer to the center of the porphyrin, so in the case of metallated linkers, the properties of the porphyrin metal center could be extensively tuned within the Por-MOF.

Co-authorship Statement

A portion of the following chapter appears in:

E.K. Berdichevsky[a]; V.A. Downing[a]; R.W. Hooper[b]; N.W. Butt[a]; D.T. McGrath[a]; L.J. Donnelly[a]; V.K. Michaelis[b]; M.J. Katz[a]* Ultra-High Size Exclusion Selectivity for Carbon Dioxide from Nitrogen/Methane in an Ultramicroporous Metal-Organic Framework. *Inorganic Chemistry*, 2022, **61**, 7970-7979.

[a] Department of Chemistry, Memorial University of Newfoundland, 230 Elizabeth Avenue, St. John's, Newfoundland and Labrador, A1C 5S7, Canada

[b] Department of Chemistry, University of Alberta, 11227 Saskatchewan Drive, Edmonton, Alberta, T6G 2G2, Canada

Author Contributions: EKB contributed to the majority of the article through manuscript writing, collection and analysis of data, and interpretation of results. VAD, DTM and LJD developed the initial synthesis of the materials and collected preliminary gas adsorption data. NWB contributed to the synthetic development and collection of time-resolved solution NMR. RWH and VKM collected and interpreted solid-state NMR data. MJK directed the work, collected and solved all the crystallographic data, and wrote the manuscript.

Chapter 2

Carbon Dioxide Separation by Ultramicroporous MOFs

2.1 Introduction

Separation of carbon dioxide (CO_2) from various industrial gas streams is necessary to curb its overall impact on the environment. Over the past decade, atmospheric CO_2 concentrations have increased by 18.4% (Figure 2.1),[78] and with the rise of global extreme weather events,[79] it is obvious that new and improved ways to deal with anthropogenic carbon emissions must continue to be studied.

Typical industrial CCS involves the use of liquid amine sorbents to scrub CO_2 out of flue gas streams. While they feature good working capacities, subsequent regeneration (i.e., release of captured CO_2) is energy intensive and offsets overall CCS efficiency.[80] Addressing this challenge has spurred the development of MOF materials (Figure 2.1) that offer both high selectivity and capacity for CO_2 adsorption, as well as lower energy requirements for sorbent regeneration. MOFs have already began

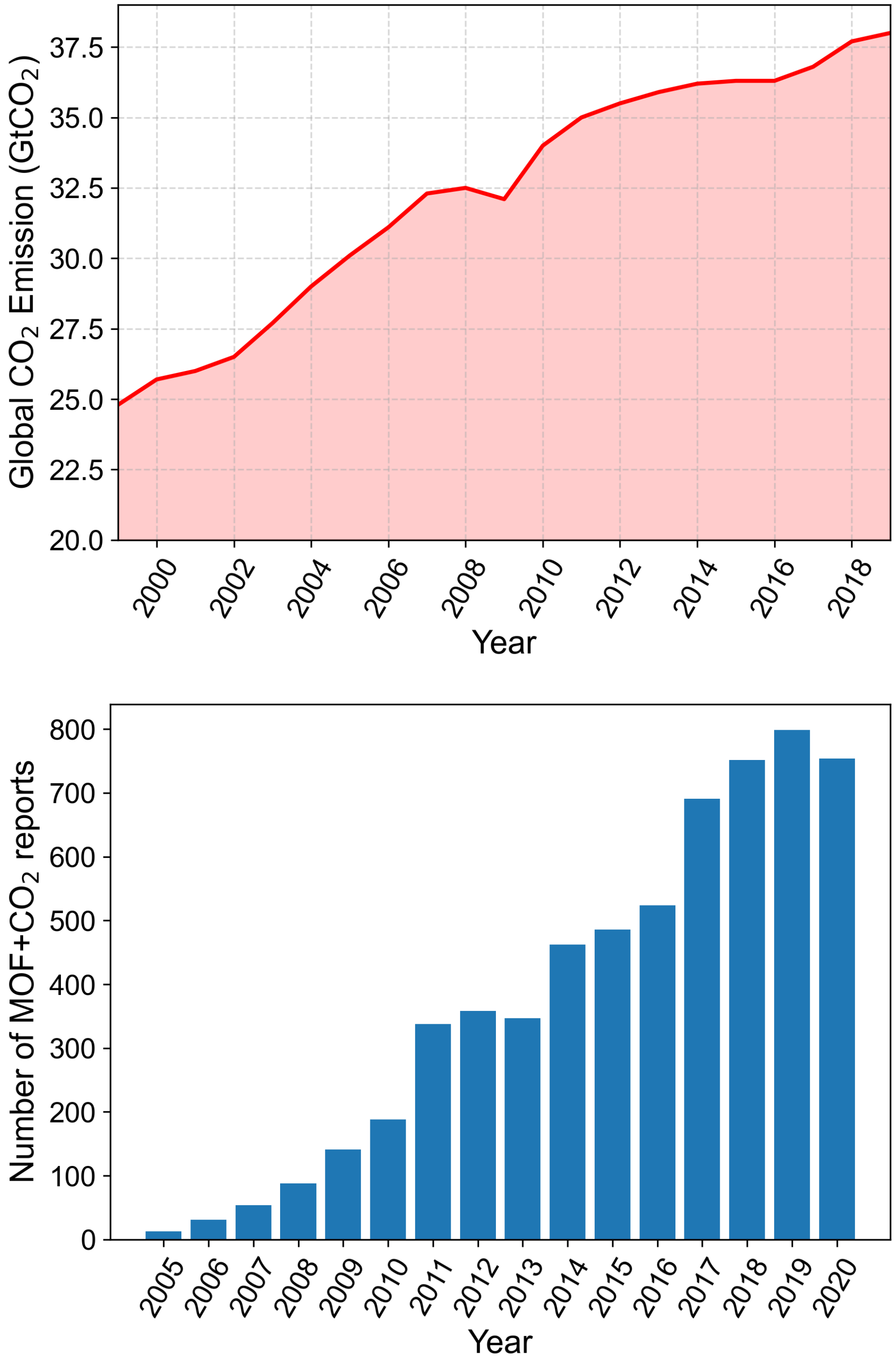

Figure 2.1: Top: Global carbon dioxide emissions in gigatons (GtCO$_2$); Bottom: Number of SciFinder® reports for MOFs + CO$_2$

to play a pivotal role against rising CO_2 emissions. Recently, CALF-20 (Zn_2tz_2ox, where tz = triazolate and ox = oxalate), a MOF with good water stability and CO_2 adsorption properties, has been implemented as an adsorbent for cement flue gas streams.[81]

The work herein seeks to better understand the gas adsorption and separation capabilities of two MOFs, $\mathbf{Zn_3}$ and $\mathbf{Zn_2Cd}$, previously found by the Katz group. The synthesis of these MOFs has been previously discussed in the thesis of Victoria Downing,[82] while the present thesis will focus on their crystallographic structure and gas adsorption behaviours.

2.2 Results and Discussion

$\mathbf{Zn_3}$ and $\mathbf{Zn_2Cd}$ are a pair of isostructural MOFs, meaning that they share the same geometric arrangement of nodes and linkers, and thus have identical framework topologies. These MOFs have the formula $Zn_2M(NH_2BDC)_3DABCO$, where M = Zn or Cd. Figure 2.2a below shows the node geometry, which features a Zn_{tet}–M_{oct}–Zn_{tet} trimetallic unit pillared by DABCO along the *c*-axis. Along the *ab*-plane, there are two sets of three NH_2BDC 'spokes' that are offset from each other by 60°. Each group of three NH_2BDC linkers and half of each node form a 2D-hexagonal sheet (Figure 2.2b). Since each sheet contains half of a node, the M_{oct} center acts as a sort of fuse point between two adjacent sheets. As a result of the offset in the NH_2BDC linkers, the hexagonal sheets are also offset from each other (see Figure 2.2c, when the second sheet is added, it does not perfectly eclipse the sheet below it). This way of stacking hexagonal sheets gives the appearance of triangular channels down the crystallographic *c*-axis, though in reality, the pore structure is likely more toroidal in

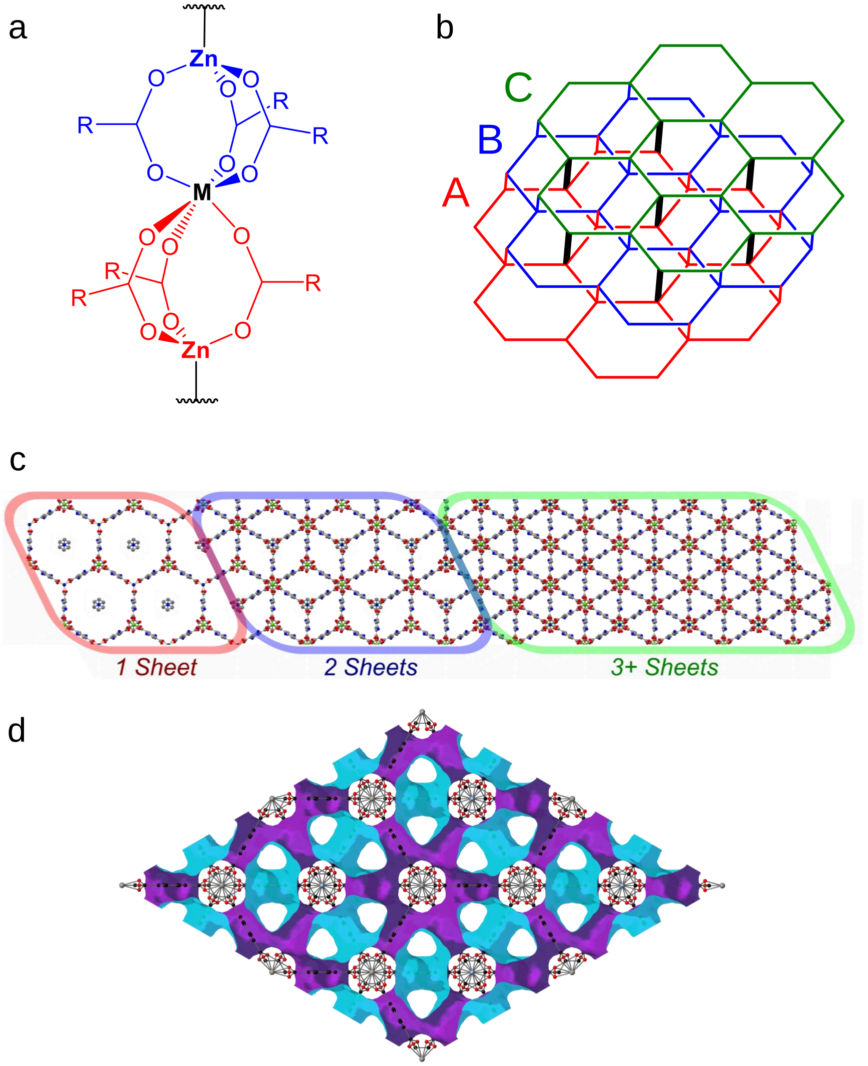

Figure 2.2: a) Depiction of the Zn_2M MOF node geometry, where M = Zn for $\mathbf{Zn_3}$, M = Cd for $\mathbf{Zn_2Cd}$, and R(COO) = NH_2BDC. b,c) Stacking of interconnected hexagonal sheets of Zn_2M. Black lines in (b) represent DABCO pillars that connect between A and C sheets, which can be seen in the single sheet part of (c). d) Connolly surface with a probe size of 1.0 Å, viewed down the crystallographic *c*-axis. Purple represents the inner (inaccessible) surface, while cyan represents the outer (accessible) surface.

shape (Figure 2.2c, single sheet).

These MOFs possess very small pores, in the so-called ‘ultramicroporous’ range

(<7 Å pore width, Figure 2.2d). This is in contrast with many MOFs that feature micropores (7–20 Å), and other porous sorbents that may contain mesopores (20–500 Å) and/or macropores (>500 Å). This ultramicroporous range is ideal for exploring gas separations based on kinetics/molecular sieving, as the pore size starts to approach the molecular size of the gas molecules.

2.2.1 Structural Characterization

To better understand the role that solvent has on the pore size, the structures of $\mathbf{Zn_3}$ and $\mathbf{Zn_2Cd}$ with DMSO and MeOH soaked crystals were collected at both 273 and 100 K. The 273 K data allows for a better understanding of how the structure will behave for gas adsorption applications (often aimed at operational temperatures around ambient temperature and above), while the 100 K data allows for the study of any changes in molecular motion in the MOFs.

Comparing the DMSO soaked structures of $\mathbf{Zn_3}$, which contain a structurally resolved DMSO molecule, at 273 vs. 100 K illustrates a 0.2% decrease in the a/b-axis length with a 0.8% decrease in the c-axis length. When these DMSO-soaked structures are compared with the MeOH-exchanged samples, some key differences are noted. In addition to the larger unit-cell (Table 2.1), the DMSO-containing structure crystalizes in the R $\bar{3}$ spacegroup with six crystallographically resolved DMSO molecules per formula unit. The MeOH-exchanged structure crystallizes in the R $\bar{3}$ m spacegroup with no evidence for localized MeOH units. The spacegroup differences observed are due to the localized DMSO units that can only be observed in three of the six sections of the hexagonal pore, thereby breaking up the R $\bar{3}$ m symmetry. Additionally, the MeOH-exchanged structure shows disorder at 100 K for the whole NH_2BDC linker.

This indicates that in the absence of a tightly filled pore (e.g., as in the DMSO-containing sample), the structure is more flexible. The removal of DMSO also results in a 1% decrease in the a/b-axis length and a 1.8% decrease in the c-axis length at 273 K.

In the case of $\mathbf{Zn_2Cd}$, going from 273 to 100 K in the DMSO-containing structure showed a similar absolute change in the unit cell dimensions as was observed for $\mathbf{Zn_3}$ (Table 2.1). However, there is a much larger decrease in the axis lengths when DMSO is exchanged for MeOH in $\mathbf{Zn_3}$ than in $\mathbf{Zn_2Cd}$. This suggest that the DMSO is more constrained in $\mathbf{Zn_3}$ and once it is exchanged the structure is no longer being held open and it shrinks. This further suggests that when a pore-bound guest is almost too big to fit in the structure, the structure can stretch to some degree to allow for it to incorporate the guest (see below).

Next, assessment of the pore characteristics of the MOFs was performed computationally. The pore aperture as well as the pore width was calculated for both $\mathbf{Zn_3}$ and $\mathbf{Zn_2Cd}$ using the PoreBlazer software package,[83] using a He-sized (2.58 Å) probe to ensure access to the majority of the structure. For each MOF, two crystal structures are available to be examined: the as-synthesized structure that contains DMSO in the pores, and a solvent-exchanged structure containing MeOH. Starting from the as-synthesized structure of $\mathbf{Zn_3}$, removal of the pore-occupying DMSO molecules was done using VESTA software[84] to simulate an 'empty' structure. Recall that in this structure the DMSO is 'puckering' the structure outward, which may result in an over estimate of the calculated values. It was found that 44% of this structure is unoccupied (i.e., empty space between framework atoms) via PLATON SQUEEZE[85] with a pore aperture of 3.47 Å and a pore width of 4.90 Å (Table 2.2, columns 1 and 2). Notably, the DMSO-solvated structure has nearly no crystallographic disorder, which

Table 2.1: Unit cell parameters of Zn_2M in different solvents and collected at different temperatures. Columns/rows with Δ represent the change in unit cell lengths, with relative change indicated in parentheses. Further structural information can be found at CCDC 2076836-2076839, 2153801, 2153802, 2153920-2153923.

		$\mathbf{Zn_3}$		$\mathbf{Zn_2Cd}$		Δ ($\mathbf{Zn_3 \rightarrow Zn_2Cd}$)	
		a/b	c	a/b	c	a/b	c
DMSO	273 K	18.339 602(17)	13.981 500(17)	18.556 000(17)	14.133 901(17)	0.216 398 (1.18)	0.152 401 (1.09)
	100 K	18.304 699(17)	13.866 301(14)	18.526 800(14)	13.961 600(14)	0.222 101 (1.21)	0.095 299 (0.69)
	Δ (273→100)	0.034 903 (-0.19)	0.115 199 (-0.82)	0.0292 (-0.16)	0.172 301 (-1.21)		
MeOH	273 K	18.157 61(2)	13.722 409(19)	18.503 57(2)	13.968 13(2)	0.345 960 (1.91)	0.245 721 (1.79)
	100 K	18.126 96(2)	13.648 43(2)	18.4624(3)	13.8878(3)	0.335 440 (1.85)	0.239 370 (1.75)
	Δ (273→100)	0.030 650 (-0.17)	0.073 979 (-0.54)	0.041 170 (-0.22)	0.080 330 (-0.58)		
Δ (solvent)	273 K	0.181 992 (-0.99)	0.259 091 (-1.85)	0.052 430 (-0.28)	0.165 771 (-1.17)		
	100 K	0.177 739 (-0.97)	0.217 871 (-1.57)	0.064 400 (-0.35)	0.073 800 (-0.53)		

is attributed to the rather large DMSO molecules swelling and rigidifying the framework. When the DMSO is exchanged for MeOH, the connectivity (i.e., topology) of the framework remains the same, but the NH_2BDC units display increased flexibility (i.e., more disorder in the structure). This results in an apparent (see below) decrease in the pore aperture and width (Table 2.2, columns 3 and 4).

Table 2.2: Pore apertures and widths (in Å) of solvated $\mathbf{Zn_3}$ and $\mathbf{Zn_2Cd}$ calculated with PoreBlazer from structures obtained at 273 K.

	DMSO-solvated		MeOH-solvated	
	Pore aperture	Pore width	Pore aperture	Pore width
$\mathbf{Zn_3}$	3.47	4.90	3.29	4.80
$\mathbf{Zn_2Cd}$	4.08	5.03	3.09	5.05

Looking back at the crystal structures, in the MeOH-solvated $\mathbf{Zn_2Cd}$ structure, the Cd-O bonds are *ca.* 17% longer than the equivalent Zn-O bonds (2.2442(15) Å vs. 1.913(3) Å). This leads to a small twist in the NH_2BDC linker that results in a slight increase in the size of the hexagonal sheet. For the MeOH-solvated structure of $\mathbf{Zn_2Cd}$, the pore aperture and width were calculated to be 3.09 Å and 5.05 Å, respectively. In the MeOH-solvated structures of both MOFs, the calculated pore dimensions are affected by the increased flexibility of the frameworks, which show crystallographic disorder in the linkers (unlike the structure occupied by DMSO which is comparatively more rigid and less disordered), and as the calculations are done on a time-averaged structure rather than dynamically, there is likely an underestimation of the true pore sizes. This is particularly true for the pore aperture of MeOH-exchanged $\mathbf{Zn_2Cd}$, which is known to be larger than that of $\mathbf{Zn_3}$ based on gas adsorption data (see below). The DMSO-filled structures likely paint a more accurate picture for $\mathbf{Zn_2Cd}$, while being a slight overestimate in the case of $\mathbf{Zn_3}$. Nonetheless, these MOFs possess apertures approximately the size of small gas molecules such as CH_4, N_2, and CO_2 (refer to Table 1.1). This indicates that these materials may be ideal

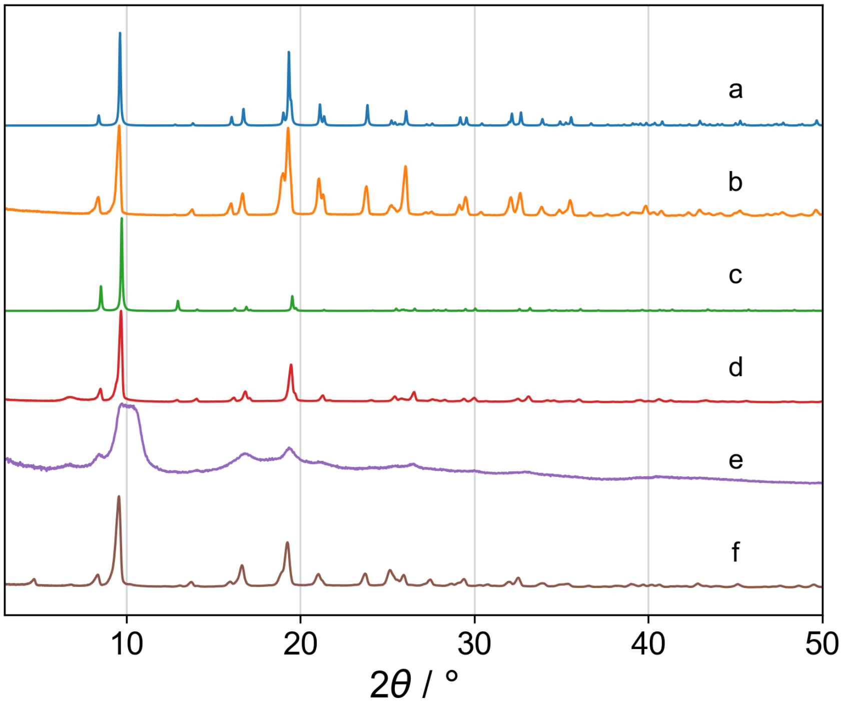

Figure 2.3: PXRD diffractograms of $\mathbf{Zn_3}$. a) simulated DMSO-containing $\mathbf{Zn_3}$. b) as-synthesized $\mathbf{Zn_3}$. c) simulated MeOH-exchanged $\mathbf{Zn_3}$. d) MeOH-exchanged $\mathbf{Zn_3}$. e) activated (solvent removed) $\mathbf{Zn_3}$. f) activated $\mathbf{Zn_3}$ after resolvation in DMF.

for molecular sieving applications.

As another method of exploring the structures of these materials, the powder X-ray diffraction (PXRD) patterns of $\mathbf{Zn_3}$ and $\mathbf{Zn_2Cd}$ were examined. Figures 2.3 and 2.4 show simulated and obtained diffractograms under various conditions. Crystals of both MOFs grow as large hexagons along the *c*-axis that results in preferred orientation; this can be best seen by comparing the $\{1\ 0\ 1\}$ reflection (the first reflection) vs. the $\{2\ \bar{1}\ 0\}$ reflection just shy of 10°. Of particular note is the effect of solvent on the diffraction pattern. The smaller pore sizes of these MOFs lead to more localized solvents that lead to more pronounced differences in the diffraction pattern. The DMSO-containing structures are more localized and the intensity differences between

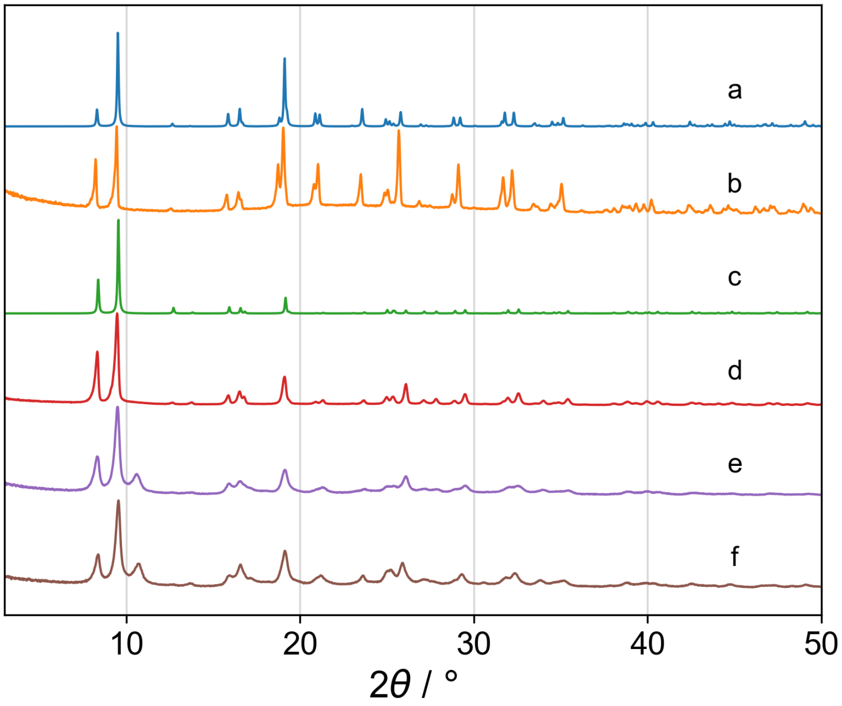

Figure 2.4: PXRD diffractograms of $\mathbf{Zn_2Cd}$. a) simulated DMSO-containing $\mathbf{Zn_2Cd}$. b) as-synthesized $\mathbf{Zn_2Cd}$. c) simulated MeOH-exchanged $\mathbf{Zn_2Cd}$. d) MeOH-exchanged $\mathbf{Zn_2Cd}$. e) activated (solvent removed) $\mathbf{Zn_2Cd}$. f) activated $\mathbf{Zn_2Cd}$ after resolvation in DMF.

the observed and measured diffractograms are more pronounced. For the methanol-exchanged samples, where the solvent in the pore is more dynamic, the observed and calculated diffraction patterns are more similar. Overall, the diffraction patterns of these samples coupled with the single crystal X-ray diffraction indicate that solvent exchange of the MOF does not lead to a change in the topology. Once the solvent was removed from the MOFs (i.e., activation, see Experimental), significant peak broadening was observed. This is indicative of the highly flexible nature of these frameworks, as noted from single crystal data. Resolvation of $\mathbf{Zn_3}$ (i.e., refilling the framework with solvent) could be accomplished by stirring the MOF in DMF over several hours, and the PXRD pattern again looks like the solvent-exchanged form. In the case of $\mathbf{Zn_2Cd}$, while peak broadening did occur, it was not to the same extent as what was observed with **Zn_3**. This is consistent with the comparatively smaller changes to the unit cell of **Zn_2Cd** upon solvent exchange (Table 2.1). As a result, no noticeable change was observed in the diffraction pattern after suspension of the MOF in DMF.

2.2.2 Gas Adsorption

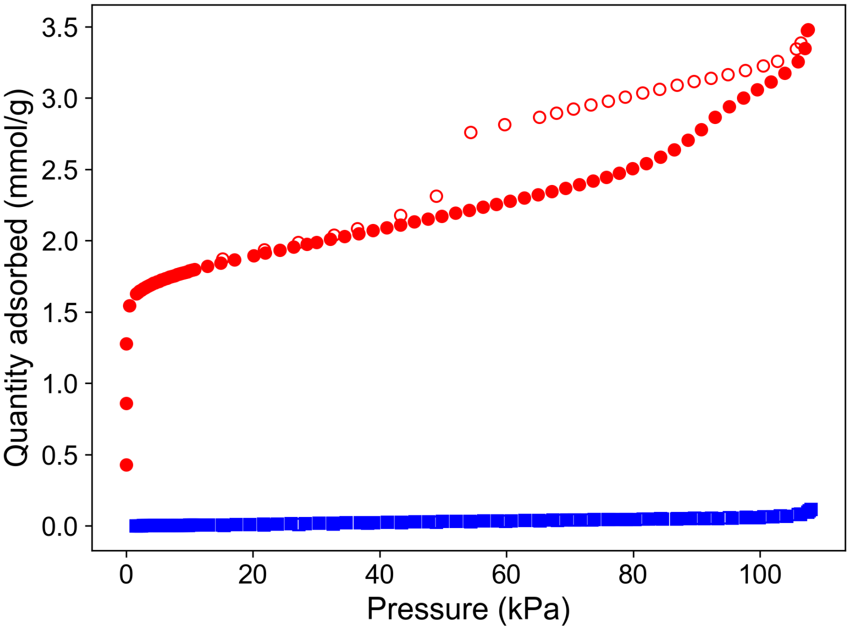

Figure 2.5: N_2 isotherms at 77 K for **Zn_3** (blue squares) and **Zn_2Cd** (red circles). Filled and empty symbols represent the adsorption and desorption arms, respectively.

N_2 gas adsorption isotherms, measured at 77 K, for activated (see Experimental) **Zn_3** and **Zn_2Cd** are shown in Figure 2.5. **Zn_3** showed no N_2 uptake. This is consistent with the small pore aperture calculated from the MeOH-solvated structure. It should be noted that although the pore width of **Zn_3** (4.8 Å) is large enough to theoretically accommodate a N_2 molecule, there is no way for said molecule to enter the framework through the 3.29 Å aperture. Thus it would seem that **Zn_3** should be able to function as a molecular sieve between gases larger and smaller than N_2. Conversely,

Zn_2Cd exhibits a N_2 gas uptake at 77 K of $3.5\,\mathrm{mmol\,g^{-1}}$ and an associated BET surface area of $140\,\mathrm{m^2\,g^{-1}}$. To place this in perspective, UiO-66, a commonly studied MOF,[86] typically has an associated BET surface area from $800–1000\,\mathrm{m^2\,g^{-1}}$ for pristine MOF, up to $1400–1600\,\mathrm{m^2\,g^{-1}}$ when defects are introduced.[87,88] While there may be a large difference between these two MOFs, high surface areas are more important for gas storage applications, and may otherwise be less critical for separations, where efficiency and efficacy are the dominant factors. Indeed, the notable observation here is that the slight expansion of the structure caused by the substitution of Cd into **Zn_3** to form **Zn_2Cd** has opened the framework enough for N_2 to enter. Furthermore, there is noticeable hysteresis in the N_2 isotherm of **Zn_2Cd**, a distinct non-reversible portion of the isotherm where the adsorption and desorption arms do not trace each other. This form of hysteresis in N_2 adsorption isotherms at 77 K is indicative of the presence of mesopores in the framework. It occurs due to capillary condensation (i.e., multilayer formation) in these larger pores. For **Zn_2Cd**, N_2 is not only able to enter the pore through the enlarged aperture, but also now has access to larger cavities within the bulk material.

To explore the molecular sieving capabilities of **Zn_3**, CO_2 gas adsorption isotherms were measured. Recall that CO_2 has a smaller kinetic diameter than N_2 (Table 1.1), and thus may be able to enter the pores of **Zn_3**. This trial-and-error approach of trying to adsorb gases of different sizes is the only realistic method to empirically assess the size of the pore aperture. As can be seen in Figure 2.6, **Zn_3** adsorbs CO_2 gas, placing its pore aperture roughly between 3.3 and 3.6 Å (assuming Breck diameters; see section 1.4.1 for discussion). The sharp uptake of CO_2 at 195 K at low pressures confirms the presence of small micropores. Moreover, this result indicates that **Zn_3** should be capable of sieving CO_2 from its mixtures with N_2, or other larger gas molecules such as CH_4.

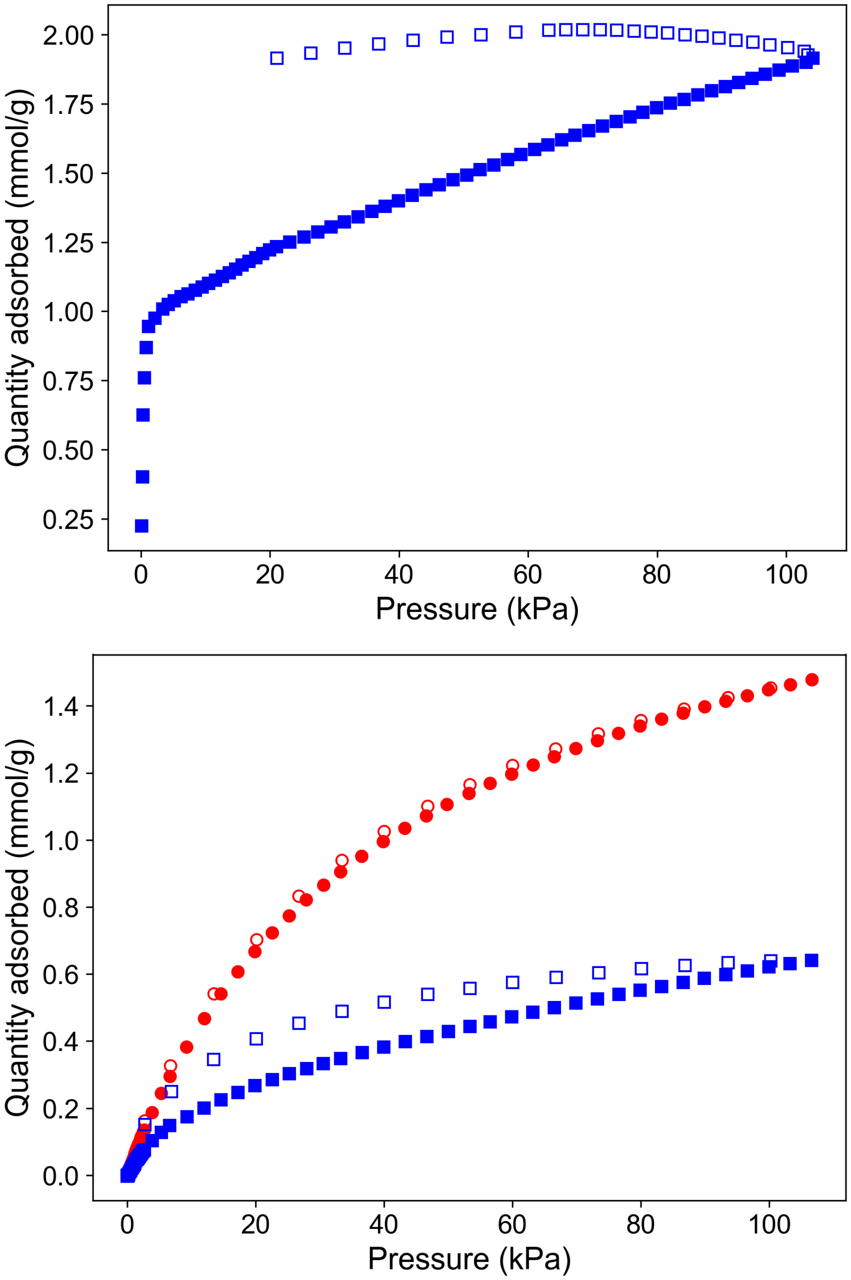

Figure 2.6: Top: CO_2 isotherms at 195 K for **Zn_3**; Bottom: CO_2 isotherms at 273 K for **Zn_3** (blue squares) and **Zn_2Cd** (red circles).

Furthermore, hysteresis is observed for **Zn_3**, both at 195 K and 273 K. Unlike what was observed for N_2 adsorbing onto **Zn_2Cd**, the hysteresis in the CO_2 isotherm of **Zn_3** may be more indicative of a swelling (i.e., rigidification) of the unoccupied, flexible framework during CO_2 adsorption. This is consistent with the lack of disorder observed in the DMSO-solvated (rigid) structure vs. the MeOH-solvated (more flexible) structure. Once occupied, the small pores tightly bind CO_2 and desorption becomes more difficult. In the larger **Zn_2Cd**, the pores can easily accommodate CO_2 and does not show hysteresis (i.e., no rigidification and/or CO_2 confinement effects).

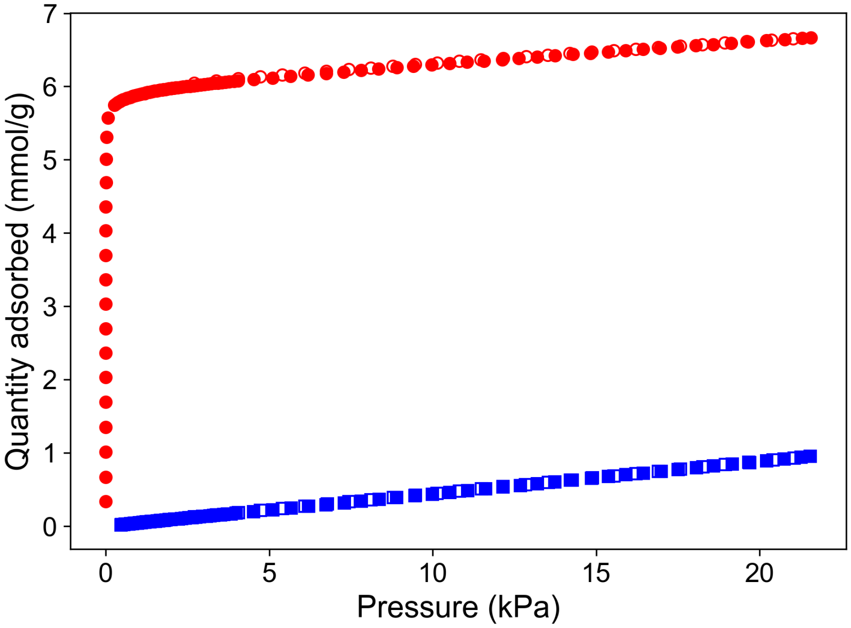

Figure 2.7: Ar isotherms at 77 K for **Zn_3** (blue squares) and **Zn_2Cd** (red circles).

To further narrow down the aperture dimensions of **Zn_3**, a gas must be chosen with a kinetic diameter between that of CO_2 and N_2. Argon ($\sigma_B = 3.4$ Å) fits this description perfectly. Typically, low temperature Ar isotherms are collected at either 77 or 87 K. At 87 K (i.e., the boiling point of Ar), the system is above the triple point of Ar and as a result capillary condensation can occur, allowing for the characterization of mesopores. The diffusion kinetics are also slightly higher than they would be at 77 K.

A drawback, however, is that adsorption at 87 K requires liquid Ar, or specifically designed hardware, making experiments at this temperature cost prohibitive. As an alternative, Ar adsorption can be done at 77 K using liquid N_2. At this temperature, the ability to evaluate mesoporosity is lost as the system is now below the triple point of Ar and capillary condensation will not occur. Nonetheless, as the primary interest is ultramicropore adsorption and framework accessibility, this limitation does not pose a significant problem, and thus the experiments can be conveniently performed at 77 K.

As seen from Figure 2.7, $\mathbf{Zn_2Cd}$ is unsurprisingly porous to Ar. This time, a fully reversible isotherm with no hysteresis is observed, as there is no capillary condensation as there was with N_2 as the adsorbate. As for $\mathbf{Zn_3}$, a total uptake of roughly $1\,\mathrm{mmol\,g^{-1}}$ was measured. While this seems to be an appreciable amount compared to what was measured for N_2, the lack of a sharp, initial uptake would suggest that the small pores of the framework were not accessed. Instead, the Ar isotherm fits the linear Henry model ($q = K_H P$, where K_H is a constant) and a K_H of $0.044\,02\,\mathrm{mmol\,g^{-1}\,kPa^{-1}}$ was obtained. Such a Henry-type adsorption isotherm is consistent with what would be seen with non-porous substrates, or in another sense, the gas is adsorbing onto the outer surface of the material. The Ar adsorption that is seen for $\mathbf{Zn_3}$ could hence be associated with external surface adsorption, which is highly dependent on individual sample particle size or the degree of crystal fracturing during activation.

Another possibility is that due to the very small pore aperture of $\mathbf{Zn_3}$, only limited adsorption is observed due to the effects of activated diffusion.[89] Activated diffusion is the process by which adsorbate molecules must 'hop' (i.e., adsorb, desorb, and readsorb) on their path from the outside of a framework to further inside the framework.

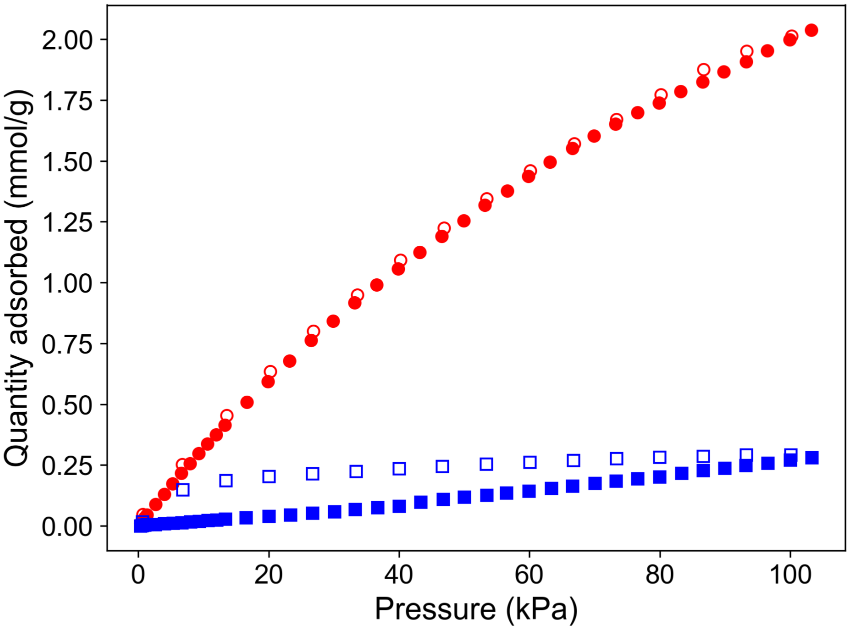

Figure 2.8: Ar isotherms at 195 K for **Zn_3** (blue squares) and **Zn_2Cd** (red circles).

This 'hopping', as the adsorbate molecule enters the framework, has a particular activation energy which, at low temperatures especially, will limit the diffusion of the adsorbate. This has long been observed in the study of microporous carbon-based adsorbents and zeolites,[2,89–92] where for certain materials (e.g., sodium aluminosilicate sieve 4A), N_2 does not appreciably adsorb at 77 K, but does adsorb at higher temperatures (e.g., 195 K).

In order to verify this, Ar isotherms were collected at 195 K (Figure 2.8); at this temperature the process of activated diffusion should no longer hinder the adsorption of Ar. **Zn_2Cd**, which is known to not be limited by diffusion, adsorbed roughly 60% less Ar at 195 K vs. 77 K (2.05 vs. 6.6 mmol/per/g). Likewise, **Zn_3** shows a similar decrease in quantity adsorbed, 0.28 vs. 0.95 $\mathrm{mmol\,g^{-1}}$ at 195 and 77 K, respectively. This would suggest that activated diffusion is likely not limiting the adsorption of Ar in **Zn_3**. With this it can be claimed that the pore aperture of **Zn_3** sits between 3.3 and 3.4 Å (assuming Breck diameters).

Next, finding an upper bound for the pore aperture of **Zn_2Cd** was explored. To this end CH_4 adsorption at 273 K was examined; CH_4 has a Breck kinetic diameter of 3.8 Å, slightly larger than N_2. For **Zn_2Cd**, an adsorption uptake of $0.43\,\mathrm{mmol\,g^{-1}}$ was observed (Figure 2.9). **Zn_3** showed no uptake as expected. Although **Zn_2Cd** is unable to exclude CH_4, this result at least allows for a lower bound to be set for the pore aperture. In fact, it is perhaps expected given the increase in size from **Zn_3** to **Zn_2Cd**. Recall that the Cd-O bond lengths are roughly 17% longer than the equivalent Zn-O bonds. Then, taking the **Zn_3** pore aperture to be 3.4 Å, an increase by 17% would result in a new aperture of 4.0 Å. Even if only an estimate, this value would be consistent with the results so far observed for **Zn_2Cd**. This larger aperture could be particularly useful for the separations of mixtures of hydrocarbons, such as C_2H_4/C_2H_6 (4.16 vs. 4.44 Å kinetic diameters, respectively) or C_3H_6/C_3H_8 (4.68 vs. 4.3 Å, respectively).[93]

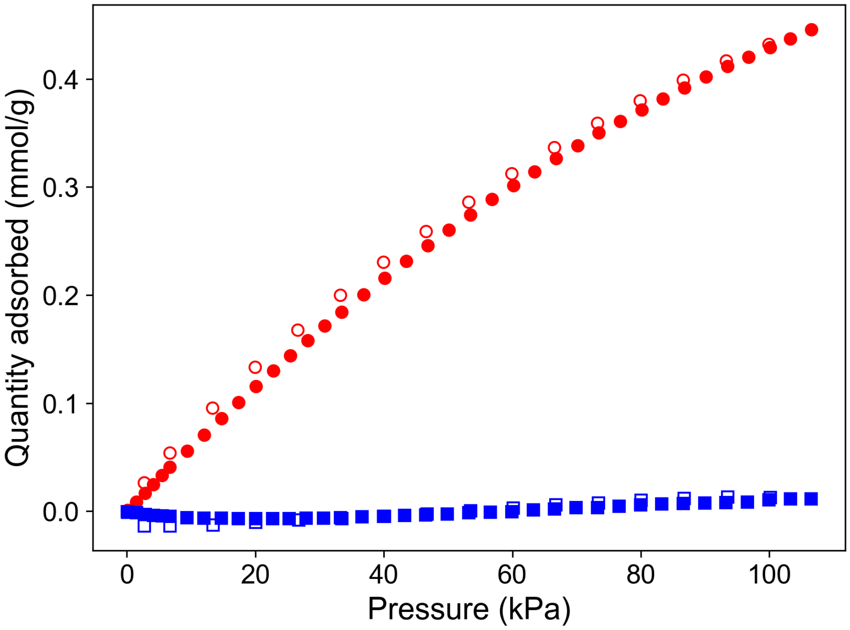

Figure 2.9: CH_4 isotherms at 273 K for **Zn_3** (blue squares) and **Zn_2Cd** (red circles).

2.2.3 Isosteric Heats of Adsorption

To investigate the strong CO_2-framework interaction in **$\mathbf{Zn_3}$**, as evidenced by the adsorption hysteresis, the corresponding isosteric heats of adsorption (Q_{ST}) for CO_2 were calculated. As mentioned previously in Section 1.2.1, this can be done by fitting gas adsorption isotherms to a model. For the MOFs in this work, the dual-site Langmuir model (DSLM) was chosen, given in Equation 2.1 below:

$$q = \frac{q_{m,1}K_1P}{1+K_1P} + \frac{q_{m,2}K_2P}{1+K_2P} \tag{2.1}$$

The DSLM, as the name suggests, is a combination of two distinct Langmuir-type adsorption sites (subscripts 1 and 2 in Equation 2.1), each one equivalent to the single-site model that was discussed Chapter 1. Indeed, one could imagine combining three or more sites to further increase the granularity of the model, though in such situations it is typically more favourable to choose a different model entirely. Regardless, the DSLM allows a ‘hot’ and ‘cold’ site (strong and weak adsorbate binding sites, respectively) to be distinguished in the materials, which is otherwise not possible with only a single-site model.

Shown in Figure 2.10 are the DSLM fits to the CO_2 gas adsorption isotherms taken at 285, 290, and 295 K, with the associated fit values presented in Table 2.3. These obtained fits were used to calculate Q_{ST} for the studied MOFs, as outlined by Long and co-workers.[94] The Q_{ST} for CO_2 in **$\mathbf{Zn_3}$** is initially relatively high (ca. $35\,\mathrm{kJ\,mol^{-1}}$, with a Q_{ST} at zero loading of $40.2\,\mathrm{kJ\,mol^{-1}}$, Figure 2.11). This data is consistent with the hysteresis observed in the CO_2 gas adsorption isotherm and further supports the idea of a strongly binding site, leading to confinement effects in the small pores. Afterwards, the CO_2 adsorption enthalpy decreases as more gas is adsorbed and the

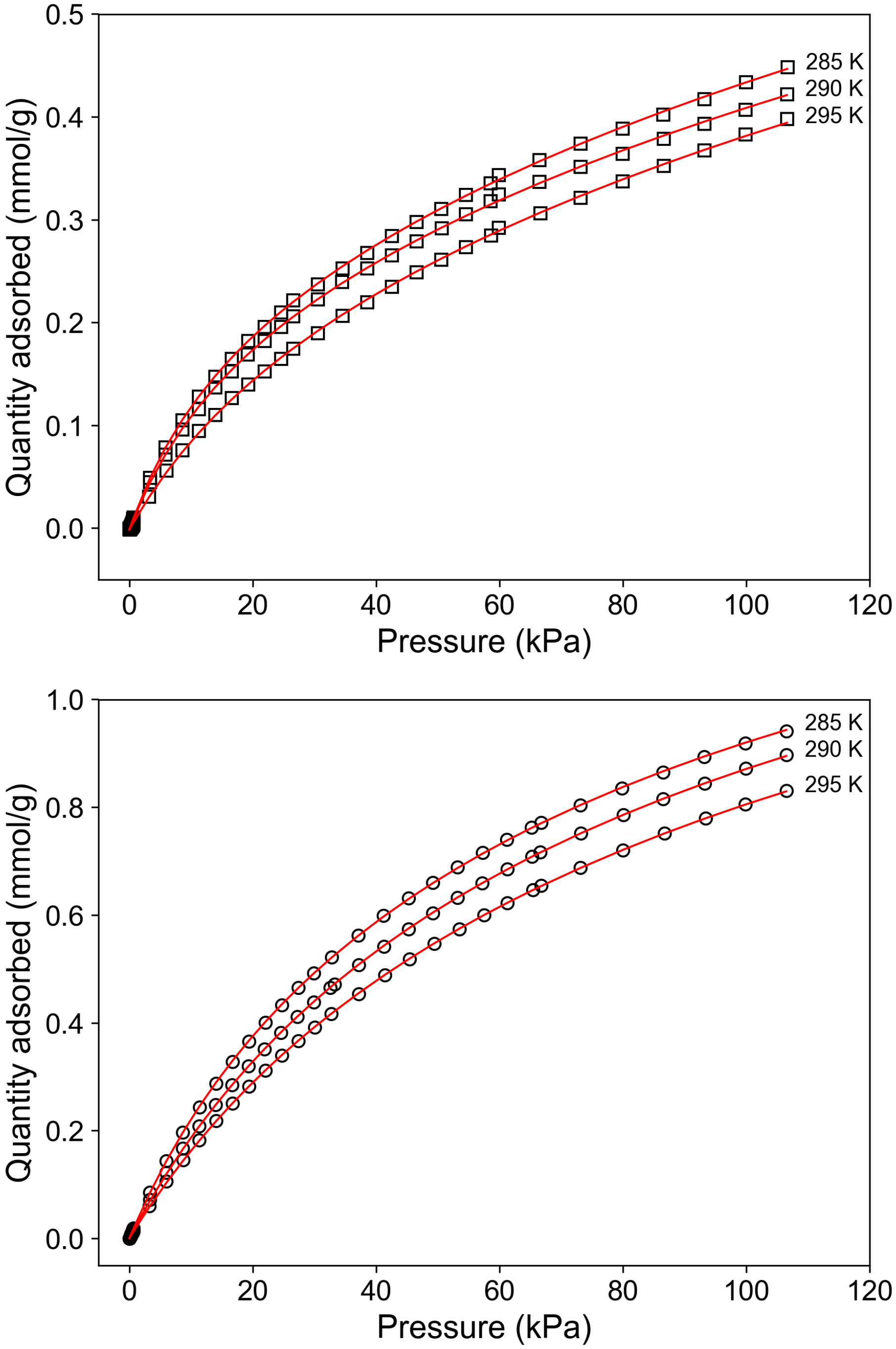

Figure 2.10: DSLM fits (red lines) to the CO_2 adsorption isotherms of $\mathbf{Zn_3}$ (top, squares) and $\mathbf{Zn_2Cd}$ (bottom, circles) at 285, 290, and 295 K.

surface is occupied, down to a minimum of roughly 15 kJ mol^{-1}. This value is consistent with the heat of vaporization for CO_2 (18 kJ mol^{-1}) and indicates the point when the majority of the surface sites of **Zn_3** are occupied.

Table 2.3: Values of the obtained DSLM fits.

	Site 1			
	q_m / mmol g^{-1}	K_{285K} / kPa^{-1}	K_{290K} / kPa^{-1}	K_{295K} / kPa^{-1}
Zn_3	0.222	0.0648	0.0585	0.0364
Zn_2Cd	0.604	0.0310	0.0230	0.0198

	Site 2			
	q_m / mmol g^{-1}	K_{285K} / kPa^{-1}	K_{290K} / kPa^{-1}	K_{295K} / kPa^{-1}
Zn_3	0.857	0.00397	0.00348	0.00323
Zn_2Cd	1.04	0.00796	0.00757	0.00629

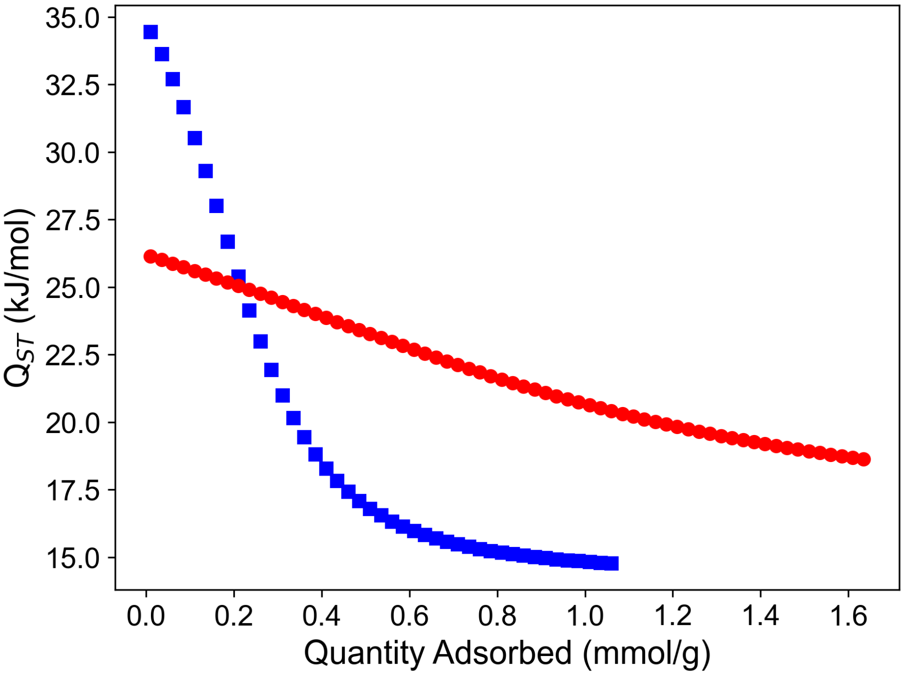

Figure 2.11: Isosteric heats of adsorption for CO_2 in **Zn_3** (blue squares) and **Zn_2Cd** (red circles), calculated at 290 K.

Opening up the structure slightly to **Zn_2Cd**, the Q_{ST} values no longer indicate a significantly strong binding site, and instead there is a more gradual decrease as the framework is filled with CO_2. Interestingly, while both MOFs possess amine-functionalized linkers, which have been shown to have favourable interactions that benefit CO_2 adsorption,[95–97] only **Zn_3** exhibits a particularly 'hot' site, evidenced by its increased Q_{ST} value. This result instead highlights the role that small pores/apertures play in CO_2 affinity through adsorbent confinement,[98] and may suggest that the amine groups of **Zn_3** and **Zn_2Cd** are not positioned to optimally interact with CO_2. This further demonstrates the importance of sub-Å level control over the framework structure, which is needed for developing molecular sieving MOFs.

2.2.4 Gas Separation

After examining the gas adsorption behaviours and associated adsorption enthalpies for these two MOFs, it would seem that **Zn_3** is promising for CO_2-selective gas separations. In order to evaluate and compare these MOFs for potential applications, IAST was used to calculate theoretical adsorptive selectivies. As mentioned in section 1.3.3, IAST allows for the calculation of theoretical adsorption isotherms for a gas mixture of a given composition. These theoretical isotherms may then be used to calculate a selectivity, $S_{CO_2/b}$, for CO_2 over gas b at a particular pressure.

Beginning with CO_2/N_2 selectivity, a gas composition of 15:85 CO_2:N_2 was chosen, which mimics the concentrations of post-combustion flue gas. Perhaps unsurprisingly, **Zn_3**, which is inaccessible to N_2, has a very large calculated selectivity ($S_{CO_2/N_2} = 4800$ at 100 kPa and 295 K, Figure 2.12). Furthermore, the selectivity increases exponentially as pressure increases. This highlights a drawback when using IAST to study ultramicroporous MOFs, particularly those in which molecular sieving occurs. The

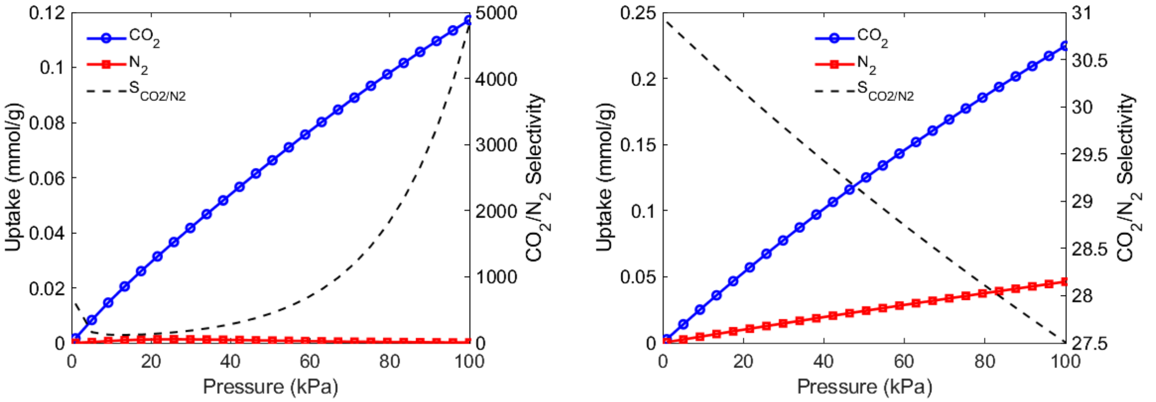

Figure 2.12: Calculated IAST adsorption isotherms and corresponding selectivities of a 15:85 CO_2/N_2 binary mixture for **Zn$_3$** (right) and **Zn$_2$Cd** (left).

theory depends on all components of a gas mixture being able to compete for the same adsorptive sites within the MOF, so as to properly calculate the adsorptive selectivity of one gas over another. For the case of **Zn$_3$** and other molecular sieves, the assumptions of IAST are not met, and the selectivity values become dominated by the uncertainties of the instrument collecting the data. Nonetheless, adsorptive selectivies from IAST calculations are still frequently performed on such materials as a qualitative measure and tool for comparison.

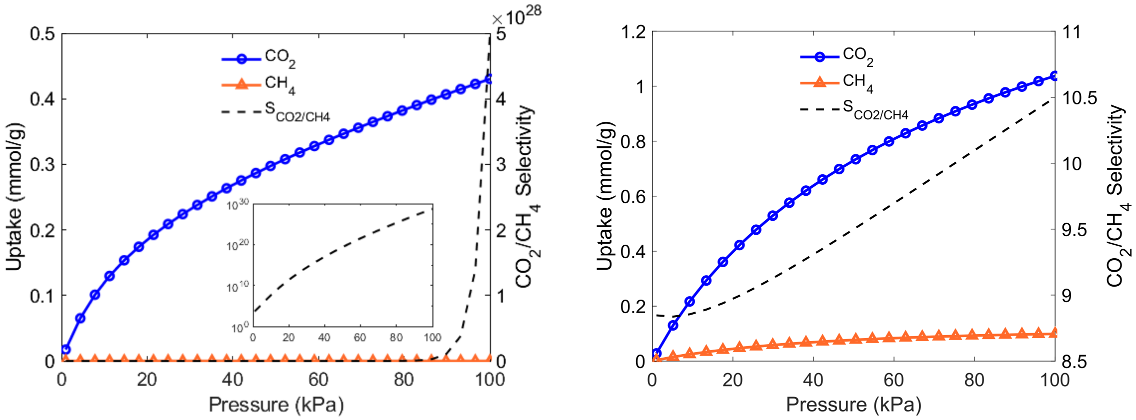

Figure 2.13: Calculated IAST adsorption isotherms and corresponding selectivities of a 15:85 CO_2/N_2 binary mixture for **Zn$_3$** (right) and **Zn$_2$Cd** (left). The inset for **Zn$_3$** shows the selectivity on a log plot.

For **Zn$_2$Cd**, a S_{CO_2/N_2} of 27.5 at 100 kPa and 295 K is obtained. As it does not act as a molecular sieve for this particular gas pair, it can be assumed that the selectivity of **Zn_2Cd** is relatively accurate. Indeed, the difference in selectivity caused by the very slight expansion of the structure going from **Zn_3** to **Zn_2Cd** is striking. The same trend is seen for the CO_2/CH_4 gas pair; **Zn_2Cd** has a marginal S_{CO_2/CH_4} of 10.5 at 100 kPa and 273 K. Interestingly, the selectivity towards CO_2 seems to very slightly increase with pressure. While this might be an indication that **Zn_2Cd** could have a greater S_{CO_2/CH_4} at higher pressures, this needs to be confirmed with complimentary high-pressure adsorption isotherms or real-world selectivity studies that are beyond the current capabilities of our instrumentation. On the other hand, **Zn_3** is calculated to have an unbelievable S_{CO_2/CH_4} value of ca. 10^{28} at 100 kPa and 273 K. Although qualitative, these results highlight the tuneability afforded with these Zn_2M nodes.

2.3 Conclusions and Future Work

In summary, two isostructural ultramicroporous MOFs were extensively characterized both crystallographically and by studying their gas adsorption properties. In this chapter, a detailed examination of not only the accessibility of **Zn_3** and **Zn_2Cd** to different gases, but also of how the structures of these MOFs expand/contract in different solvents and at different temperatures was performed. Such small changes in the frameworks, which may be insignificant in more conventional, larger-pore MOFs, proved to be a key part of the difference in molecular sieving capabilities between **Zn_3** and **Zn_2Cd**. By assessing adsorption of gases of increasing kinetic diameters (CO_2 < Ar < N_2 < CH_4) and at different temperatures, it could be determined that **Zn_3** has a pore aperture between 3.3 and 3.4 Å (assuming Breck diameters), allowing for theoretically infinite separation selectivity of CO_2 from larger gases. On the other hand **Zn_2Cd** was found to adsorb CH_4, placing its aperture above 3.8 Å.

The incorporation of Cd into the framework not only opened up the pores, but also resulted in less structural change upon solvent exchange or removal, which explains its different gas adsorption behaviour.

2.3.1 MOF-based Hybrid Membranes for Gas Separation

The work presented in this chapter lays the groundwork for the next rational step with these materials; mixed-gas separation experiments. As much as IAST and other computational methods allow for the prediction of how these MOFs might perform in a particular separation application, only real-world experiments will give a concrete idea of how efficient these materials are. The standard method to assess materials in this way is called a breakthrough experiment. In a typical breakthrough, a mixture of gases at predetermined concentrations is flowed through a packed column of adsorbent (e.g., MOF) while the composition of the column outlet is monitored (e.g., by mass detection).[99] Then, breakthrough times of the each component gas can be determined when a change in the outlet concentration occurs, along with the corresponding separation selectivity. As the Katz lab will have a new breakthrough instrument at our disposal, it will be the perfect opportunity to test $\mathbf{Zn_3}$ and $\mathbf{Zn_2Cd}$.

Adequate preparation of the adsorbent column is critical for obtaining reproducible and sensible breakthrough data. In the case of $\mathbf{Zn_3}$, this is anticipated to be particularly challenging given the ultramicropores and molecular sieving effects. Typically, the microporous adsorbents used in breakthroughs separate gases based on their adsorptive selectivity, rather than size exclusion. As such, all gases in the mixture can freely passes through the adsorbent (Figure 2.14, top), with one component adsorbing more than the others. Difficulty arises when some components of the gas mixture are prevented from entering the adsorbent. Significant back-pressure would be expected due to the restricted flow, and if slight defects occurred during packing, then gases could diffuse through interparticle spaces (Figure 2.14, bottom), lowering overall separation efficiency.

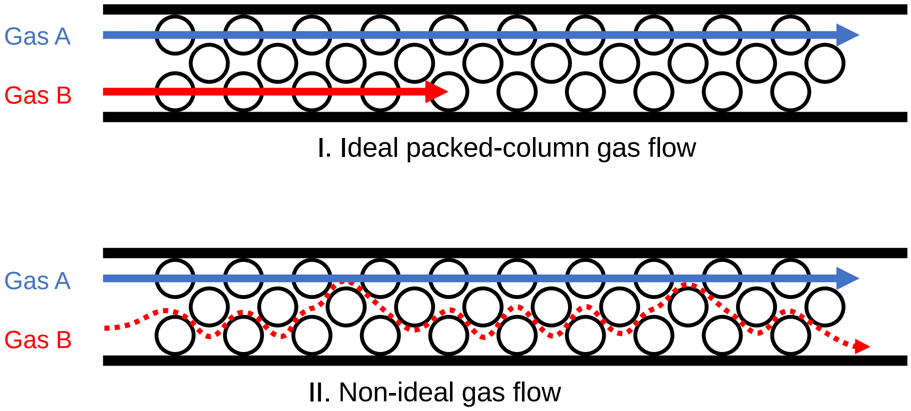

Figure 2.14: Gas flow through packed adsorbent columns. The ideal case (top) illustrates both gases flowing through the adsorbent with gas B being preferentially adsorbed, allowing the gases to be separated. With ultramicroporous adsorbents, particularly for molecular sieving, there is a risk of gases flowing through interparticle spaces (bottom) and decreasing the effective separation.

Furthermore, the adsorbents used in such so-called ‘fixed-bed’ systems often feature higher adsorbent capacities as they must capture and store the gas that is being separated. As has been demonstrated with single-component adsorption experiments, $\mathbf{Zn_3}$ and $\mathbf{Zn_2Cd}$ do not possess particularly high capacities. However this does not detract from their promising separation capabilities, particularly $\mathbf{Zn_3}$, as it is expected that incorporation of these MOFs into a mixed-matrix membrane (MMM) system would better highlight their capabilities to separate gases, without necessarily needing to worry about storing the separated gas. MMMs are a type of hybrid materials which combine porous sorbents such as MOFs with durable and processable polymers.[100] These sorts of membranes have been used in gas separations,[101,102] optics,[21] and sensing[103] applications with the polymer component acting as a robust substrate without compromising the properties of the incorporated MOFs.

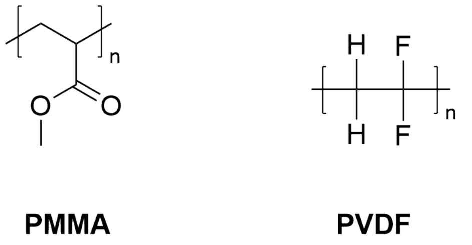

Figure 2.15: Structures of polymethyl methacrylate (PMMA) and polyvinylidene difluoride (PVDF) polymers.

Our group has already begun preliminary work on the fabrication of MMMs containing **Zn_3** and **Zn_2Cd**. As a starting-off point, creating MMMs using polymethyl methacrylate (PMMA) and polyvinylidene difluoride (PVDF) polymers (Figure 2.15) will be investigated. These two polymers give an opportunity to try two different approaches to MOF incorporation: PMMA membranes can be covalently linked to the MOF through post-synthetic functionalization of the MOF linker, while in PVDF membranes, MOF particles can be directly embedded without any modification. Scheme 2.1 illustrates how a MOF containing amino-functionalized linkers (as is the case for **Zn_3** and **Zn_2Cd**) can be further modified for incorporation into a PMMA membrane. This process could produce membranes with minimal macro-voids or gaps between the MOF and polymer. It is easy to imagine that gas will want to travel along the path of least resistance, so minimizing these routes which flow around the MOF rather than through the MOF will increase the overall separation efficacy.

As an alternative to methacrylate-based membranes, PVDF as a polymer for MMMs will be explored as it does not require any additional synthetic modifications to the MOFs in order to form membranes. The procedure to fabricate MOF-incorporated PVDF (MOF@PVDF) membranes is rather simple. As shown in Figure 2.16, MOF

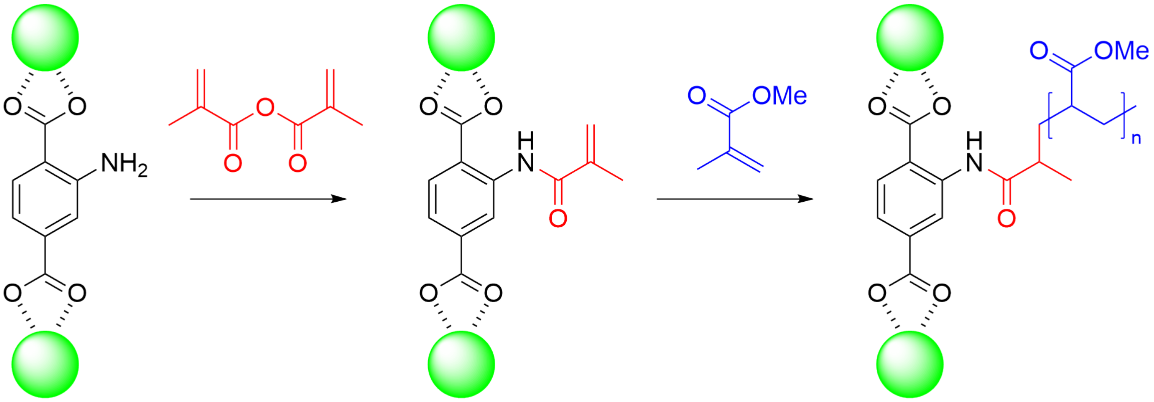

Scheme 2.1: Functionalization of NH_2BDC linkers within MOFs for the preparation of PMMA-based MMMs. Green spheres represent MOF nodes, as the functionalization and polymerization occurs after the MOF is synthesized.

can be suspended in a PVDF solution (e.g., DMF as solvent), poured/cast onto a substrate or mould, and once evaporation of the solvent is complete, a membrane is obtained. The simplicity of this method would allow for high-throughput testing of many membrane formulations, such as the amount of MOF used, the amount of PVDF, as well as co-polymers/fillers that may be incorporated.

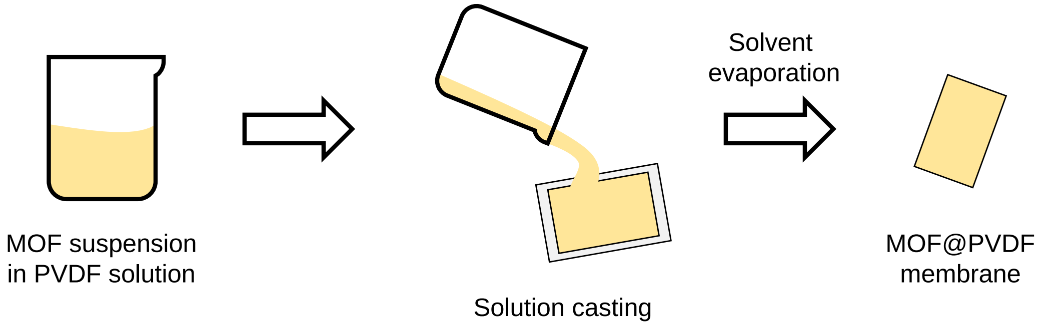

Figure 2.16: Fabrication process for MOF-incorporated PVDF membranes.

2.3.2 Expanding the Zn_3 MOF Family

Since the discovery of $\mathbf{Zn_3}$ and $\mathbf{Zn_2Cd}$, the group has been curious about how analogous structures with different metals and/or linkers might be synthesized. In terms of different metals, it would be logical to substitute the octahedral Zn with other metals that prefer that geometry, such as Mn, Fe, Co, or Ni, as has been done with Cd. From a gas adsorption/separation perspective, while these other metals may not open up the structure as much as Cd (since most 1st-row transition metals are roughly similar in size and none as large as Cd), they may impart greater structural rigidity and thus less shrinking when guest molecules are evacuated from the framework. This could allow even more fine-tuning of the aperture in such a way, for example, that the framework would still be inaccessible to N_2 (pore aperture < 3.64 Å) but possesses an aperture larger than $\mathbf{Zn_3}$ (e.g., 3.5 Å), which would improve CO_2 diffusion kinetics and overall separation efficiency. Beyond gas separation, substituting the metals in the node could lead to systems with interesting catalytic or magnetic properties.

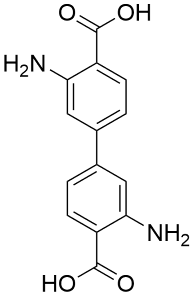

Changing the linkers of $\mathbf{Zn_3}$ and $\mathbf{Zn_2Cd}$ to dicarboxylates other than NH_2BDC would permit a different approach to tuning the pores of the frameworks. Substituting the amino moiety (or removing it altogether) could be used as a way to modify the properties of the pore surface, without changing the overall structure (i.e., pore aperture) too much. On the other hand, a longer linker such as 3,3'-diaminobiphenyl-4,4'-dicarboxylic acid (H_2-$(NH_2)_2$BPDC, shown on the left) would greatly open up the pores. While the resulting MOF would obviously have pore apertures that are too large for molecular sieving, it may nonetheless show interesting gas adsorption properties (e.g., flexibility in the structure could produce gating behaviour).

During the ongoing work towards synthesizing these **Zn_3** analogues, some new structures have been obtained. The first of these structures is **Zn_3(BDC)**, with the formula $Zn_3(BDC)_3(DMSO)_2$. **Zn_3(BDC)** was obtained under identical synthetic conditions to **Zn_3**, with NH_2BDC replaced with an equivalent amount of BDC. This structure possesses a node similar to that of **Zn_3**, with the familiar Zn_{tet}–Zn_{oct}–Zn_{tet} motif, surrounded by two sets of three BDC linkers. Unlike in **Zn_3**, DABCO did not incorporate as a pillar in **Zn_3(BDC)**, despite its presence during the synthesis. Instead, DMSO molecules are seen coordinating in a κO fashion to the tetrahedral Zn atoms, capping the nodes (Figure 2.17b). Another structural difference can be seen in the how two of the BDC linkers coordinate to the metal node. In **Zn_3**, the carboxylates of the linkers bridge two Zn atoms, each one coordinated by a different O atom. In **Zn_3(BDC)**, two of the BDC linkers have carboxylates which bridge two Zn atoms through a μ_2-O. This causes a considerable twist in these linkers, which can be seen in Figure 2.17d (the phenylene groups in the plane of the page). Overall, **Zn_3(BDC)** crystallizes in the $P\ 2_1/n$ space group, forming large 2D sheets rather than a 3D structure.

Taking both approaches of changing the metal node as well as the linker, a second structure was obtained. Namely, **Zn_2Mn(BDC)**, with the formula $Zn_2Mn(BDC)_3(DMSO)_4$. This framework was obtained by following the preparation for **Zn_2Cd**, with $Cd(NO_3)_2 \cdot 4\,H_2O$ replaced with $Mn(OAc)_2 \cdot 4\,H_2O$. Again, the same trimetallic node as the other structures is observed, with Mn occupying the octahedral site (Figure 2.18b). It was found that Mn occupies this site 75% of the time throughout the structure, with the remaining 25% the site is occupied by Zn. In **Zn_2Mn(BDC)**, the Zn atoms are in a trigonal bipyramidal geometry. Each Zn is bridged to Mn via the carboxylate groups of three BDC linkers, and two κO-DMSO molecules cap each Zn to complete the coordination sphere (Figure 2.18a,b). Once

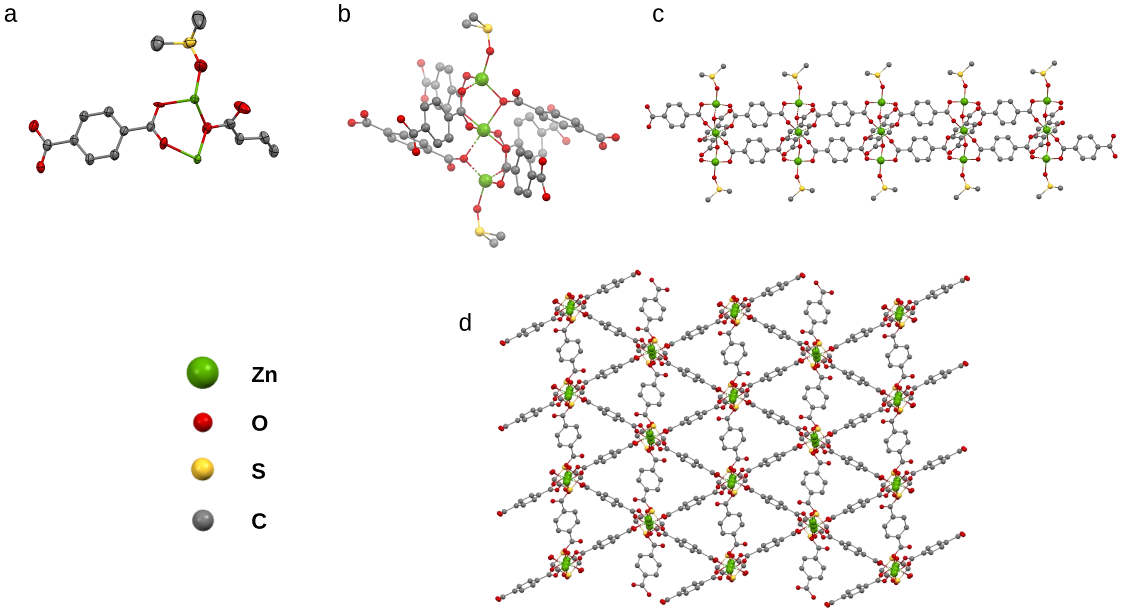

Figure 2.17: Structural diagrams of $Zn_3(BDC)_3(DMSO)_2$. a) Asymmetric unit with thermal elipsoids shown at 50% probability; b) Node geometry; c) View down the crystallographic *b*-axis; d) View along $(\bar{1}\ 0\ 1)$. Hydrogen atoms and pore-occupying DMSO molecules have been omitted for clarity. Structural data is given in Appendix A.

again, DABCO was not seen to be incorporated into the framework. $\mathbf{Zn_2Mn(BDC)}$ also crystallizes in the P 2_1/n space group, and forms a 2D sheet structure as shown in Figure 2.18d.

From these two structures, it is evident that the trimetallic node of $\mathbf{Zn_3}$ can be formed with different metals and a different linker. What remains is to tune the synthetic conditions such that the topology obtained matches that of $\mathbf{Zn_3}$. This may be as simple as increasing the concentration of DABCO in the synthesis to promote its incorporation into the framework. One factor that was found to be important in the synthesis of $\mathbf{Zn_3}$ is the amount of DMF used. When less is used (e.g., half the normal amount), $\mathbf{Zn_3}$ does not form. Moreover, nothing formed when DMF was substituted for STEPOSOL® MET-10U (*N*,*N*-dimethyl-9-decenamide), a greener alternative to

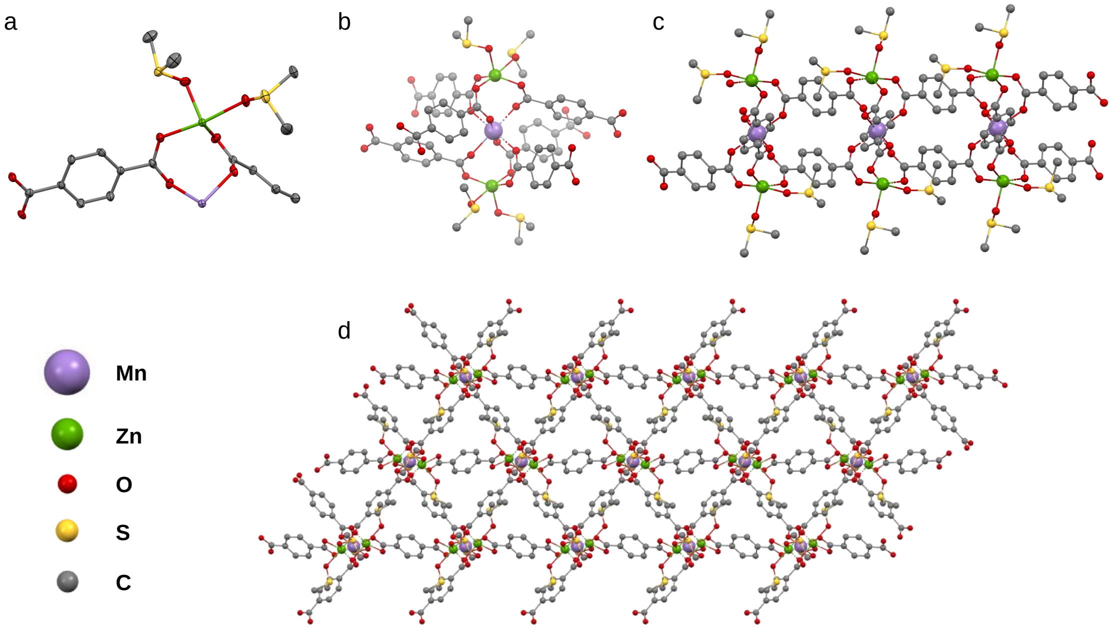

Figure 2.18: Structural diagrams of $Zn_2Mn(BDC)_3 \cdot (DMSO)_4$. a) Asymmetric unit with thermal elipsoids shown at 50% probability; b) Node geometry; c) View down the crystallographic *b*-axis; d) View along $(\bar{1}\ 0\ 1)$. Hydrogen atoms have been omitted for clarity. Structural data is given in Appendix A.

DMF that has recently been applied to MOF synthesis.[104,105] This points to DMF, and more broadly the acid-base chemistry it facilitates, being crucial in the formation of $\mathbf{Zn_3}$ and $\mathbf{Zn_2Cd}$. Playing around systematically with the pH of the reaction might be the key to accessing these new structures.

2.4 Experimental

2.4.1 Materials and Methods

Unless otherwise noted, reagents used herein were purchased from commercial sources and used without further purification.

^{1}H nuclear magnetic resonance (NMR) data were collected on either a Bruker AVANCE 500 MHz spectrometer using an inverse probe or a Bruker AVANCE III 300 MHz spectrometer, as noted in the text.

Powder X-ray diffraction (PXRD) patterns were collected on a Rigaku MiniFlex with sealed-tube X-ray source (CuKα radiation, $\lambda = 1.54$ Å) operating at 40 kV/15 mA and a D/teX Ultra detector.

Gas adsorption isotherms were measured using a Micromeritics 3Flex Surface Characterization instrument, with accompanying MicroActive software suites. Samples measured in the range of 273–295 K were kept at a stable temperature using a VWR circulating water bath connected to an AD07R-40 temperature controller. Samples measured at 195 K were cooled with a dry ice/acetone bath. Otherwise, samples were cooled to 77 K with liquid nitrogen. Sample surface areas were calculated based on Brunauer-Emmett-Teller (BET) theory and associated 4-point criteria, or by Langmuir theory with associated Dual-Site Langmuir fits of CO_2 adsorption isotherms.

2.4.2 MOF Synthesis

UiO-66 was synthesized according to previous literature.[88]

Zn_3 and was synthesized according to a previously reported procedure with slight modification.[82] To a 25 mL glass bottle, 2-aminoterephthalic acid (268 mg, 1.58 mmol), DABCO (95 mg, 0.847 mmol), and $Zn(NO_3)_2 \cdot 6\,H_2O$ (500 mg, 1.68 mmol) were added and dissolved in DMSO (18 mL). To this solution, DMF (1.2 mL) and *di*H_2O (2.7 mL) were added. The bottle was capped and placed in a 110 °C oven for 72 h, after which formation of large yellow, hexagonal crystals was observed. The bottle was removed from the oven and upon cooling, the supernatant was exchanged with fresh DMSO

(20 mL), then exchanged with MeOH (4×20 mL) and left soaking overnight (at least 18 h) to fully remove DMSO from the pores.

Zn_2Cd was synthesized in the same manner as **Zn_3**, using $Zn(NO_3)_2 \cdot 6\,H_2O$ (333 mg, 1.12 mmol) and $Cd(NO_3)_2 \cdot 4\,H_2O$ (173 mg, 0.561 mmol), and was kept in the oven for 48 h, affording large yellow, hexagonal crystals.

Zn_3(BDC) was synthesized as follows: To a 4 dram vial, terephthalic acid (63 mg, 0.38 mmol), DABCO (24 mg, 0.21 mmol), and $Zn(NO_3)_2 \cdot 6\,H_2O$ (125 mg, 0.42 mmol) were added. The solids were dissolved in DMSO (4.5 mL) with sonication, then DMF (0.3 mL) and *di*H_2O (0.7 mL) were added. The vial was capped and placed in a 110 °C oven for 72 h, after which time large, colourless prisms had formed. Once cooled, the supernatant was decanted and exchanged with fresh DMSO (2×8 mL).

Zn_2Mn(BDC) was synthesized in the same manner as **Zn_3(BDC)**, using $Zn(NO_3)_2 \cdot 6\,H_2O$ (83 mg, 0.28 mmol) and $Mn(OAc)_2 \cdot 4\,H_2O$ (34 mg, 0.14 mmol), to afford small colourless crystals.

2.4.3 Gas Adsorption

Prior to gas adsorption measurements, all MOF samples were thermally degassed (activated) using a Micromeritics Smart VacPrep sample preparation instrument. Samples were heated (Zn_2M at 50 °C, UiO-66 at 150 °C) while a vacuum level below 1.00 mmHg was reached at a rate of 5.00 $\mathrm{mmHg\,s^{-1}}$. Then, samples were held under unrestricted vacuum for 1080 min (Zn_2M) or 800 min (UiO-66).

Chapter 3

Linker Design towards Novel Porphyrinic MOFs

3.1 Introduction

As stated in the introduction, porphyrins and porphyrinoids (e.g., chlorins, corrins) are well known biological compounds responsible for energy generation in plants and mammals alike. The core of porphyrin (sometimes referred to as the compound porphine) is shown in Figure 3.1a. In the synthesis of porphyrins, there are two primary areas of functionalization: the *meso*-positions (carbons 5, 10, 15, and 20) and the β-positions (carbons 2, 3, 7, 8, 12, 13, 17, and 18). These positions may contain a large variety of substituents, though as more and more unique groups are added, the synthetic complexity increases rapidly and yields of a particular product can drop due to the formation of isomers and side-products. Chemists have long used the *meso*-positions to tune the steric and electronic properties around the central core. This has allowed researchers to tune the gas binding chemistry in solution-based studies of

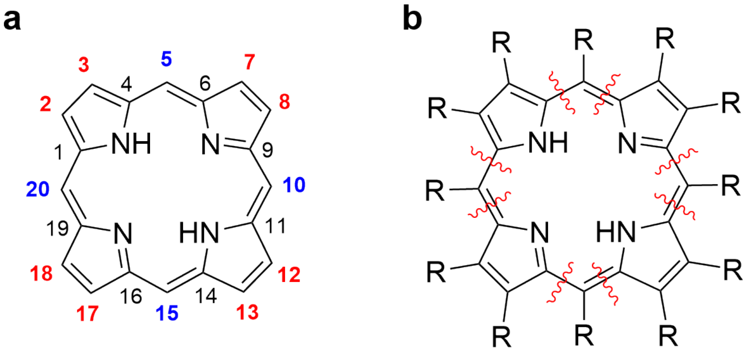

Figure 3.1: a) Structure of the porphyrin core and associated numbering of the peripheral carbons. b) Targeted bonds for the formation of porphryins.

hemoglobin mimics.[106,107] Similarly, MOF chemists have used these same positions to introduce linking moieties for the formation of porphyrinic-MOFs (Por-MOFs). Por-MOFs, with their ability to have metals coordinated to the porphyrin linker itself, are ideal candidates for catalytic applications. With high densities of well-defined active sites, and a rigid framework that prevents porphyrin aggregation, Por-MOFs possess the best features of both homogeneous and heterogeneous catalysts.[63,108]

While adding linking moieties at the *meso*-positions is the logical approach to work on Por-MOFs (due to the synthetic simplicity), there exists a dichotomy between the solution-based porphyrin work and the MOF-based work. It is clear that MOFs can mimic biological applications of porphyrins, but with current Por-MOFs the sterics of the active site of the porphyrin cannot be synthetically tuned, and changes to the electronics of the system are limited as they may begin to interfere with the chemistry of MOF formation. So, if changing product distributions from catalytic or other processes is desired, a way to modulate the surroundings of the porphyrin core in MOFs must be found. This chapter explores the synthetic methodology to free up the *meso*-positions by instead placing linking groups in the β-positions, leaving the *meso*-regions for tuning of the porphyrin active site. To achieve this, it is first worth taking a step back and discussing the synthesis of pyrroles and subsequently porphyrins.

3.1.1 Synthesis of β-Substituted Pyrroles

Beyond their pivotal role in the synthesis of porphyrins, pyrroles have been widely studied for their pharmaceutical, photophysical, and electronic properties.[109–111] The parent compound, pyrrole is produced on an industrial scale by the reaction of furan with ammonia,[112] making it a cheap and abundant starting material for porphyrin synthesis. However, the fully unsubstituted pyrrole does not lend itself well to the synthesis of β-substituted porphyrins; regioselective modification of pyrrole is unnecessarily complicated due to the formation of unwanted side products (e.g., polypyrrole), especially when addition of multiple functional groups on the pyrrole is desired. On the other hand, functionalization at the β-positions of an already formed porphyrin is limited, and could be interfered with depending on the *meso*-substituents that are present. In order to circumvent these challenges, various synthetic methodologies have been developed that can be used to synthesize multi-substituted pyrroles by the assembly of two or more constituent parts. As β-substituted porphyrins are the end goal, focus will be primarily on those methods that produce pyrroles that best lend themselves to the synthesis of such porphyrins.

3.1.1.1 van Leusen Pyrrole Synthesis

The van Leusen pyrrole synthesis is an efficient method for the formation of 3,4-disubstituted pyrroles (Scheme 3.1). It involves the versatile tosylmethyl isocyanide (TosMIC, also known as the van Leusen reagent).[113–116]

In the overall reaction, TosMIC reacts with a Michael acceptor in the presence

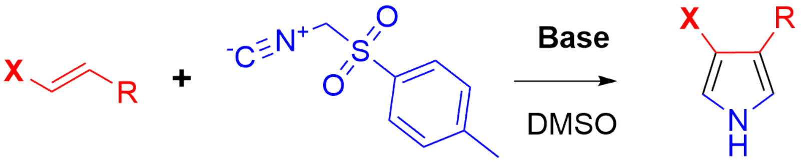

X = COOR, CN, NO_2
Base = NaH, t-BuOK

Scheme 3.1: van Leusen pyrrole synthesis.

of base to form the desired 3,4-disubstituted pyrrole product. A variety of electron-withdrawing groups have been successfully employed, such as nitro,[117] cyano,[118] alkoxycarbonyl,[119] and phenylsulfonyl.[120]

3.1.1.2 Barton-Zard Pyrrole Synthesis

In 1985, Derek Barton and Samir Zard reported on what would become one of the major powerhouses in the field of pyrrole synthesis.[121] Their methodology involves the reaction of α-isocyanoacetates, the most common being ethyl isocyanoacetate (EtICA), with nitroalkenes in the presence of base, akin to the prior van Leusen method, to afford 3,4-disubstituted pyrroles with carboxyester functionality at the 2-position.

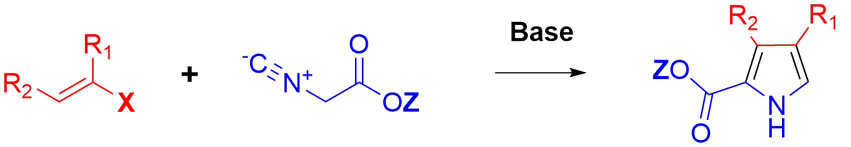

X = NO_2, SO_2Ph
Z = Me, Et, t-Bu, Bn
Base = DBU, t-BuOK

Scheme 3.2: Barton-Zard (BZ) pyrrole synthesis.

The remarkable simplicity of the BZ reaction (Scheme 3.2) coupled with the extensive scope and ease of synthesis of various starting nitroalkenes (or β-nitroacetates) has propelled its use in the synthesis of pyrrolic chromophores,[122] organic semiconductors,[123] and biologically active compounds.[124] In addition, the resulting pyrrole-2-carboxyesters have frequently been used to synthesize β-substituted porphyrins (vide infra), and were even used as precursors in the synthesis of highly conjugated, π-extended Por-MOF linkers.[125,126]

3.1.2 Synthesis of β-Substituted Porphyrins

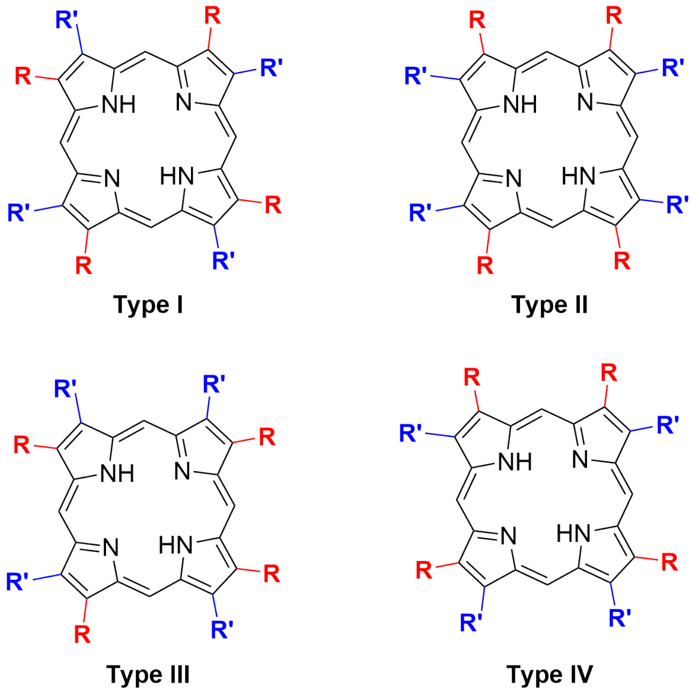

Type I **Type II**

Type III **Type IV**

Figure 3.2: β-substituted porphyrin isomers.

The synthetic strategies for the formation of porphyrins remain more or less the same regardless of whether *meso*-substituted or β-substituted porphyrins are desired. Nearly all modern methods involve the acid-catalyzed condensation of pyrroles (or pyrrolic oligomers) with aldehydes to form reduced porphyrins (e.g., porphyrinogens), which are subsequently oxidized to the final porphyrin. Some difficulty arises as the asymmetry of the desired porphyrin increases, leading to the formation of isomers such as the so-called ‘type-isomers’ of β-substituted porphyrins (Figure 3.2). Outlined in this section are methodologies that would be particularly applicable in the synthesis of porphyrinic MOF linkers.

3.1.2.1 Lindsey Method

The Lindsey method is one of the most widely used methodologies for the synthesis of porphyrins from mono-pyrrolic starting materials.[127] In this method, pyrroles and aldehydes are tetramerized to a porphyrinogen intermediate under acidic conditions (most commonly TFA or $BF_3 \cdot OEt_2$) at room temperature, and are subsequently oxidized to the aromatic porphyrin with quinone derivates (i.e., DDQ or chloranil) or with O_2 (Scheme 3.3). However, to achieve reasonable yields and simplify purification, it is preferred to use symmetric pyrroles and aldehydes, as well as choose symmetric porphyrins as targets. As the symmetry of either the starting materials or the desired the porphyrin decreases, the yields too will plummet in most cases and purification of complex isomeric mixtures is required. As such, the Lindsey method has primarily been applied to β-substituted porphyrins from symmetric starting pyrroles. Furthermore, if *meso*-free porphyrins are desired (i.e., by the use of formaldehyde), they are not reliably synthesized by this method.

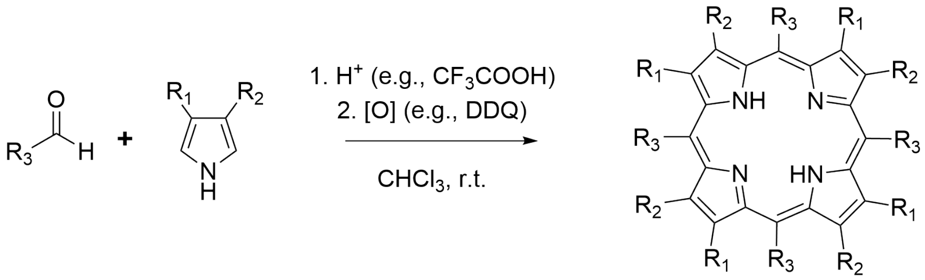

Scheme 3.3: Porphyrin synthesis via the Lindsey method.

3.1.2.2 Ono Method

An alternative tetramerization approach is possible through the use of pyrrole-2-carbinols, which in themselves already contain the necessary *meso*-carbon of the final porphyrin. This methodology was reported on extensively by Ono, who showed

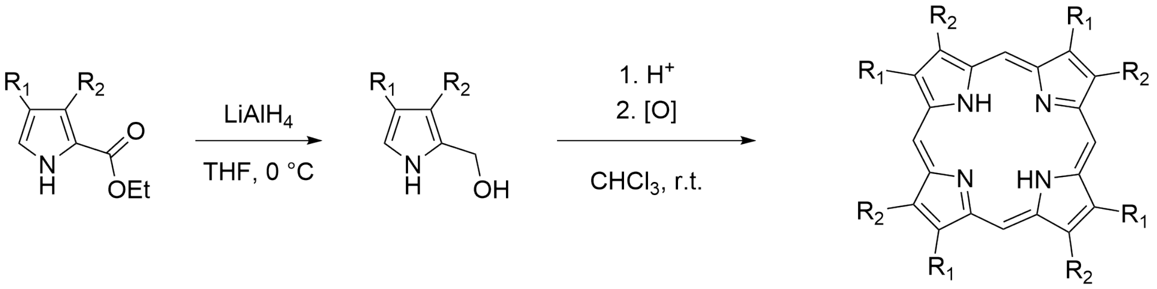

Scheme 3.4: Porphyrin synthesis via pyrrole-2-carbinol condensation.

that the ethyl pyrrole-2-carboxylates easily accessible by the BZ reaction could be converted to pyrrole-2-carbinols by reduction with LiAlH$_4$ and carried forward to cyclization without additional purification in an overall three-step, one-pot reaction (Scheme 3.4). This was shown to be a highly effective approach for the synthesis of β-substituted porphyrins, where the representative example OEP could be prepared in 50-70% yields.[128] Towards the synthesis of specific type-isomers (namely, type I porphyrins; see Figure 3.2) from unsymmetric pyrroles, Ono demonstrated that when one of the pyrrole substituents is a sufficiently bulky aryl group or strongly electron withdrawing (e.g., CF$_3$ or NO$_2$),[129–131] the type I isomer is formed selectively. However, when cyclization cannot be directed by sterics/electronics, this method suffers from isomeric scrambling, much like the Lindsey method.

3.1.2.3 [2+2] Condensation

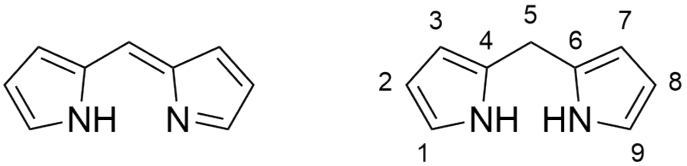

Figure 3.3: Structures of dipyrromethene (left) and dipyrromethane (right) with associated carbon numbering.

When greater control over the porphyrin type-isomer is desired, many choose a strategy involving a [2+2] condensation of dipyrrolic precursors, such as dipyrromethenes or dipyrromethanes (Figure 3.3). The present text will focus on the use of dipyrromethanes as this is the most compatible with the research in this chapter. The [2+2] approach has been extensively used in the synthesis of porphyrins bearing unsymmetrically substituted pyrrolic subunits, the most famous example being the so-called 'MacDonald' condensation of 1,9-unsubstituted dipyrromethane with 1,9-diformyldipyrromethane in AcOH with catalytic hydroiodic acid (Figure 3.4a).[132] After the original report, the [2+2] methodology has been applied to many different dipyrromethanes (Figure 3.4b), with reaction conditions resembling those of the Lindsey method. The central methylene often also bears a substituent, which allows for the synthesis of porphyrins with highly specific symmetries and functional group distributions.[133–137]

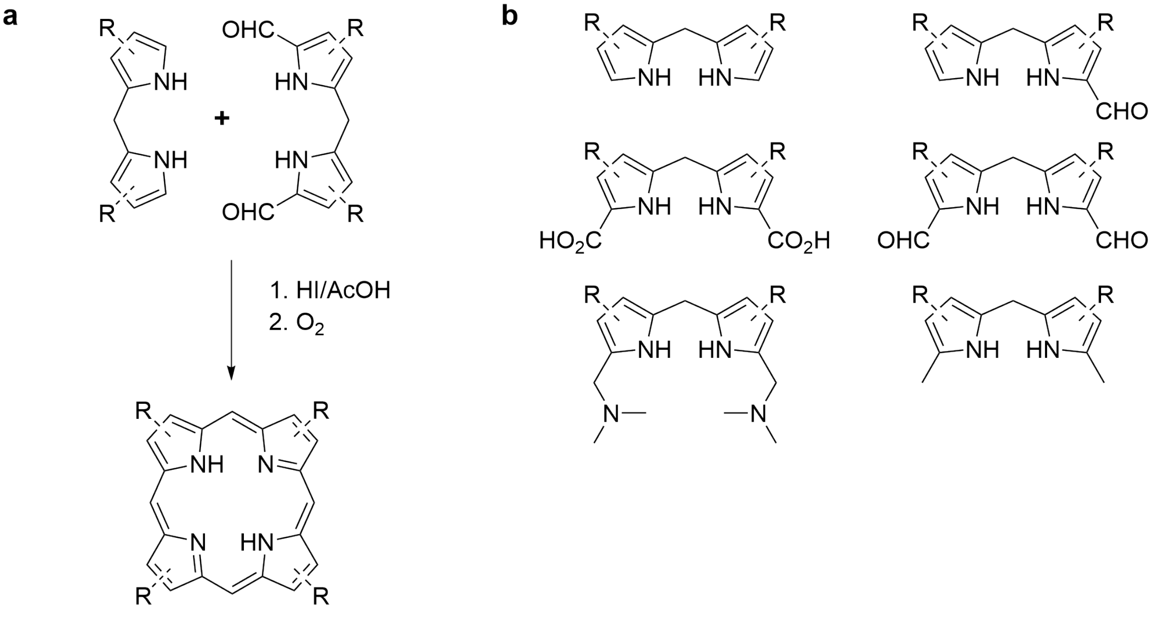

Figure 3.4: a) MacDonald [2+2] condensation of dipyrromethanes. b) Some examples of dipyrromethane precursors used in porphyrin synthesis.

With these synthetic tools, the goal of this research was to develop a methodology to synthesize porphyrins with linker moieties at the β positions. Importantly, this should be accomplished in a way that does not limit the tailorability of the porphyrin linkers themselves. Linking moieties, such as phenylcarboxylates, could be added to a porphyrin through means such as coupling reactions to β-halogenated porphyrins. However, this would decrease the overall scope of functionalities that could be introduced at the *meso* positions, as these functionalities might interfere with other reaction needed to modify the porphyrin. Thus, incorporating the linking moiety onto the pyrrolic precursor was crucial. Keeping this in mind, two families of porphyrin linkers were set as targets, shown in Figure 3.5.

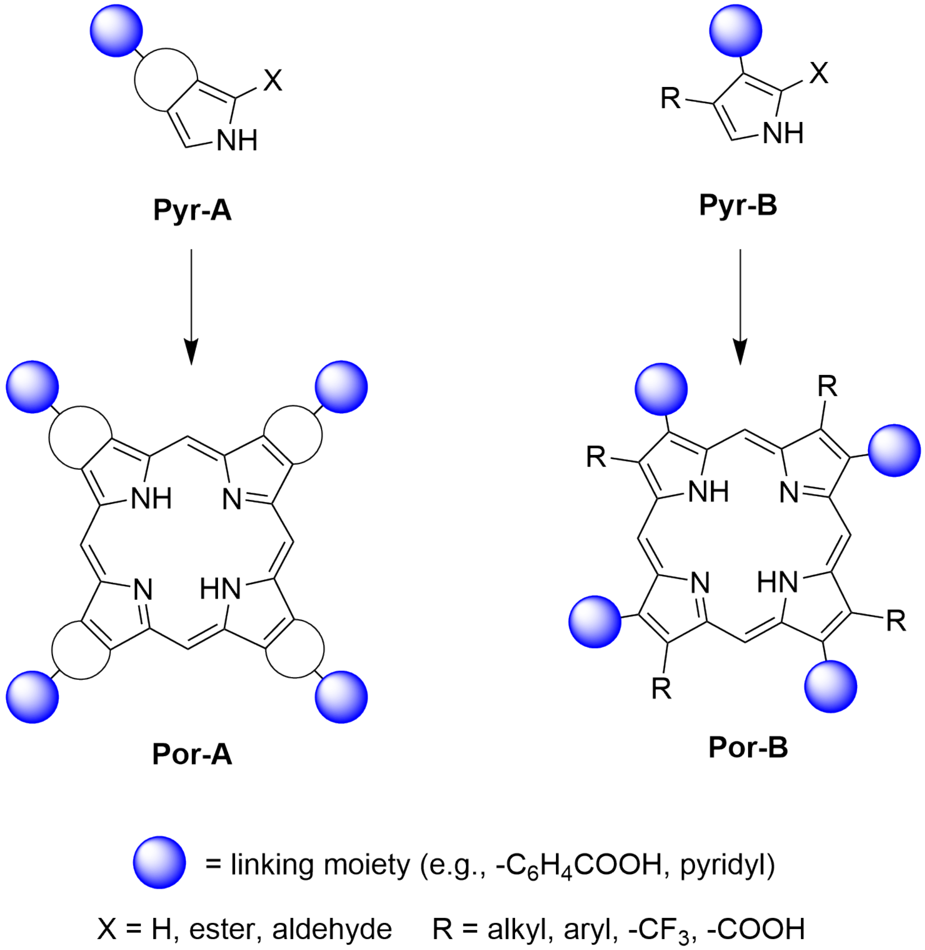

Figure 3.5: General form of target porphyrin linkers and associated pyrrole precursors.

Linkers of the type **Por-A** are highly symmetric (D_{4h}), as is often desired in MOF synthesis. This family was inspired by ongoing work in the Katz group on the synthesis of novel phthalocyanine linkers.[138] By introducing a fused ring on the starting pyrrole (**Pyr-A**) from which linking functionality can be appended in a symmetric fashion, many of the problems of isomerization during porphyrin synthesis can be avoided, at least at the β positions. The challenge then mostly lies on the synthesis of the starting pyrrole.

The second type of linker, **Por-B**, has the linking moiety extended from one of the two β positions of each pyrrolic subunit. In this family of potential linkers, the pyrrole precursor **Pyr-B** is synthetically easy to access, at the cost of being less symmetric than a pyrrole of the type **Pyr-A**. The decreased symmetry (C_{4h} or C_4, depending on substituents) introduces challenges in the porphyrin synthesis due to the higher probability of forming isomers, but at the current state of this research, it would be beneficial to investigate all of the possible isomers (see Figure 3.2) and what kinds of MOF structures can or cannot be formed.

3.2 Results and Discussion

3.2.1 Pyrrole Synthesis

The first synthetic target was a phenanthrolinopyrrole **1** (Scheme 3.5). Pyrrole **1** is appealing due to its molecular symmetry and accessibility through only a few synthetic steps, making it one of the easiest fused-ring pyrrole targets towards a **Por-A**-type porphyrin. The phenanthroline backbone could coordinate a variety of metals, and metallating the porphyrin linker could lead to a catalytically active, bi-metallic MOF. Synthesis began with a straightforward nitration of phenanthroline in refluxing H_2SO_4/HNO_3 to obtain 5-nitro-1,10-phenanthroline. From this, Lash's approach[139] was followed and a Barton-Zard reaction was performed in order to form pyrrole-2-carboxylate **1-e**. 5-Nitro-1,10-phenanthroline was dissolved in THF, and EtICA was added to the resulting solution. DBU (1,8-diazabicyclo[5.4.0]undec-7-ene) was added to the mixture, and it was left to stir overnight at room temperature.

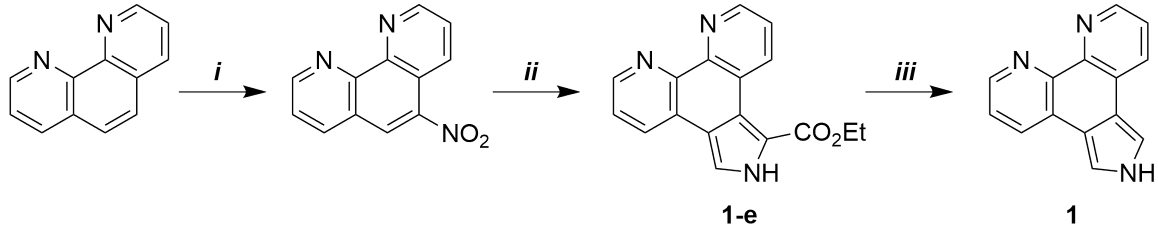

Scheme 3.5: Synthesis of phenanthrolinopyrrole **1**. *i*: H_2SO_4/HNO_3, Δ, 3 h; *ii*: EtOH, EtICA, K_2CO_3, r.t., overnight; *iii*: $(CH_2OH)_2$, KOH, Δ, 2 h.

Isolation of the desired pyrrole **1-e** gave unexpectedly poor yields (ca. 34%) compared to the 76% reported by Lash. Where all of the reagents used were recently purchased and were acceptably pure, the effect of solvent was investigated. It was at this point that a study by Palaniswamy and co-workers was found showing considerable decrease in yield of the BZ reaction when stabilized THF is used.[140] THF is commonly stabilized with BHT (butylated hydroxytoluene), a radical scavenger that prevents the formation of explosive THF-peroxides. Distillation of THF would easily remove the BHT stabilizer, though finding an alternative solvent would be a more convenient and safer option. To that end, following a report by Silyanova on the synthesis of pyrroles with electron-withdrawing substituents,[141] THF was replaced with EtOH. The report also mentioned K_2CO_3 as an effective base that could be used instead of DBU. This new solvent–base combination was very effective, giving acceptable yields (65-70%) of pyrrole **1-e**, and simplifying purification as the product could be precipitated out by addition of water. Finally, to remove the ethoxycarbonyl group and obtain the desired phenanthrolinopyrrole **1**, pyrrole **1-e** was heated at reflux in ethylene glycol in the presence of excess KOH. It is important to keep the system under nitrogen to prevent formation of polymeric side-products.

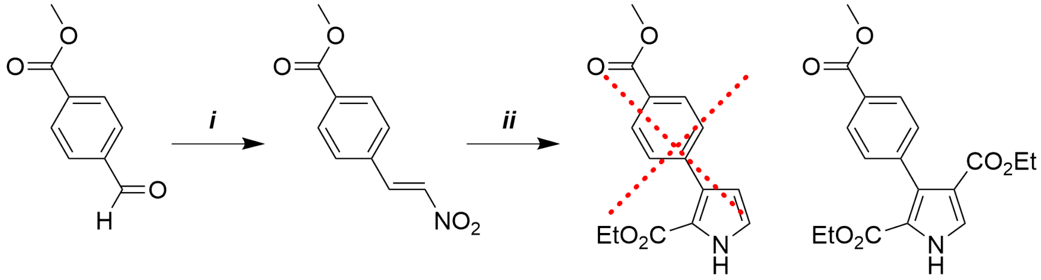

2 **3-e** **3'-e**

Scheme 3.6: Synthesis of ethyl 3-(*p*-methylbenzoato)pyrrole-2-carboxylate **3-e**. *i*: CH_3NO_2, NaOH, 0 °C; *ii*: EtOH, EtICA, K_2CO_3, r.t., overnight.

The second synthetic target was an asymmetric pyrrole of the type **Pyr-B** (Figure 3.5). The simplest pyrrole of this type that could be envisioned was ethyl 3-(*p*-methylbenzoato)pyrrole-2-carboxylate **3-e**. The synthetic pathway began with a nitroaldol reaction of nitromethane with methyl *p*-formylbenzoate (Scheme 3.6). The two substrates were dissolved in MeOH and treated with an aqueous NaOH solution at 0 °C. The solution was stirred for an hour before neutralization with HCl, at which point the desired nitroalkene **2** precipitated out of solution and was collected by suction filtration (ca. 75% yield). Nitroalkene **2** was then subject to the BZ reaction under the same conditions that were used to form pyrrole **1-e** (i.e., EtOH as solvent and K_2CO_3 as base).

Unlike pyrrole **1-e**, no precipitate was observed on the addition of water. Instead, an opaque tan-coloured colloid was formed. Extraction of the solution with EtOAc and subsequent solvent evaporation left a crude oil that was subsequently chromatographed. The earliest eluting fractions contained a pyrrolic compound as determined by ^{1}H NMR, though surprisingly it was not the expected pyrrole **3-e**. In the ^{1}H NMR spectrum (Figure 3.6), there are two overlapping quartets centered at δ 4.12 and 4.10, as well as the corresponding triplets at δ 1.10 and 1.05, indicating the

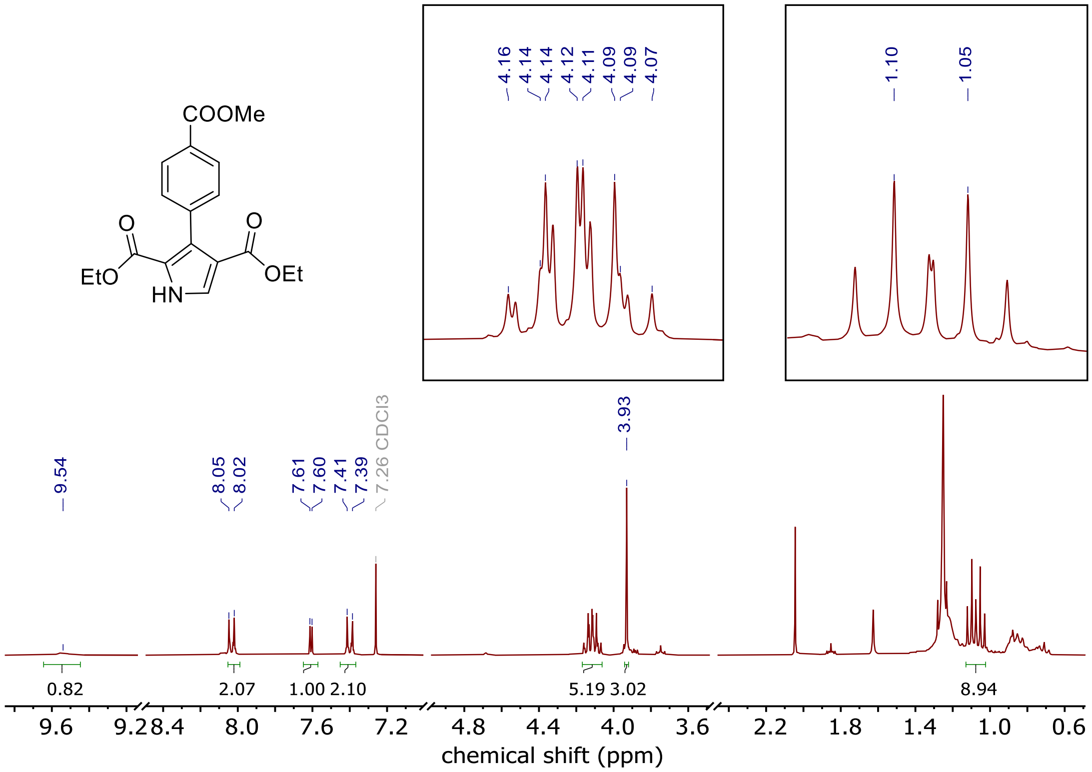

Figure 3.6: ^{1}H NMR spectrum (300 MHz, $CDCl_3$) of evaporated fractions containing pyrrole **3′-e**. Insets are expansions of the quartets/triplets of the esters. The third quartet visible in the inset is assigned to residual EtOAc.

presence of two ethyl esters, rather than just the one expected. This is consistent with diethyl pyrrole-2,4-dicarboxylate **3′-e**. The same sort of compounds were observed by Samet and coworkers in their synthesis of 3,4-diarylpyrroles.[142] They propose a secondary pathway to the typical BZ cyclization (Scheme 3.7), where after initial attack by EtICA, loss of a nitroalkylate moiety leads to addition of a second isocyanide, with subsequent liberation of cyanide and a 1,3-proton shift resulting in the formation of the pyrrole diester.

Although not the intended product, pyrrole **3′-e** would be an appealing substrate to explore further in the formation of porphyrin linkers. However, investigation of this molecule was not carried out further. Instead, a derivative based on the parent pyrrole

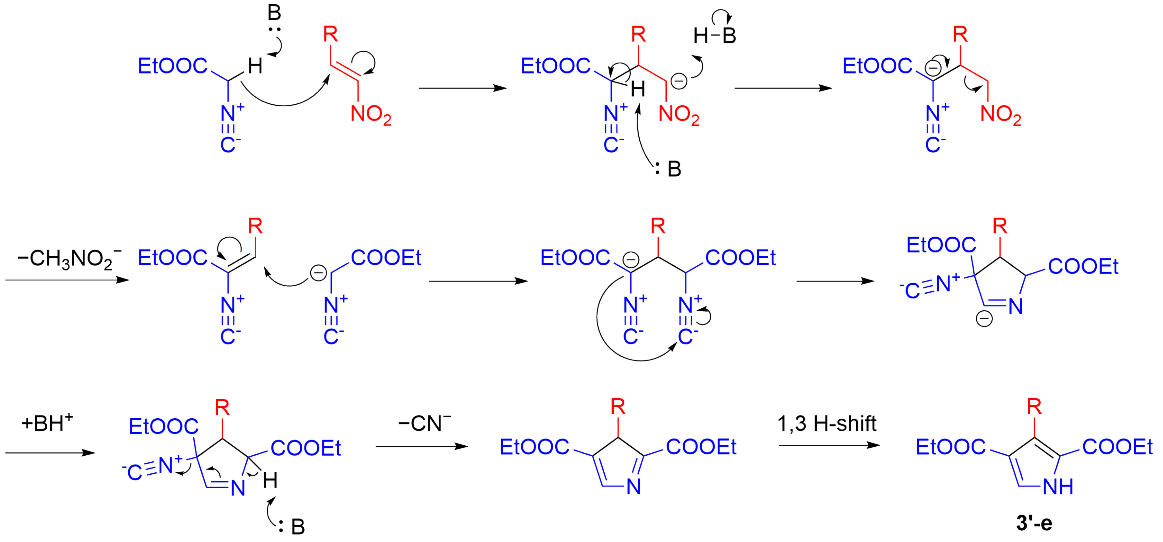

Scheme 3.7: Proposed mechanism for the formation of pyrrole diester **3′-e**.

3-e was chosen, namely ethyl 4-ethyl-3-(*p*-methylbenzoato)pyrrole-2-carboxylate **5-e** (Scheme 3.8). Introduction of an alkyl group at the 4-position significantly decreases formation of the diester byproduct, and a 4-ethyl group was chosen due to the readily available 1-nitropropane starting material.

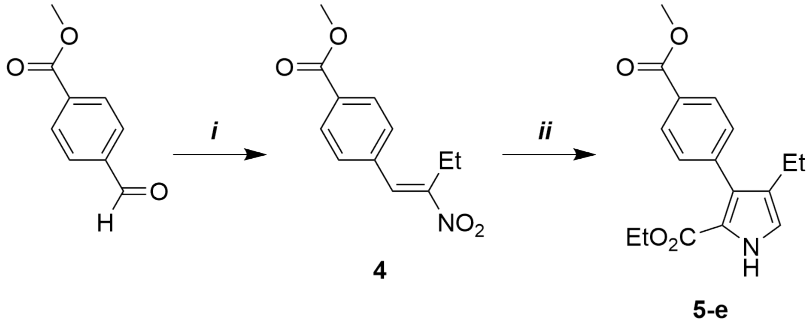

Scheme 3.8: Synthesis of ethyl 4-ethyl-3-(*p*-methylbenzoato)pyrrole-2-carboxylate **5-e**. *i*: $PrNO_2$, NH_4OAc, AcOH, Δ, overnight; *ii*: *i*-PrOH, EtICA, DBU, r.t., overnight.

As with the other pyrroles, the first step is to prepare the nitroalkene substrate for the BZ reaction (Scheme 3.8). In this case, nitroalkene **4** was prepared by a nitroaldol reaction between methyl *p*-formylbenzoate and 1-nitropropane. Then the proceeding BZ reaction was carried out overnight in isopropanol with DBU as base.

After completion of the BZ reaction, the reaction mixture was poured into a dilute HCl solution, then extracted with EtOAc. This time, chromatographic separation afforded the pyrrole **5-e**, without appreciable amounts of diester. After multiple syntheses of pyrrole **5-e**, a more convenient purification was found and chromatography could be avoided entirely. After extraction with EtOAc, the solvent was evaporated and the residue was triturated with hexanes. Finally, the solution of **5-e** in hexanes was filtered through celite, and subsequent evaporation gave the pyrrole **5-e** in a 64% yield.

Overall, the BZ reaction has proved to be an effective means to access β-substituted pyrroles which will act as precursors to porphyrinic MOF linkers. Expanding the family of linkers will, for the most part, only be limited to the nitroalkenes that are accessible.

3.2.2 Porphyrin Synthesis

With two pyrroles synthesized, the next goal was the synthesis of the desired porphyrins. Returning first to phenanthrolinopyrrole **1**, I was immediately met with an uphill battle. Shortly after the synthesis of **1**, a report by Lash was found that outlined that the desired tetraphenanthrolinoporphyrin could not be formed,[143] at least under the conditions intended to be used. Due to the fused-ring system of **1**, porphyrin formation is drastically reduced as the pyrrole subunit no longer has enough electron density to carry out the necessary bond forming steps. Nonetheless, I decided to at the very least attempt a synthesis with modified conditions that, to my knowledge, had not yet been applied to pyrrole **1** (Scheme 3.9). As there are known phenanthroline-fused, dipyrrolic compounds,[144] it is evident that bond formation at the pyrrole α position is not entirely prevented. Following standard Lindsey con-

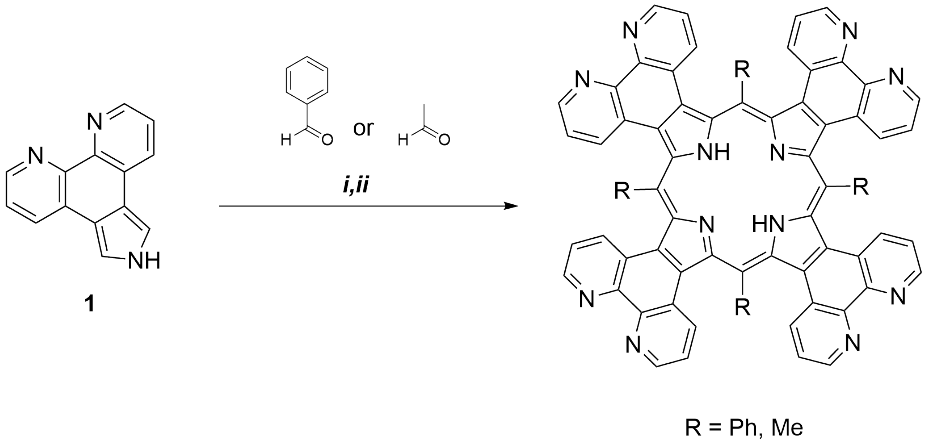

Scheme 3.9: Attempted synthesis of tetraphenthrolinoporphyrin. *i*: aldehyde, K10, DCM, N_2, Δ, 90 min; *ii*: DDQ, Δ, 60 min, then r.t., overnight.

ditions, benzaldehyde and **1** were mixed in dry, degassed DCM. Then, following a method by Kikkawa et al.,[145] Montmorillonite-K10 clay (K10) was used as acid catalyst. K10 is an acid-treated aluminosilicate clay that has found use in the synthesis of porphyrins where traditional acids (i.e., TFA or $BF_3 \cdot OEt_2$) have been ineffective. It has been hypothesized that the reason for K10's effectiveness lies in its mesoporosity and pore structure,[146,147] leading to an environment where higher pyrrolic oligomers are disfavoured over cyclization of four pyrrole units. Aldehyde, **1**, and K10 were heated at reflux under N_2 for 90 min, with the flask covered in foil to prevent exposure to light. After this time, the flask was cooled, opened to air, and DDQ was added. The solution was then returned to reflux for an additional 60 min before being left to stir at room temperature overnight. The next day, the dark red solution was filtered through a short plug of celite to remove the K10 before evaporating the solvent under vacuum. The dark residue was chromatographed on silica gel with $CHCl_3$. Good separation could not be achieved, and TLC of the fractions showed a complex mixture of numerous products. Moreover, porphyrinic products were unable to be detected by ^1H NMR in any of the coloured fractions. Porphyrins can often be detected by peaks in the δ 9–10 region (corresponding to *meso* protons) and the telltale

NH peaks at $\delta < 0$, all of which were absent here. The same synthesis was repeated with acetaldehyde, as it was believed that this would reduce the steric strain of the porphyrin, though again no porphyrin products could be isolated.

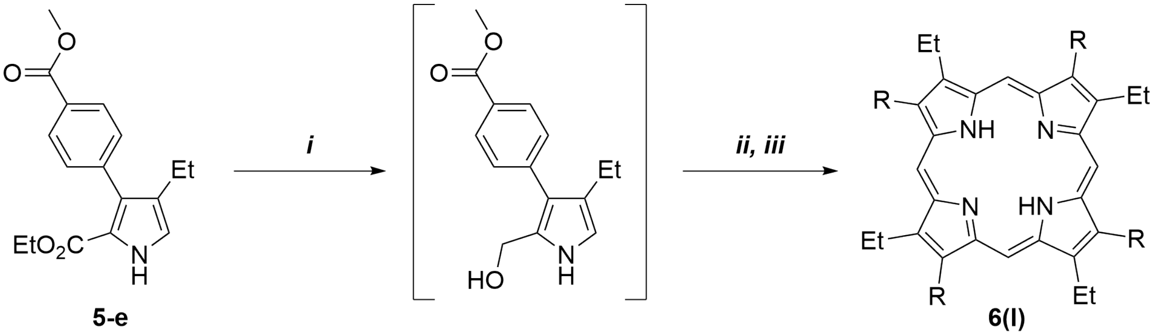

Scheme 3.10: Synthesis of porphyrin **6(I)**. R = $-C_6H_4COOMe$. *i*: $LiAlH_4$, THF, 0 °C, 2 h; *ii*: p-TsOH, DCM, r.t, overnight; *iii*: DDQ, r.t., 6 h.

Given what was experienced with **1** and the literature precedent that indicates this chemistry was not successful, I turned my attention to pyrrole **5-e**, which was expected to be better suited to forming a desired porphyrin. With this pyrrole in hand, some preliminary attempts at porphyrin syntheses following the method popularized by Ono were conducted (Scheme 3.10). Pyrrole **5-e** can be converted to a 2-hydroxymethyl pyrrole via reduction with $LiAlH_4$. This pyrrole is then carried forward without isolation to an acid-mediated tetramerization that should result in the desired C_{4h}-symmetric porphyrin (**6(I)**). In a typical reaction, **5-e** was dissolved in THF and added to a stirred solution of $LiAlH_4$ in THF at 0 °C. Once reacted (ca. 2 h), the solution is quenched with EtOAc, poured into a dilute HCl solution, and extracted with DCM. The organics were dried with $MgSO_4$, and acid (*p*-TsOH) was added to the solution after covering the reaction vessel with foil to protect it from light. After stirring overnight at room temperature, DDQ was added to oxidize any porphyrinoid species present (stirred ca. 6 h). Finally, the solution was washed with a $NaHCO_3$ solution prior to purification by column chromatography.

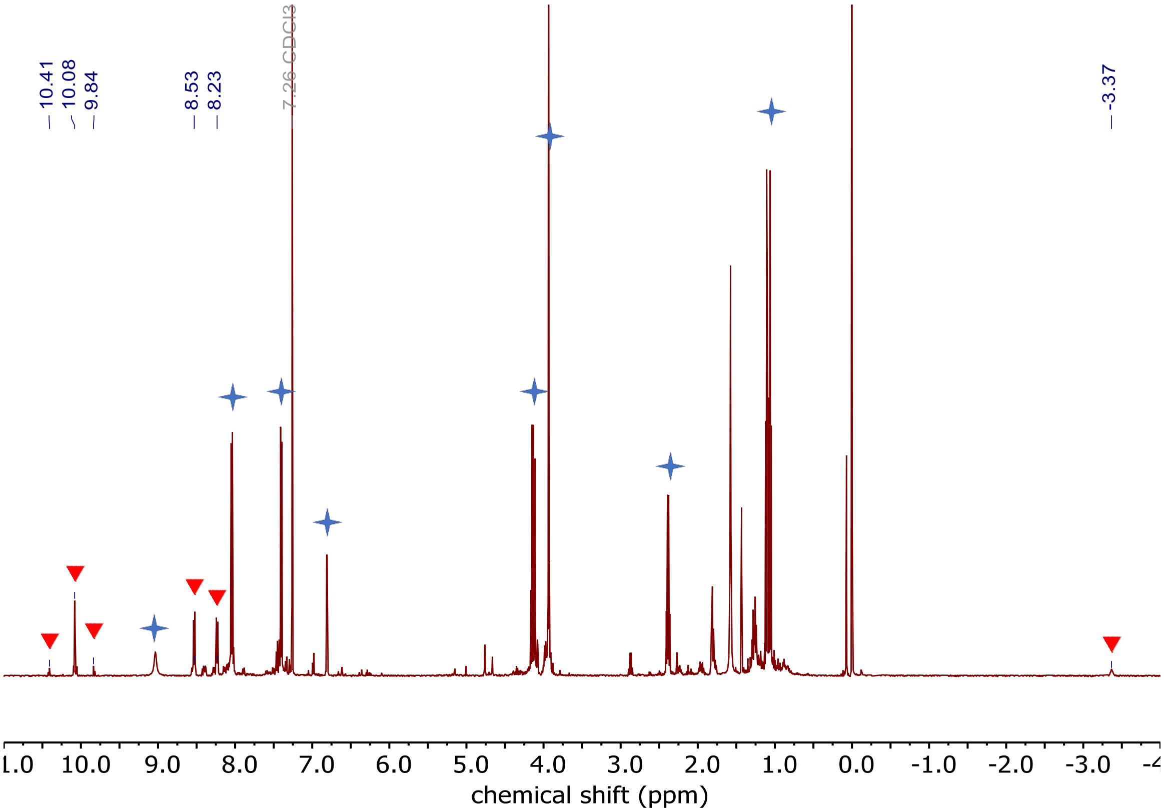

Figure 3.7: Crude ^{1}H NMR (500 MHz, $CDCl_3$) of first attempted porphyrin reaction with **5-e**, after column. Red downward triangles indicate peaks that associated with porphyrin products. Blue crosses indicate peaks of starting material **5-e**.

^{1}H NMR of the collected fractions confirmed the formation of porphyrin products (Figure 3.7), as seen by the *meso*-H peaks in the downfield region around δ 10 and the upfield shifted NH protons at around δ -3, caused by the aromatic ring-current of the porphyrin. Furthermore, even after column chromatography there was a considerable amount of starting material present. This indicates that the first reduction step with $LiAlH_4$ was incomplete, either due to too much residual water in the solvent, or insufficient reaction time. It also appears that some amount of isomeric scrambling occurred during the reaction, as multiple peaks are visible in the *meso*-H region. Nonetheless, the major porphyrinic component that was isolated in this fraction appears to be the target porphyrin **6(I)** (Scheme 3.10). This is evidenced by the prominent singlet at

δ 10.08, which only highly symmetric type I porphyrins would possess.

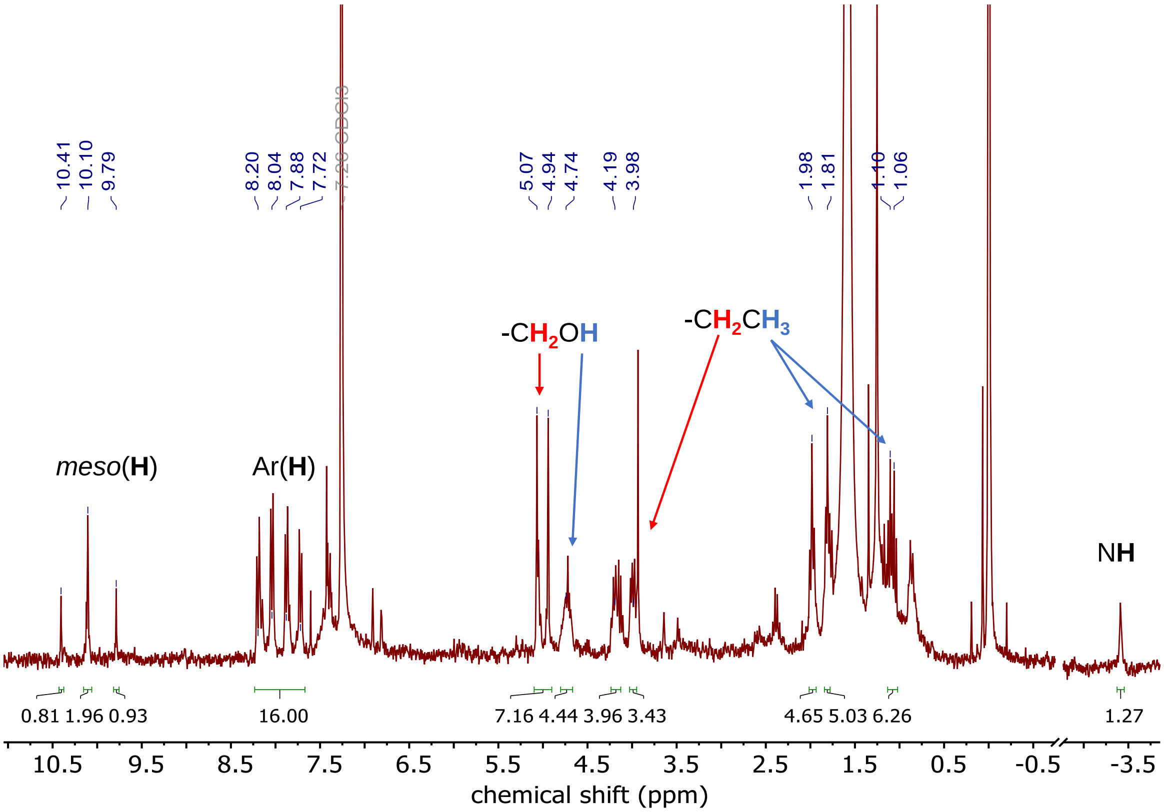

Figure 3.8: ^{1}H NMR spectrum (300 MHz, $CDCl_3$) of crude **6′(IV)**. Further purification of this sample was not attempted.

Spurred on by this promising result, the next attempt used a larger excess (1.6 equiv.) of $LiAlH_4$ to account for any adventitious water in the solvent. The rest of the reaction was carried out as mentioned above. This time, there was considerably less leftover pyrrole **5-e**. However, the amount of $LiAlH_4$ used resulted in the over-reduction of **5-e**. From the ^{1}H NMR of the major fraction from column chromatography (Figure 3.8), the peaks at δ 4.94 and 5.07 suggest that the methoxycarbonyl groups of the aryl moieties were reduced to the corresponding alcohols by the excess $LiAlH_4$. Instead of the target porphyrin **6(I)**, the spectrum was consistent with C_{2v}-symmetric porphyrin **6′(IV)**, shown in Figure 3.9. The type-IV isomer characteristically possesses three *meso*-H peaks in a 1:2:1 ratio (Figure 3.8).

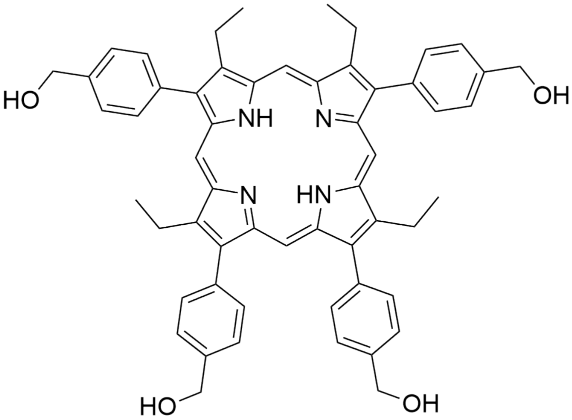

Figure 3.9: Structure of the proposed type-IV porphyrin **6′(IV)**.

Overall, the results from the attempted monopyrrole tetramerizations showed that it was possible to synthesize **6(I)** in this way. It is clear that the reduction step needs to be optimized in order to maximize the amount of pyrrole-2-carbinol that is formed while minimally reducing the aryl esters. This could perhaps be accomplished with increased reaction time at the first step, rather than increasing the $LiAlH_4$ concentration. Unfortunately, further explorations of this synthetic pathway were hindered by the time constraints imposed by the COVID-19 pandemic. It was decided that with the limited time available, it would be beneficial to explore synthetic pathways that lend themselves to a more directed porphyrin synthesis, with fewer opportunities for isomer formation (i.e., simplifying the isolation/purification of the target porphyrin).

3.2.3 Dipyrromethane Route

Another strategy for the synthesis of porphyrins is through a [2+2] condensation of dipyrromethanes, as was discussed earlier in this chapter. This approach could potentially be useful, as it would allow for a specific porphyrin isomer to be targeted and reduce isomeric scrambling as compared to typical monopyrrole tetramerization, thus in turn simplifying the purification. Using the previously synthesized pyrrole

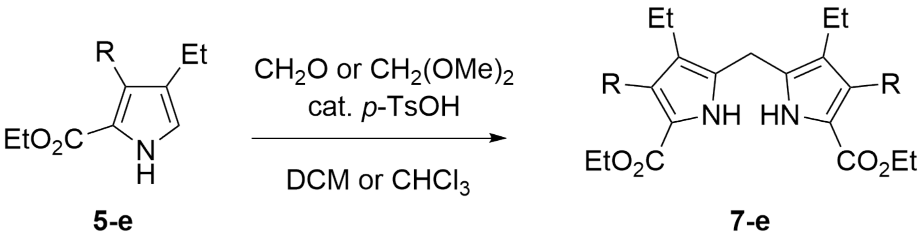

Scheme 3.11: Synthesis of dipyrromethane **7-e**. R = $-C_6H_4COOMe$. *i*: CH_2O, p-TsOH, DCM, Δ, overnight; *ii*: $CH_2(OMe)_2$, p-TsOH, $CHCl_3$, N_2, r.t., 4 d.

5-e, the synthesis of *meso*-free dipyrromethane **7-e** was explored, using the ethoxycarbonyl groups as a directing group to ensure the configuration of the β-substituents (Scheme 3.11). Attempting the dimerization of **5-e** with formaldehyde in refluxing MeOH and HCl did not proceed at all, with only starting materials able to be recovered. Changing the solvent to refluxing DCM and using *p*-TsOH as a catalyst, a new compound could be detected by TLC. Curiously, the spot on the TLC plate changed colour over time, gradually changing from colourless to a vibrant pink over several minutes. This colour change was not observed on silica gel typically used for column chromatography, so instead it was believed that the fluorescent additive on the TLC plates may be responsible. The fluorescent backing of typical TLC plates contains zinc silicate (Zn_2SiO_4) as the fluorophore, and indeed reports were found documenting the formation of zinc complexes with porphyrins and natural pheophytins when exposed to fluorescent backed TLC plates.[148,149] The pink colour is believed to appear as the compound coordinates zinc ions on the TLC plate. ^{1}H NMR was used to confirm that this compound is the desired dipyrromethane **7-e**. The symmetry of **7-e** results in an NMR spectrum which greatly resembles that of starting pyrrole **5-e** (Figure 3.10), with the main discerning feature being the disappearance of the doublet at δ 6.82 (α proton of **5-e**), and the subsequent appearance of the singlet at δ 4.02 (*meso* methylene of **7-e**).

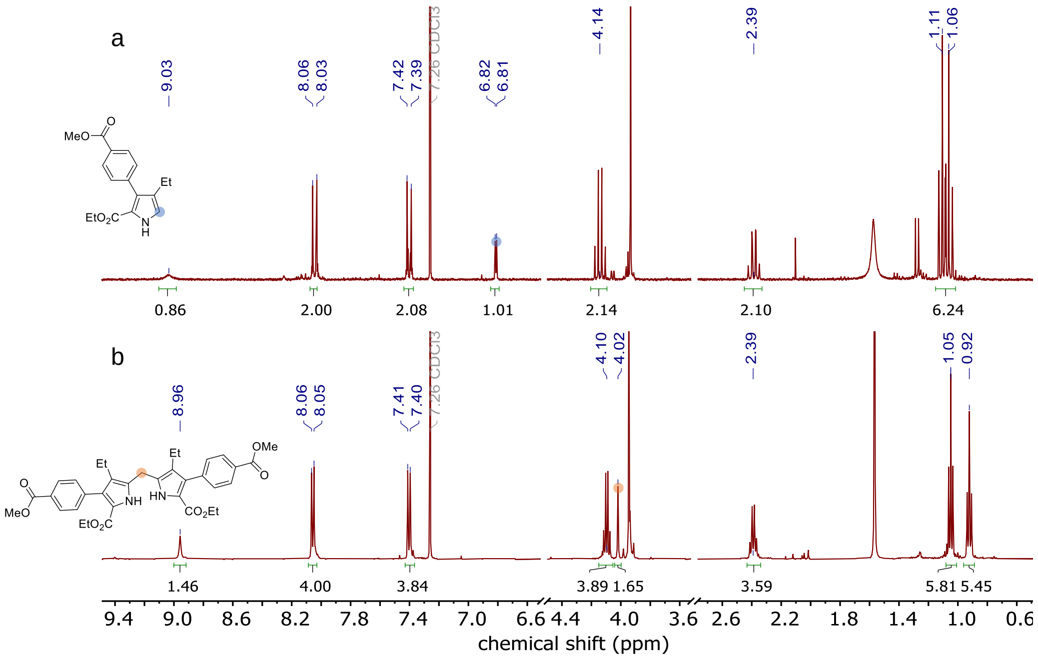

Figure 3.10: ^{1}H NMR spectra of a) **5-e** (300 MHz) and b) **7-e** (500 MHz).

In an effort to increase the yield of **7-e**, a method in which formaldehyde is substituted for dimethoxymethane (methylal) was followed.[128,150,151] Pyrrole **5-e** was first dissolved in N_2-degassed $CHCl_3$, then methylal (ca. 2 equiv.) and *p*-TsOH were added. The mixture was left to stir over a few days under N_2 at room temperature, after which the solution was concentrated and chromatographed to afford **7-e**. The final yield of **7-e** was 34%, which was enough to try further reactions, though it would likely be possible to increase this yield by heating the reaction and/or using a greater amount of methylal, as some starting material remained. Nonetheless, from this point the synthesis of porphyrin **6(II)** (Scheme 3.12) could be attempted.

The synthetic method follows a report by Semeikin et al. where they synthesize a variety of *meso*-free and 5,15-disubstituted porphyrins from dipyrromethanes.[152] In their report, dipyrromethanes or their corresponding 1,9-dicarboxylic acids were condensed with triethyl orthoformate (i.e., $CH(OEt)_3$) in the presence of TFA to afford type-II porphyrins in moderate to high yields. The first attempt was a condensation

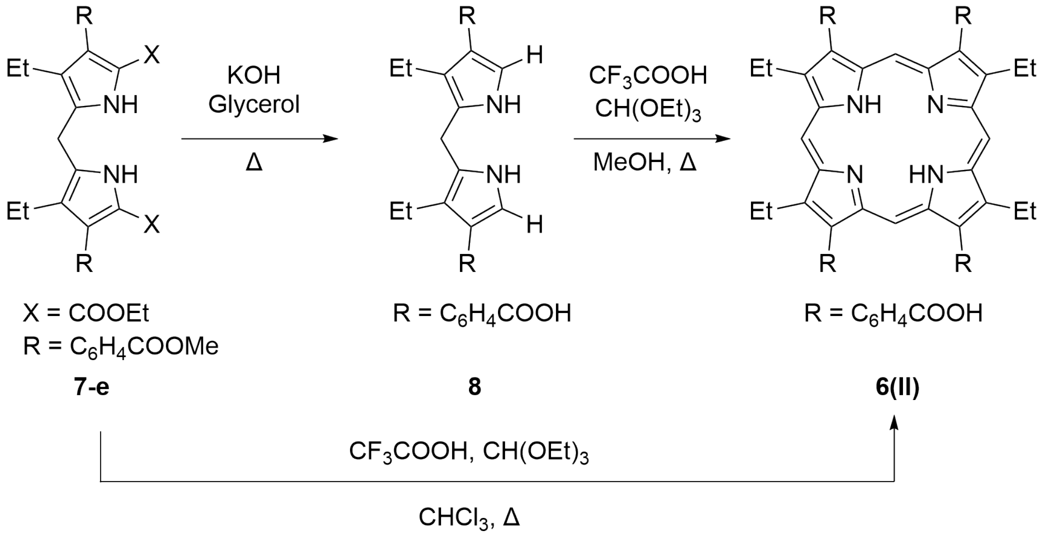

Scheme 3.12: Attempted pathways to porphyrin **6(II)**.

directly with **7-e** (Scheme 3.12), though only the starting dipyrromethane could be recovered, with no obvious traces of porphyrin. It was clear that the ethyl esters were not reactive enough under these reaction conditions, and instead the α-free dipyrromethane **8** would be needed in order to promote cyclization (Scheme 3.12). Saponification and decarboxylation was accomplished in one pot simply by heating **7-e** in glycerol in the presence of KOH (ca. 10 equiv.). After 1-2 h, the reaction was cooled and neutralized with HCl, after which **8** was obtained by extractive workup with $CHCl_3$.

Complications arose with this method, as the ester moiety of the aryl group was also saponified to the carboxylic acid. Attempts to take **8** onward to porphyrin **6(II)** resulted in complex, inseparable mixtures. From a purification point of view, having free carboxylic acids on the porphyrin would make chromatography on silica gel difficult due to the significant amount of streaking and propensity for the compound to stick to the stationary phase. In addition to the complicated mixtures, no traces of actual porphyrin products could be detected by ^{1}H NMR. It is clear that free carboxylic acids significantly hinder the porphyrin synthesis. Thus, to move forward with this method it will be important to preserve the ester moieties on the aryl groups of the dipyrromethane.

3.3 Conclusions and Future Work

The research in this chapter has served as a foray into the synthesis of β-substituted porphyrin MOF linkers. Although isolation of a potential linker was ultimately unsuccessful, the work herein shows that it is possible to form these linkers and the groundwork has been laid to accomplish this. The most promising method explored was the tetramerization of pyrrole-2-carbinols. Although they were not isolated, ^{1}H NMR showed that at least two porphyrin isomers of interest (**6(I)** and **6′(IV)**; see Scheme 3.10 and Figure 3.9) could be formed from this reaction. Optimization of the reduction that leads to the carbinols would be the most straightforward way of accessing these porphyrins, in particular **6(I)**. Moreover, the [2+2] condensation method is a promising route to the type-II porphyrin linker, as the precursor dipyrromethanes have been shown to be easily accessible. The difficulties that presented themselves when it came to actually performing the condensation can be addressed with some careful planning of the synthetic steps leading up to the condensation. These considerations, as well as some discussion on the inevitable synthesis of Por-MOFs, are presented below.

3.3.1 Improving the [2+2] Condensation Route

Although the [2+2] condensation attempted did not lead to porphyrin products, this was most likely caused by the free carboxylic acids. It is known from the tetramerization described above that when the carboxylic acids on the aryl groups are protected, there are no issues in forming the porphyrin (see Figure 3.7). A solution would then be to protect the phenylcarboxylic acids on **8** prior to condensation. The difficulty here lies in the general instability of α-free pyrroles/dipyrromethanes under typical esterification conditions (i.e., refluxing in alcohol with catalytic acid). Alternative conditions can selectively protect the phenylcarboxylic acids without other side reactions, though this would require the use of highly toxic and explosive diazomethane.[153]

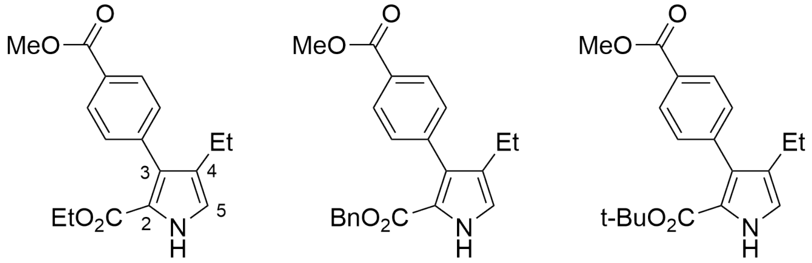

5-e **5-e-Bn** **5-e-tBu**

Figure 3.11: Structures of pyrroles with differing ester groups at the 2-position.

Taking a step back, the challenge in this chemistry is ultimately due to the two different esters in this molecule. The phenylcarboxyester (i.e., the eventual linking moiety) at the 3-position (Figure 3.11) must remain as an ester until after the completion of porphyrin formation. Meanwhile the ester at the 2-position needs to eventually be cleaved in order to perform the [2+2] condensation. In the tetramerization approach, the ethyl ester of pyrrole **5-e** was more reactive and could be selectively reduced to the alcohol under the right conditions (referring back to Scheme 3.10). However, under the conditions used to deprotect/cleave the ethyl ester prior to dipyrromethane condensation, the methyl ester was also deprotected. Thus, to preform the desired chemistry, a proposed solution is to install an ester group at the 2-position of the pyrrole, which has different chemical reactivity compared to the phenylmethoxycarbonyl group.

The key step that introduces the ester moiety at the 2-position is the BZ reaction. Specifically, the isocyanoacetate used will determine what kind of ester is left on the resulting pyrrole (see Scheme 3.2 in the introduction to this chapter). For the chemistry that is being pursued here, benzyl isocyanoacetate (BnICA) and *tert*-butyl isocyanoacetate (t-BuICA) are the most appealing. While they are commercially available, their very high cost (e.g., \$700 CAD/5 mL for t-BuICA from Sigma-Aldrich) makes it important to know how they can be accessed synthetically. One method is the conversion of one isocyanoacetate ester to another (Scheme 3.13). For example, an alkali metal isocyanoacetate can be generated from EtICA, and subsequent reaction with the corresponding bromide will afford the desired ester.[154,155] Alternatively, a direct synthesis can be accomplished via the dehydration of the corresponding *N*-formylglycinates which themselves are accessible from the naturally abundant amino-acid glycine (Scheme 3.13).[156–158]

Scheme 3.14 demonstrates the advantage that is gained with these different ester groups. Benzyl esters can be converted to carboxylic acids through catalytic hydrogenation, a reaction that will leave the methyl ester of the aryl group unaffected.[159–161] These carboxylic acid groups can subsequently be cleaved with simple heating. On the other hand, *tert*-butyl pyrrole-2-carboxylates can be completely cleaved in one step upon treatment with TFA,[162–164] again leaving the methyl ester untouched. Regardless of which ester is used, both cases result in the 1,9-unsubstituted dipyrromethane

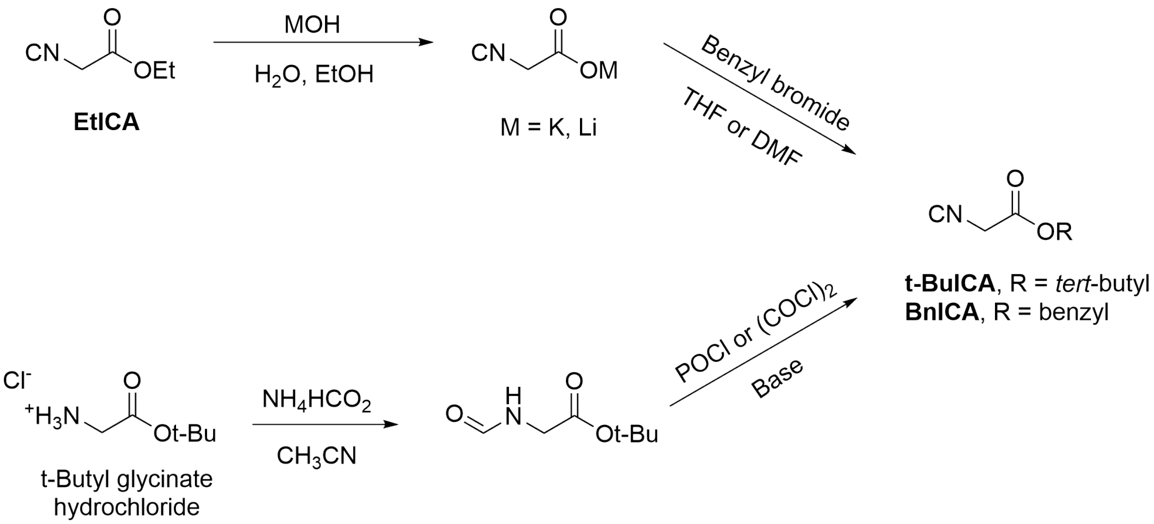

Scheme 3.13: Synthetic routes to other isocyanoacetate esters.

8′ (Scheme 3.14). With **8′**, the [2+2] condensation can be done without the interference of free carboxylic acids that was experienced with **8**. This modification should greatly improve the yield and isolation of the desired porphyrin linker.

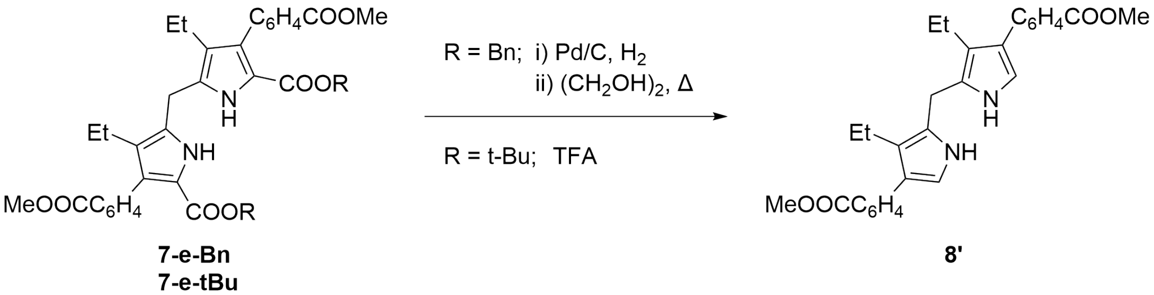

Scheme 3.14: Decarboxylation steps of proposed 1,9-dicarboxyester dipyrromethanes.

3.3.2 Synthesis of Por-MOFs

Perhaps the best outcome from the work that could be performed was the confirmation that porphyrins such as **6(I)** could indeed be formed. Once the synthetic conditions are optimized, it is inevitable that linkers such as those in Figure 3.12 will become available. As such, we should look toward the formation of MOFs with

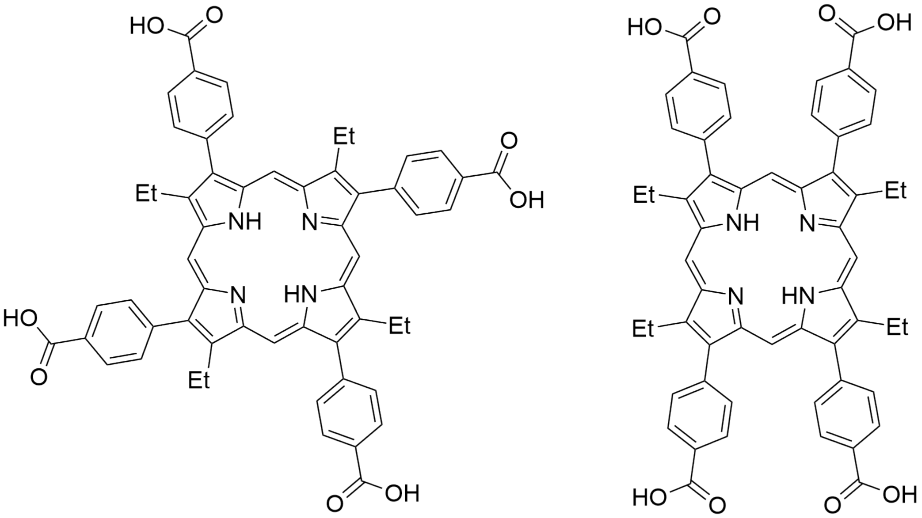

PML1 **PML2**

Figure 3.12: Porphyrinic MOF linkers obtainable through the methods herein.

these linkers and their impact on the MOF properties. A logical starting place would be to look at the synthetic conditions of the PCN (Porous Coordination Network) family of MOFs. Many MOFs in the PCN family feature *meso*-substituted porphyrin linkers (recall Section 1.4.2 of Chapter 1). For example, PCN-221 through 225 are all Zr-based TCPP-linked MOFs, which vary in their structural topologies. Accessing these different topologies can be done by changing the temperature at which the synthesis is carried out, or by using different modulators during the synthesis (recall that modulators are acids added to the synthesis which compete with the linkers in the coordination of the MOF nodes). In addition, Zr-based MOFs are known to be relatively stable compared to MOFs with other metal nodes. I believe trying to synthesize a Zr-based MOF with **PML1** or **PML2** will give a good chance of forming a robust material that can be explored in the future.

3.4 Experimental

3.4.1 Materials and Methods

Unless otherwise noted, reagents used herein were purchased from commercial sources and used without further purification.

^{1}H nuclear magnetic resonance (NMR) data were collected on either a Bruker AVANCE 500 MHz spectrometer using an inverse probe or a Bruker AVANCE III 300 MHz spectrometer, as noted in the text.

3.4.2 Synthesis

Only compounds that were isolated are described here.

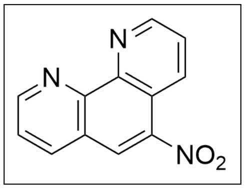

5-Nitro-1,10-phenanthroline:[165]

Phenanthroline (5.21 g, 28.9 mmol) was dissolved in conc. H_2SO_4 (30 mL) and was added dropwise to conc. HNO_3 (15 mL). The solution was heated with stirring to 160 °C for 3 h, after which the solution was poured into ice water, and NaOH (sat., aq.) was added until pH 3. The resulting pale yellow precipitate was collected via vacuum filtration, washed with water and dried in air (4.10 g, 63%). ^{1}H NMR (500 MHz, DMSO-d_6) δ 9.44 (dd, J = 1.6, 4.7 Hz, 1H), 9.40 (dd, J = 1.4, 4.5 Hz, 1H), 9.18 (dd, J = 1.4, 8.6 Hz, 1H), 9.15 (dd, J = 1.4, 8.2 Hz, 1H), 8.23 (m, J = 2.8 Hz, 2H).

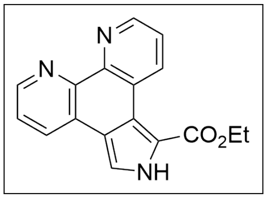

Phenanthrolinopyrrole (1-e):[139]

5-Nitro-1,10-phenanthroline (225 mg, 1.00 mmol) was suspended in EtOH with stirring, and EtICA (110 µL, 1.00 mmol) was then added. To this mixture, K_2CO_3 (276 mg, 2.00 mmol) was added and the mixture was stirred overnight at room temperature. After the elapsed time, water was added and a tan-coloured solid precipitates from solution. This solid was collected by vacuum filtration, washed with water and dried in air (198 mg, 68%). ^{1}H NMR (300 MHz, DMSO-d_6) δ 13.08 (bs, 1H), 10.06 (dd, J = 1.7, 8.3 Hz, 1H), 8.93 (dd, J = 1.7, 4.3 Hz, 1H), 8.88 (dd, J = 1.7, 4.3 Hz, 1H), 8.80 (dd, J = 1.7, 8.0 Hz, 1H), 7.69 (m, J = 3.2 Hz, 2H), 4.43 (q, J = 7.1 Hz, 2H), 1.42 (t, J = 7.1 Hz, 3H).

Phenanthrolinopyrrole (1):[143]

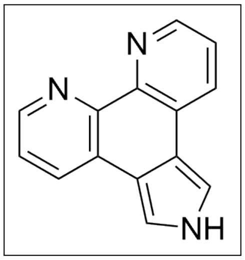

Ethylene glycol (20 mL) was first degassed with N_2, then **1-e** (300 mg, 1.03 mmol) and KOH (600 mg, 10.7 mmol) were added. The mixture was refluxed under N_2 for 30 min, after which the solution was poured into ice water. The resulting precipitate was collected via vacuum filtration, washed with water and dried in air (190 mg, 84%). ^{1}H NMR (500 MHz, DMSO-d_6) δ 8.76 (dd, J = 4.4, 1.7 Hz, 2H), 8.56 (dd, J = 8.0, 1.8 Hz, 2H), 7.93 (d, J = 2.8 Hz, 2H), 7.57 (dd, J = 8.0, 4.4 Hz, 2H).

Nitroalkene (2):[166]

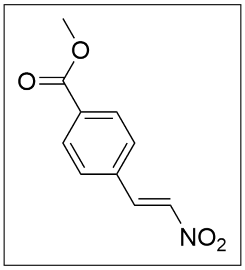

Methyl p-formylbenzoate (368 mg, 2 mmol) and nitromethane (130 µL, 2.4 mmol) were dissolved in MeOH (ca. 10 mL) and cooled to 0 °C. With stirring, NaOH was added (100 mg, 2.5 mmol in 1 mL H_2O) dropwise over 30 min. After complete addition, the solution was stirred for another 30 min, after which it was neutralized with HCl (1 M). A pale-yellow precipitate was collected via vacuum filtration, washed with cold MeOH and dried in air (310 mg, 75%). ^{1}H NMR (300 MHz, $CDCl_3$) δ 8.11 (d, J = 8.3 Hz, 2H), 8.02 (d, J = 13.7 Hz, 1H), 7.68 – 7.57 (m, 3H), 3.95 (s, 3H).

Pyrrole (3'-e):

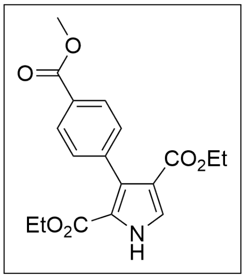

To 5 mL of EtOH, **2** (207 mg, 1 eq.) and EtICA (110 µL, 1 eq.) were added. With stirring, K_2CO_3 (415 mg, 3 eq.) was added and the mixture was stirred overnight at room temperature. Then, the mixture was diluted with water and extracted with EtOAc. The organic extract was washed with water (3×10 mL), brine (1×10 mL), and dried over $MgSO_4$ before being evaporated in vacuo. The crude residue was then chromatographed on silica with EtOAc/hexanes (15:85) as eluent to afford a yellow oil. ^{1}H NMR (300 MHz, $CDCl_3$) δ 9.54 (bs, 1H), 8.03 (d, J = 8.6 Hz, 1H), 7.61 (d, J = 3.4 Hz, 1H), 7.40 (d, J = 8.6 Hz, 1H), 4.12 (q, J = 7.1 Hz, 2H), 4.11 (q, J = 7.1 Hz, 2H), 3.93 (s, 3H), 1.10 (t, J = 7.1 Hz, 3H), 1.04 (t, J = 7.2 Hz, 3H).

Nitroalkene (4):

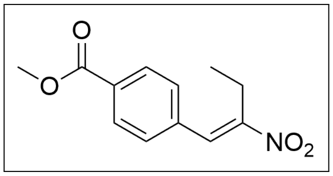

Methyl *p*-formylbenzoate (164 mg, 1.00 mmol) and ammonium acetate (123 mg, 1.60 mmol) were dissolved in acetic acid (5 mL). To this, 1-nitropropane (98 µL, 1.10 mmol) was added. The colourless solution was stirred at reflux overnight. The resulting yellow, clear solution was poured into a beaker of cold water, neutralized with sat. $NaHCO_3$ (aq.). After neutralization, the solution becomes colourless, and a pale yellow solid coated the beaker. The solid was dissolved in EtOAc (20 mL), washed with water (3×10 mL) and brine (1×10 mL). The solvent was evaporated and the crude residue was recrystallized in 95% EtOH to give yellow needle-like crystals of **4** (184 mg, 78%). ^{1}H NMR (500 MHz, $CDCl_3$) δ 8.11 (d, J = 8.4 Hz, 2H), 8.01 (s, 1H), 7.47 (d, J = 8.2 Hz, 2H), 3.95 (s, 3H), 2.85 (q, J = 7.4 Hz, 2H), 1.28 (t, J = 7.4 Hz, 3H).

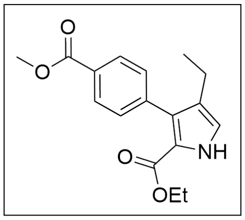

Ethyl pyrrole-2-carboxylate (5-e):

Nitroalkene **4** (235 mg, 1.00 mmol) was suspended in isopropanol (ca. 10 mL). To the suspension, EtICA (113 µL, 1.04 mmol) was added with stirring. To the dark brown suspension, DBU (150 µL, 1.00 mmol) was added. Upon addition of base, all remaining solids were dissolved. The solution was left to stir overnight at room temperature. The dark solution was then poured into dilute HCl (1 M, ca. 20 mL) and extracted with EtOAc. The extracts were washed with water and brine, then dried over $MgSO_4$. The solvent was evaporated, and the dark brown residue was triturated with hexanes. The solution in hexanes was filtered through a short plug of celite, then evaporated to obtain **5-e** as a pale-orange oil (193 mg, 64%). ^{1}H NMR (300 MHz, $CDCl_3$) δ 9.03 (s, 1H), 8.04 (d, J = 8.5 Hz, 2H), 7.40 (d, J = 8.6 Hz, 2H), 6.81 (d, J = 3.0 Hz, 1H), 4.14 (q, J = 7.1 Hz, 2H), 2.39 (q, J = 7.5 Hz, 2H), 1.11 (t, J = 7.2 Hz, 3H), 1.06 (t, J = 7.5 Hz, 3H).

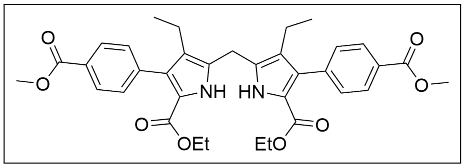

Dipyrromethane (7-e):

To a solution of **5-e** (660 mg, 2.19 mmol) in $CHCl_3$, dimethoxymethane (485 µL) and p-TsOH (38 mg) were added. The mixture was stirred under nitrogen at room temperature for 4 d. The reaction mixture was then washed with $NaHCO_3$ (aq.), H_2O, and brine, then dried over Na_2SO_4. The solvent was evaporated and the residue was purified by chromatography, first eluting with CH_2Cl_2 to remove impurities, then 1-2% MeOH was added to elute the desired compound. The solvent was evaporated and dipyrromethane **7-e** was obtained as a yellow-orange oil (228 mg, 34%). ^{1}H NMR (500 MHz, $CDCl_3$) δ 8.96 (s, 2H), 8.06 (d, J = 8.3 Hz, 4H), 7.40 (d, J = 8.3 Hz, 4H), 4.10 (q, J = 7.1 Hz, 4H), 4.02 (s, 2H), 3.94 (s, 6H), 2.39 (q, J = 7.5 Hz, 4H), 1.05 (t, J = 7.1 Hz, 6H), 0.92 (t, J = 7.5 Hz, 6H).

Chapter 4

Future Directions

This thesis explored two distinct sides of MOFs and their chemistry. On the one end, evaluating the gas adsorption of two frameworks with incredibly small pores, so small that they can act as molecular sieves for gases based on their size alone. On the other end, starting to develop a route to new porphyrin linkers, which would result in much larger frameworks. The theme tying these projects together is the development of systems that can be modified and tailored to specific applications.

4.1 Gas Separation and Tuneable Frameworks

In Chapter 2, an emerging family of MOFs was presented whose pores can be tuned at the sub-Å scale. This sort of tuneability opens up the path for developing efficient molecular sieves for gas separations, and the stark differences in gas adsorption between $\mathbf{Zn_3}$ and $\mathbf{Zn_2Cd}$ highlight this. Perhaps one of the reasons that molecular sieving MOFs such as $\mathbf{Zn_3}$ may not have been previously investigated in detail is due to the commonly targeted MOF applications, pressure-swing and temperature-swing adsorption, often requiring decent adsorption capacities (e.g., 3–4 $\mathrm{mmol_{CO_2}\,g^{-1}}$ of sorbent for adsorption-based CO_2 capture[167]), which are out of reach for a material like **$\mathbf{Zn_3}$** (ca. 0.4 $\mathrm{mmol_{CO_2}\,g^{-1}}$ at 295 K and 1 atm). However, a low adsorption capacity does not preclude **$\mathbf{Zn_3}$** from being used in separations. In fact, the lower capacity coupled with ability to exclude Ar and larger gases could be ideal for membrane based filters as described earlier in this thesis. Crucially in membrane-based separations, it is gas permeance (i.e., the permeability of the membrane divided by the membrane thickness) that dictates the applicability of a particular material and not the working capacity. This also means that a **$\mathbf{Zn_3}$**-based mixed-matrix membrane (**$\mathbf{Zn_3}$**-MMM) would be effective at higher operating temperatures, where the gas uptake is lower and the diffusion kinetics are higher. I believe that an ideal application for a **$\mathbf{Zn_3}$**-MMM would be direct air capture (DAC) of CO_2 from the atmosphere. The challenge with DAC is the significantly lower concentration of CO_2 in air (ca. 0.04 vol%) compared to flue gas streams (10–15 vol%). All but the most highly selective sorbents would struggle to capture a meaningful amount, as most adsorptive sites would be occupied by other gas molecules. Those sorbents that could bind CO_2 selectively at such low concentrations have the drawback that the energy cost to recycle/regenerate the material would be very high. A **$\mathbf{Zn_3}$**-MMM does not function on adsorption, and the exclusion of other gases larger than CO_2 means that the dilute concentration is less of an issue. A conceptual mock-up of such a DAC membrane cell is shown in Figure 4.1. Applying a pressure differential across the membrane would drive CO_2 diffusion, and the permeate stream could then be routed to a compressor, or a high capacity adsorbent (e.g., another MOF), to concentrate/store the captured CO_2.

A **$\mathbf{Zn_2Cd}$**-MMM, on the other hand, with its larger pore apertures could potentially be used in the molecular sieving of hydrocarbons such as propane/propylene mixtures. To date, research on MMMs for propane/propylene separation has been

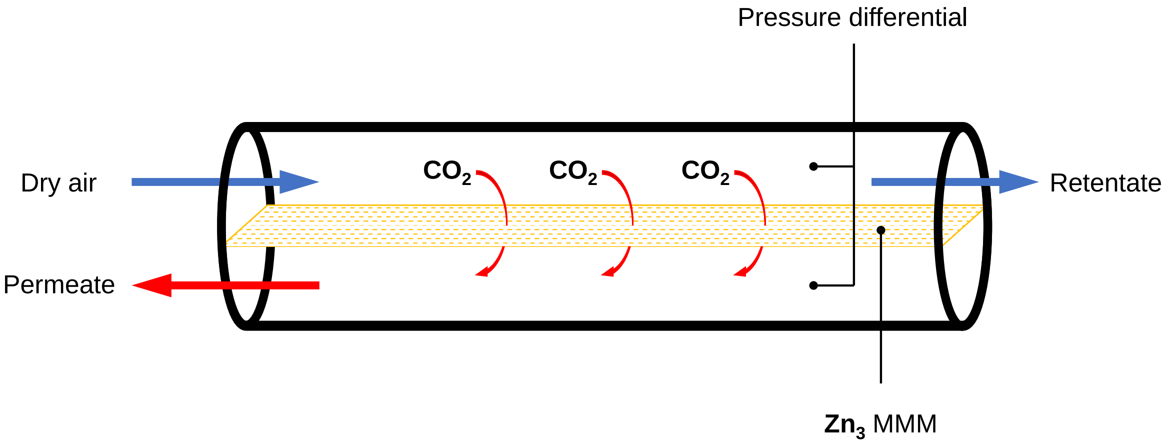

Figure 4.1: Membrane cell concept for direct air capture of CO_2.

dominated by the ZIF family of adsorbents, underlining the need for broader work in this area.[168]

4.2 Porphyrin Linkers and Por-MOFs

Developing new porphyrin MOF linkers was an ambitious undertaking. Although time was limited due to the pandemic, the work presented in Chapter 3 will serve as a jumping-off point for future students to explore this chemistry. The ultimate goal of designing these new porphyrin linkers is to give MOF chemists a way to modify the regions nearest the porphyrin active site (i.e., the *meso*-positions), and thus tune properties such as gas adsorption and catalysis. In contrast, current Por-MOF linkers such as TCPP offer limited ways of tuning the porphyrin core itself. The results herein have shown that the intended chemistry is possible, with some of the desired porphyrin configurations being detectable by NMR. Improved synthetic technique will undoubtedly give access to these linkers, and by extension new Por-MOFs. A particularly exciting extension of this work is the development of enzyme-inspired linkers. One of the common motifs in porphyrin-containing heme enzymes is the coordination

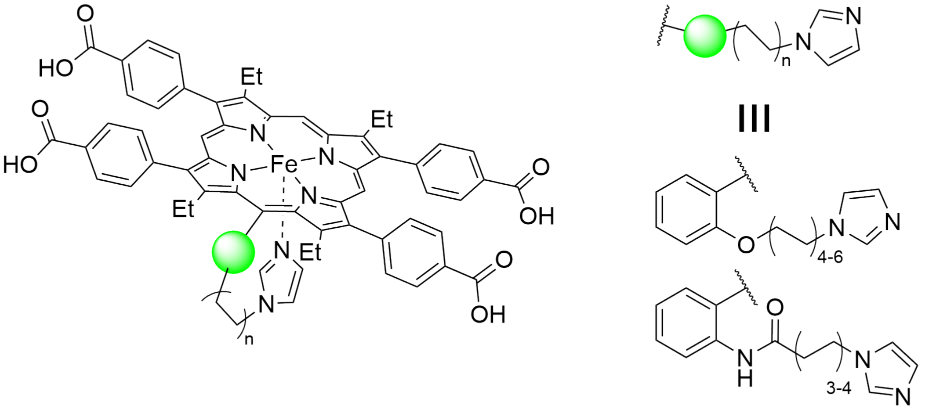

Figure 4.2: Type-II metalloporphyrin linker with a *meso*-tethered imidazole, which can form a heme-like active site.

of an axial ligand to the Fe metal center. This ligand comes from a nearby amino-acid residue, such as histidine (imidazole), tyrosine (phenolate), or cysteine (thiolate).[169] A common way to mimic this these biological systems is to covalently tether the axial ligand to the porphyrin.[170–172] In the porphyrin linkers discussed in Chapter 3, the free *meso*-positions provide the ideal location for such tethering. Figure 4.2 shows a porphyrin linker that has a histidine-like moiety hanging from the *meso*-position. This moiety could then axially coordinate an Fe porphyrin, creating an active site that closely resembles that of a heme protein. When incorporated into a MOF, this sort of linker enables a well defined active site dispersed within the framework, and brings us closer to bio-inspired catalysis. The scope of these new Por-MOFs is not limited to mimicry of enzymes, and inspiration can also be drawn from porphyrin systems previously only seen in molecular catalysis. For example, the central metal of a metalloporphyrin linker can function as a binding site for gases. The binding of gas at this site can be tuned through functionalities at the *meso*-positions, such as electron donating groups for NO_2 adsorption,[173] or Lewis-basic groups for increased CO_2 binding.[174] Overall, there are some exciting future applications of Por-MOFs enabled by β-substituted linkers, particularly in catalysis and gas sensing applications.

References

(1) R. M. Barrer, *Journal of the Chemical Society (Resumed)*, 1948, 2158–2163.

(2) B. McEnaney, *Carbon*, 1988, **26**, 267–274.

(3) N. Giri, M. G. Del Pópolo, G. Melaugh, R. L. Greenaway, K. Rätzke, T. Koschine, L. Pison, M. F. C. Gomes, A. I. Cooper and S. L. James, *Nature*, 2015, **527**, 216–220.

(4) P. M. Budd, B. S. Ghanem, S. Makhseed, N. B. McKeown, K. J. Msayib and C. E. Tattershall, *Chemical Communications*, 2004, 230–231.

(5) S. Kitagawa, R. Kitaura and S.-I. Noro, *Angewandte Chemie International Edition*, 2004, **43**, 2334–2375.

(6) M. Kondo, T. Yoshitomi, H. Matsuzaka, S. Kitagawa and K. Seki, *Angewandte Chemie International Edition*, 1997, **36**, 1725–1727.

(7) A. P. Côté, A. I. Benin, N. W. Ockwig, M. O'Keeffe, A. J. Matzger and O. M. Yaghi, *Science*, 2005, **310**, 1166–1170.

(8) T. Tozawa, J. T. A. Jones, S. I. Swamy, S. Jiang, D. J. Adams, S. Shakespeare, R. Clowes, D. Bradshaw, T. Hasell, S. Y. Chong, C. Tang, S. Thompson, J. Parker, A. Trewin, J. Bacsa, A. M. Z. Slawin, A. Steiner and A. I. Cooper, *Nature Materials*, 2009, **8**, 973–978.

(9) A. Carné-Sánchez, G. A. Craig, P. Larpent, T. Hirose, M. Higuchi, S. Kitagawa, K. Matsuda, K. Urayama and S. Furukawa, *Nature Communications*, 2018, **9**, 2506.

(10) Y. Li and R. T. Yang, *Langmuir*, 2007, **23**, 12937–12944.

(11) H. Li, L. Li, R.-B. Lin, W. Zhou, Z. Zhang, S. Xiang and B. Chen, *EnergyChem*, 2019, **1**, 100006.

(12) R. L. Siegelman, E. J. Kim and J. R. Long, *Nature Materials*, 2021, **20**, 1060–1072.

(13) A. Chakraborty, S. Roy, M. Eswaramoorthy and T. K. Maji, *Journal of Materials Chemistry A*, 2017, **5**, 8423–8430.

(14) A. A. Alqadami, M. Naushad, Z. A. Alothman and A. A. Ghfar, *ACS Applied Materials & Interfaces*, 2017, **9**, 36026–36037.

(15) J. Liu, Y.-Z. Fan, X. Li, Z. Wei, Y.-W. Xu, L. Zhang and C.-Y. Su, *Applied Catalysis B: Environmental*, 2018, **231**, 173–181.

(16) A. Salerno, L. Verdolotti, M. G. Raucci, J. Saurina, C. Domingo, R. Lamanna, V. Iozzino and M. Lavorgna, *European Polymer Journal*, 2018, **99**, 230–239.

(17) E. J. Anglin, L. Cheng, W. R. Freeman and M. J. Sailor, *Advanced Drug Delivery Reviews*, 2008, **60**, 1266–1277.

(18) V. A. Moshnikov, I. E. Gracheva, V. V. Kuznezov, A. I. Maximov, S. S. Karpova and A. A. Ponomareva, *Journal of Non-Crystalline Solids*, 2010, **356**, 2020–2025.

(19) C. Gomes Silva, A. Corma and H. García, *Journal of Materials Chemistry*, 2010, **20**, 3141–3156.

(20) H. A. Patel, N. Mansor, S. Gadipelli, D. J. L. Brett and Z. Guo, *ACS Applied Materials & Interfaces*, 2016, **8**, 30687–30691.

(21) Y. A. Mezenov, N. K. Kulachenkov, A. N. Yankin, S. S. Rzhevskiy, P. V. Alekseevskiy, V. D. Gilemkhanova, S. V. Bachinin, V. Dyachuk and V. A. Milichko, *Nanomaterials*, 2020, **10**, 1036.

(22) B. F. Hoskins and R. Robson, *Journal of the American Chemical Society*, 1990, **112**, 1546–1554.

(23) H. Li, M. Eddaoudi, M. O'Keeffe and O. M. Yaghi, *Nature*, 1999, **402**, 276–279.

(24) V. Guillerm and D. Maspoch, *Journal of the American Chemical Society*, 2019, **141**, 16517–16538.

(25) H. Ghasempour, K.-Y. Wang, J. A. Powell, F. ZareKarizi, X.-L. Lv, A. Morsali and H.-C. Zhou, *Coordination Chemistry Reviews*, 2021, **426**, 213542.

(26) P. Tholen, Y. Zorlu, J. Beckmann and G. Yücesan, *European Journal of Inorganic Chemistry*, 2020, 1542–1554.

(27) G. Zhang, G. Wei, Z. Liu, S. R. J. Oliver and H. Fei, *Chemistry of Materials*, 2016, **28**, 6276–6281.

(28) Y. Kamakura, S. Fujisawa, K. Takahashi, H. Toshima, Y. Nakatani, H. Yoshikawa, A. Saeki, K. Ogasawara and D. Tanaka, *Inorganic Chemistry*, 2021, **60**, 12691–12695.

(29) N. Stock and S. Biswas, *Chemical Reviews*, 2012, **112**, 933–969.

(30) X. Wu, Z. Bao, B. Yuan, J. Wang, Y. Sun, H. Luo and S. Deng, *Microporous and Mesoporous Materials*, 2013, **180**, 114–122.

(31) T. Wiwasuku, J. Othong, J. Boonmak, V. Ervithayasuporn and S. Youngme, *Dalton Transactions*, 2020, **49**, 10240–10249.

(32) O. J. d. L. Neto, A. C. d. O. Frós, B. S. Barros, A. F. d. F. Monteiro and J. Kulesza, *New Journal of Chemistry*, 2019, **43**, 5518–5524.

(33) M. Klimakow, P. Klobes, A. F. Thünemann, K. Rademann and F. Emmerling, *Chemistry of Materials*, 2010, **22**, 5216–5221.

(34) J. Rouquerol, F. Rouquerol, P. Llewellyn, G. Maurin and K. S. Sing, *Adsorption by Powders and Porous Solids: Principles, Methodology and Applications: Second Edition*, Elsevier, 2013, 1–626.

(35) D. T. McGrath, M. D. Ryan, J. J. Macinnis, T. C. Vandenboer, C. J. Young and M. J. Katz, *Chemical Science*, 2019, **10**, 5576–5581.

(36) J. D. Martell, P. J. Milner, R. L. Siegelman and J. R. Long, *Chemical Science*, 2020, **11**, 6457–6471.

(37) P. M. Bhatt, Y. Belmabkhout, A. Cadiau, K. Adil, O. Shekhah, A. Shkurenko, L. J. Barbour and M. Eddaoudi, *Journal of the American Chemical Society*, 2016, **138**, 9301–9307.

(38) H. Hu, J. Zhu, F. Yang, Z. Chen, M. Deng, L. Weng, Y. Ling and Y. Zhou, *Chemical Communications*, 2019, **55**, 6495–6498.

(39) A. F. Kloutse, R. Zacharia, D. Cossement, R. Chahine, R. Balderas-Xicohténcatl, H. Oh, B. Streppel, M. Schlichtenmayer and M. Hirscher, *Applied Physics A*, 2015, **121**, 1417–1424.

(40) D. Wu, J. J. Gassensmith, D. Gouvêa, S. Ushakov, J. F. Stoddart and A. Navrotsky, *Journal of the American Chemical Society*, 2013, **135**, 6790–6793.

(41) L. Hao, S. A. Stoian, L. R. Weddle and Q. Zhang, *Green Chemistry*, 2020, **22**, 6351–6356.

(42) D. S. Sholl and R. P. Lively, *Nature*, 2016, **532**, 435–437.

(43) Z. Kang, L. Fan and D. Sun, *Journal of Materials Chemistry A*, 2017, **5**, 10073–10091.

(44) C. Graham, J. Pierrus and R. Raab, *Molecular Physics*, 1989, **67**, 939–955.

(45) J.-R. Li, J. Yu, W. Lu, L.-B. Sun, J. Sculley, P. B. Balbuena and H.-C. Zhou, *Nature Communications*, 2013, **4**, 1538.

(46) X. Si, C. Jiao, F. Li, J. Zhang, S. Wang, S. Liu, Z. Li, L. Sun, F. Xu, Z. Gabelica and C. Schick, *Energy & Environmental Science*, 2011, **4**, 4522–4527.

(47) L. Li, R.-B. Lin, X. Wang, W. Zhou, L. Jia, J. Li and B. Chen, *Chemical Engineering Journal*, 2018, **354**, 977–982.

(48) A. L. Myers and J. M. Prausnitz, *AIChE Journal*, 1965, **11**, 121–127.

(49) S. Lee, J. H. Lee and J. Kim, *Korean Journal of Chemical Engineering*, 2018, **35**, 214–221.

(50) C. M. Simon, B. Smit and M. Haranczyk, *Computer Physics Communications*, 2016, **200**, 364–380.

(51) E. Haldoupis, S. Nair and D. S. Sholl, *Journal of the American Chemical Society*, 2010, **132**, 7528–7539.

(52) Y. Wang and D. Zhao, *Crystal Growth & Design*, 2017, **17**, 2291–2308.

(53) D. W. Breck, *Zeolite Molecular Sieves : Structure, Chemistry, and Use*, Wiley, New York, 1973.

(54) X. Wang, S. Ramírez-Hinestrosa, J. Dobnikar and D. Frenkel, *Physical Chemistry Chemical Physics*, 2020, **22**, 10624–10633.

(55) M. M. Dal-Cin, A. Kumar and L. Layton, *Journal of Membrane Science*, 2008, **323**, 299–308.

(56) N. Mehio, S. Dai and D.-E. Jiang, *The Journal of Physical Chemistry A*, 2014, **118**, 1150–1154.

(57) S. Subramanian and M. J. Zaworotko, *Angewandte Chemie International Edition*, 1995, **34**, 2127–2129.

(58) K. Uemura, A. Maeda, T. K. Maji, P. Kanoo and H. Kita, *European Journal of Inorganic Chemistry*, 2009, 2329–2337.

(59) S. K. Elsaidi, M. H. Mohamed, H. T. Schaef, A. Kumar, M. Lusi, T. Pham, K. A. Forrest, B. Space, W. Xu, G. J. Halder, J. Liu, M. J. Zaworotko and P. K. Thallapally, *Chemical Communications*, 2015, **51**, 15530–15533.

(60) O. Shekhah, Y. Belmabkhout, Z. Chen, V. Guillerm, A. Cairns, K. Adil and M. Eddaoudi, *Nature Communications*, 2014, **5**, 4228.

(61) M. H. Mohamed, S. K. Elsaidi, L. Wojtas, T. Pham, K. A. Forrest, B. Tudor, B. Space and M. J. Zaworotko, *Journal of the American Chemical Society*, 2012, **134**, 19556–19559.

(62) M. H. Mohamed, S. K. Elsaidi, T. Pham, K. A. Forrest, B. Tudor, L. Wojtas, B. Space and M. J. Zaworotko, *Chemical Communications*, 2013, **49**, 9809–9811.

(63) L. Feng, K.-Y. Wang, E. Joseph and H.-C. Zhou, *Trends in Chemistry*, 2020, **2**, 555–568.

(64) T. Burger, C. Winkler, I. Dalfen, C. Slugovc and S. M. Borisov, *Journal of Materials Chemistry C*, 2021, **9**, 17099–17112.

(65) X. Sun, G. He, C. Xiong, C. Wang, X. Lian, L. Hu, Z. Li, S. J. Dalgarno, Y.-W. Yang and J. Tian, *ACS Applied Materials & Interfaces*, 2021, **13**, 3679–3693.

(66) R. Willstätter and A. Stoll, *Untersuchungen Über Chlorophyll. Methoden und Ergebnisse*, Springer, Berlin, Germany, 1913.

(67) B. F. Abrahams, B. F. Hoskins and R. Robson, *Journal of the American Chemical Society*, 1991, **113**, 3606–3607.

(68) B. F. Abrahams, B. F. Hoskins, D. M. Michail and R. Robson, *Nature*, 1994, **369**, 727–729.

(69) D. Feng, Z.-Y. Gu, J.-R. Li, H.-L. Jiang, Z. Wei and H.-C. Zhou, *Angewandte Chemie International Edition*, 2012, **51**, 10307–10310.

(70) W. Morris, B. Volosskiy, S. Demir, F. Gándara, P. L. McGrier, H. Furukawa, D. Cascio, J. F. Stoddart and O. M. Yaghi, *Inorganic Chemistry*, 2012, **51**, 6443–6445.

(71) P. Deria, D. A. Gómez-Gualdrón, I. Hod, R. Q. Snurr, J. T. Hupp and O. K. Farha, *Journal of the American Chemical Society*, 2016, **138**, 14449–14457.

(72) K. Wang, D. Feng, T.-F. Liu, J. Su, S. Yuan, Y.-P. Chen, M. Bosch, X. Zou and H.-C. Zhou, *Journal of the American Chemical Society*, 2014, **136**, 13983–13986.

(73) M. V. Nguyen, H. C. Dong, V. T. N. Truong, H. N. Nguyen, L. C. Luu, N. D. Nam and T. A. T. Nguyen, *New Journal of Chemistry*, 2021, **46**, 632–641.

(74) O. K. Farha, A. M. Shultz, A. A. Sarjeant, S. T. Nguyen and J. T. Hupp, *Journal of the American Chemical Society*, 2011, **133**, 5652–5655.

(75) Y. Zhao, S. Qi, Z. Niu, Y. Peng, C. Shan, G. Verma, L. Wojtas, Z. Zhang, B. Zhang, Y. Feng, Y.-S. Chen and S. Ma, *Journal of the American Chemical Society*, 2019, **141**, 14443–14450.

(76) Y. Yang, R. Sakashita, K. Yamasumi, M. Ishida, T. Yamada and H. Furuta, *Chemistry Letters*, 2017, **46**, 1230–1232.

(77) V. B. Urlacher and M. Girhard, *Trends in Biotechnology*, 2019, **37**, 882–897.

(78) J. G. J. Olivier and J. A. H. W. Peters, *Trends in Global* CO_2 *and Total Greenhouse Gas Emissions: 2020 Report*, 4331, PBL Netherlands Environmental Assessment Agency, The Hague, 2020.

(79) R. Akhtar, in *Extreme Weather Events and Human Health: International Case Studies*, ed. R. Akhtar, Springer International Publishing, Cham, 2020, pp. 3–11.

(80) D. Aaron and C. Tsouris, *Separation Science and Technology*, 2005, **40**, 321–348.

(81) P. Hovington, O. Ghaffari-Nik, L. Mariac, A. Liu, B. Henkel and S. Marx, *Rapid Cycle Temperature Swing Adsorption Process Using Solid Structured Sorbent for* CO_2 *Capture from Cement Flue Gas*, SSRN Scholarly Paper ID 3814414, Social Science Research Network, Rochester, NY, 2021.

(82) V. A. Downing, M.Sc. Thesis, Memorial University of Newfoundland, 2021.

(83) L. Sarkisov and A. Harrison, *Molecular Simulation*, 2011, **37**, 1248–1257.

(84) K. Momma and F. Izumi, *Journal of Applied Crystallography*, 2011, **44**, 1272–1276.

(85) A. L. Spek, *Acta Crystallographica*, 2015, **C71**, 9–18.

(86) J. H. Cavka, S. Jakobsen, U. Olsbye, N. Guillou, C. Lamberti, S. Bordiga and K. P. Lillerud, *Journal of the American Chemical Society*, 2008, **130**, 13850–13851.

(87) H. Wu, Y. S. Chua, V. Krungleviciute, M. Tyagi, P. Chen, T. Yildirim and W. Zhou, *Journal of the American Chemical Society*, 2013, **135**, 10525–10532.

(88) M. J. Katz, Z. J. Brown, Y. J. Colón, P. W. Siu, K. A. Scheidt, R. Q. Snurr, J. T. Hupp and O. K. Farha, *Chemical Communications*, 2013, **49**, 9449–9451.

(89) H. Marsh and W. F. K. Wynne-Jones, *Carbon*, 1964, **1**, 269–279.

(90) H. Marsh, *Carbon*, 1987, **25**, 49–58.

(91) S. P. Nandi and P. L. Walker, *Fuel*, 1970, **49**, 309–323.

(92) M. B. Rao, *Carbon*, 1991, **29**, 813–815.

(93) J.-R. Li, R. J. Kuppler and H.-C. Zhou, *Chemical Society Reviews*, 2009, **38**, 1477–1504.

(94) J. A. Mason, K. Sumida, Z. R. Herm, R. Krishna and J. R. Long, *Energy & Environmental Science*, 2011, **4**, 3030–3040.

(95) S. Nandi, R. Maity, D. Chakraborty, H. Ballav and R. Vaidhyanathan, *Inorganic Chemistry*, 2018, **57**, 5267–5272.

(96) R. Luebke, J. F. Eubank, A. J. Cairns, Y. Belmabkhout, L. Wojtas and M. Eddaoudi, *Chemical Communications*, 2012, **48**, 1455–1457.

(97) A. Pal, S. Chand and M. C. Das, *Inorganic Chemistry*, 2017, **56**, 13991–13997.

(98) R. Vaidhyanathan, S. S. Iremonger, G. K. H. Shimizu, P. G. Boyd, S. Alavi and T. K. Woo, *Angewandte Chemie International Edition*, 2012, **51**, 1826–1829.

(99) D. Broom, *Chemical Engineering World*, 2016, **51**, 35–37.

(100) M. Kalaj, K. C. Bentz, S. Ayala, J. M. Palomba, K. S. Barcus, Y. Katayama and S. M. Cohen, *Chemical Reviews*, 2020, **120**, 8267–8302.

(101) J. Zhu, H. Li, J. Hou, J. Liu, Y. Zhang and B. Van der Bruggen, *AIChE Journal*, 2020, **66**, e16935.

(102) Z. Zhang, H. T. H. Nguyen, S. A. Miller, A. M. Ploskonka, J. B. Decoste and S. M. Cohen, *Journal of the American Chemical Society*, 2016, **138**, 920–925.

(103) J.-O. Kim, J. Y. Kim, J.-C. Lee, S. Park, H. R. Moon and D.-P. Kim, *ACS Applied Materials & Interfaces*, 2019, **11**, 4385–4392.

(104) *STEPOSOL® MET-10U*, `https://www.stepan.com/content/stepan-dot-com/en/products-markets/product/STEPOSOLMET10U.html` (visited on 03/17/2022).

(105) P. Marino, P. R. Donnarumma, H. A. Bicalho, V. Quezada-Novoa, H. M. Titi and A. J. Howarth, *ACS Sustainable Chemistry & Engineering*, 2021, **9**, 16356–16362.

(106) B. Felber, C. Calle, P. Seiler, A. Schweiger and F. Diederich, *Organic & Biomolecular Chemistry*, 2003, **1**, 1090–1093.

(107) L. J. Twyman and Y. Ge, *Chemical Communications*, 2006, 1658–1660.

(108) I. Hod, M. D. Sampson, P. Deria, C. P. Kubiak, O. K. Farha and J. T. Hupp, *ACS Catalysis*, 2015, **5**, 6302–6309.

(109) A. Berlin, B. Vercelli and G. Zotti, *Polymer Reviews*, 2008, **48**, 493–530.

(110) S. S. Gholap, *European Journal of Medicinal Chemistry*, 2016, **110**, 13–31.

(111) A. Loudet and K. Burgess, *Chemical Reviews*, 2007, **107**, 4891–4932.

(112) Y. Higashio and T. Shoji, *Applied Catalysis A: General*, 2004, **260**, 251–259.

(113) A. M. van Leusen, F. J. Schaart and D. van Leusen, *Recueil des Travaux Chimiques des Pays-Bas*, 1979, **98**, 258–262.

(114) D. Van Leusen, E. Van Echten and A. M. Van Leusen, *The Journal of Organic Chemistry*, 1992, **57**, 2245–2249.

(115) D. van Leusen and A. M. van Leusen, *The Journal of Organic Chemistry*, 1994, **59**, 7534–7538.

(116) D. V. Leusen and A. M. V. Leusen, in *Organic Reactions*, John Wiley & Sons, Ltd, 2004, pp. 417–666.

(117) R. ten Have and A. M. van Leusen, *Tetrahedron*, 1998, **54**, 1913–1920.

(118) A. M. van Leusen, H. Siderius, B. E. Hoogenboom and D. van Leusen, *Tetrahedron Letters*, 1972, **13**, 5337–5340.

(119) T. Balasubramanian and J. S. Lindsey, *Tetrahedron*, 1999, **55**, 6771–6784.

(120) P. Carter, S. Fitzjohn, S. Halazy and P. Magnus, *Journal of the American Chemical Society*, 1987, **109**, 2711–2717.

(121) D. H. R. Barton and S. Z. Zard, *Journal of the Chemical Society, Chemical Communications*, 1985, 1098–1100.

(122) N. Ono, T. Yamamoto, N. Shimada, K. Kuroki, M. Wada, R. Utsunomiya, T. Yano, H. Uno and T. Murashima, *HETEROCYCLES*, 2003, **61**, 433.

(123) P. B. Shea, L. R. Pattison, M. Kawano, C. Chen, J. Chen, P. Petroff, D. C. Martin, H. Yamada, N. Ono and J. Kanicki, *Synthetic Metals*, 2007, **157**, 190–197.

(124) I. Satyanarayana, D.-Y. Yang and T.-J. Liou, *RSC Advances*, 2020, **10**, 43168–43174.

(125) J.-Y. Zeng, X.-S. Wang, B.-R. Xie, Q.-R. Li and X.-Z. Zhang, *Journal of the American Chemical Society*, 2022, **144**, 1218–1231.

(126) J.-Y. Zeng, M.-Z. Zou, M. Zhang, X.-S. Wang, X. Zeng, H. Cong and X.-Z. Zhang, *ACS Nano*, 2018, **12**, 4630–4640.

(127) J. S. Lindsey, H. C. Hsu and I. C. Schreiman, *Tetrahedron Letters*, 1986, **27**, 4969–4970.

(128) N. Ono and K. Maruyama, *Chemistry Letters*, 1988, **17**, 1511–1514.

(129) N. Ono, H. Kawamura, M. Bougauchi and K. Maruyama, *Journal of the Chemical Society, Chemical Communications*, 1989, 1580.

(130) N. Ono, H. Kawamura and K. Maruyama, *Bulletin of the Chemical Society of Japan*, 1989, **62**, 3386–3388.

(131) N. Ono, E. Muratani, Y. Fumoto and K. Tazima, *Journal of the Chemical Society, Perkin Transactions*, 1998, **1**, 3819–3824.

(132) G. P. Arsenault, E. Bullock and S. F. MacDonald, *Journal of the American Chemical Society*, 1960, **82**, 4384–4389.

(133) S. Fox, R. Hudson and R. W. Boyle, *Tetrahedron Letters*, 2003, **44**, 1183–1185.

(134) B. F. Hohlfeld, K. J. Flanagan, N. Kulak, M. O. Senge, M. Christmann and A. Wiehe, *European Journal of Organic Chemistry*, 2019, 4020–4033.

(135) J. S. Lindsey, *Accounts of Chemical Research*, 2010, **43**, 300–311.

(136) E. A. Mikhalitsyna, V. S. Tyurin, S. E. Nefedov, S. A. Syrbu, A. S. Semeikin, O. I. Koifman and I. P. Beletskaya, *European Journal of Inorganic Chemistry*, 2012, 5979–5990.

(137) P. Thamyongkit, M. Speckbacher, J. R. Diers, H. L. Kee, C. Kirmaier, D. Holten, D. F. Bocian and J. S. Lindsey, *The Journal of Organic Chemistry*, 2004, **69**, 3700–3710.

(138) M. Shayan, Ph.D. Thesis, Memorial University of Newfoundland, 2021.

(139) T. D. Lash, B. H. Novak and Y. Lin, *Tetrahedron Letters*, 1994, **35**, 2493–2494.

(140) A. Bhattacharya, S. Cherukuri, R. E. Plata, N. Patel, V. Tamez, J. A. Grosso, M. Peddicord and V. A. Palaniswamy, *Tetrahedron Letters*, 2006, **47**, 5481–5484.

(141) E. A. Silyanova, A. V. Samet and V. V. Semenov, *Russian Chemical Bulletin*, 2018, **67**, 2316–2319.

(142) A. V. Samet, E. A. Silyanova, V. I. Ushkarov, M. N. Semenova and V. V. Semenov, *Russian Chemical Bulletin*, 2018, **67**, 858–865.

(143) T. D. Lash, Y. Lin, B. H. Novak and M. D. Parikh, *Tetrahedron*, 2005, **61**, 11601–11614.

(144) S. Swavey, M. DeBeer and K. Li, *Inorganic Chemistry*, 2015, **54**, 3139–3147.

(145) R. Plamont, Y. Kikkawa, M. Takahashi, M. Kanesato, M. Giorgi, A. Chan Kam Shun, C. Roussel and T. S. Balaban, *Chemistry - A European Journal*, 2013, **19**, 11293–11300.

(146) T. Shinoda, M. Onaka and Y. Izumi, *Chemistry Letters*, 1995, **24**, 495–496.

(147) T. Shinoda, M. Onaka and Y. Izumi, *Chemistry Letters*, 1995, **24**, 493–494.

(148) K. Saitoh, C. Kiyohara and N. Suzuki, *Journal of Chromatography A*, 1992, **603**, 231–234.

(149) B. J. Sjursnes, L. Kvittingen and R. Schmid, *Journal of Planar Chromatography - Modern TLC*, 2016, **29**, 480–483.

(150) M. Momenteau, P. Maillard, M.-A. De Bélinay, D. Carrez and A. Croisy, *Journal of Biomedical Optics*, 1999, **4**, 298–318.

(151) S. Nakajima and A. Osuka, *Tetrahedron Letters*, 1995, **36**, 8457–8460.

(152) T. V. Lyubimova, S. Syrbu and S. Semeikin, *Macroheterocycles*, 2016, **9**, 59–64.

(153) L. Cheng and D. A. Lightner, *Journal of Heterocyclic Chemistry*, 1998, **35**, 1325–1328.

(154) Y. Ito, N. Higuchi and M. Murakami, *Tetrahedron Letters*, 1988, **29**, 5151–5154.

(155) M. Suzuki, K. Nunami, K. Matsumoto, N. Yoneda, O. Kasuga, H. Yoshida and T. Yamaguchi, *Chemical & Pharmaceutical Bulletin*, 1980, **28**, 2374–2383.

(156) S. Berłożecki, W. Szymański and R. Ostaszewski, *Synthetic Communications*, 2008, **38**, 2714–2721.

(157) S. Kotha and S. Halder, *Synlett*, 2010, 337–354.

(158) T. D. Lash, J. R. Bellettini, J. A. Bastian and K. B. Couch, *Synthesis*, 1994, 170–172.

(159) J. M. Khurana and R. Arora, *Synthesis*, 2009, 1127–1130.

(160) P. R. Sultane, T. B. Mete and R. G. Bhat, *Tetrahedron Letters*, 2015, **56**, 2067–2070.

(161) T. Tsuji, T. Kataoka, M. Yoshioka, Y. Sendo, Y. Nishitani, S. Hirai, T. Maeda and W. Nagata, *Tetrahedron Letters*, 1979, **20**, 2793–2796.

(162) T. D. Lash, A. D. Lammer and G. M. Ferrence, *Angewandte Chemie International Edition*, 2011, **50**, 9718–9721.

(163) T. D. Lash, T. M. Werner, M. L. Thompson and J. M. Manley, *The Journal of Organic Chemistry*, 2001, **66**, 3152–3159.

(164) S. O. C. Mundle and R. Kluger, *Journal of the American Chemical Society*, 2009, **131**, 11674–11675.

(165) S. Ji, H. Guo, X. Yuan, X. Li, H. Ding, P. Gao, C. Zhao, W. Wu, W. Wu and J. Zhao, *Organic Letters*, 2010, **12**, 2876–2879.

(166) C. Zheng, S. Huang, Y. Liu, C. Jiang, W. Zhang, G. Fang and J. Hong, *Organic Letters*, 2020, **22**, 4868–4872.

(167) A. Samanta, A. Zhao, G. K. H. Shimizu, P. Sarkar and R. Gupta, *Industrial & Engineering Chemistry Research*, 2012, **51**, 1438–1463.

(168) Q. Qian, P. A. Asinger, M. J. Lee, G. Han, K. M. Rodriguez, S. Lin, F. M. Benedetti, A. X. Wu, W. S. Chi and Z. P. Smith, *Chemical Reviews*, 2020, **120**, 8161–8266.

(169) S. Amanullah, A. Singha and A. Dey, *Coordination Chemistry Reviews*, 2019, **386**, 183–208.

(170) T. C. Berto, V. K. K. Praneeth, L. E. Goodrich and N. Lehnert, *Journal of the American Chemical Society*, 2009, **131**, 17116–17126.

(171) P. Weyermann and F. Diederich, *Helvetica Chimica Acta*, 2002, **85**, 599–617.

(172) L. Xie, X.-P. Zhang, B. Zhao, P. Li, J. Qi, X. Guo, B. Wang, H. Lei, W. Zhang, U.-P. Apfel and R. Cao, *Angewandte Chemie International Edition*, 2021, **60**, 7576–7581.

(173) J. Ma Pedrosa, C. M. Dooling, T. H. Richardson, R. K. Hyde, C. A. Hunter, M. Teresa Martín and L. Camacho, *Journal of Materials Chemistry*, 2002, **12**, 2659–2664.

(174) S. T. Kostakoğlu, Y. Chumakov, Y. Zorlu, A. E. Sadak, S. Denizaltı, A. G. Gürek and M. M. Ayhan, *Materials Advances*, 2021, **2**, 3685–3694.

Appendix A

Table A.1: Crystal data and structure refinement for **Zn_3(BDC)** and **Zn_2Mn(BDC)**.

Compound	**Zn_3(BDC)**	**Zn_2Mn(BDC)**
Formula	$Zn_{1.5}C_{16.06}O_{8.03}S_{2.03}$	$Zn_{1.13}Mn_{0.37}C_{16}O_8S_2$
Temperature (K)	293	293
Radiation	CuKα	MoKα
Crystal system	Monoclinic	Monoclinic
Space group	P 2_1/n	P 2_1/n
a (Å) **b (Å)** **c (Å)**	14.5440(3) 9.56596(19) 14.7448(2)	14.2342(4) 10.5319(2) 14.3483(4)
α (°) β (°) γ (°)	90 101.8724(17) 90	90 112.084(3) 90
Volume (Å^3)	2007.52(7)	1993.19(10)
Z	4	4
ρ_{calc} (g cm^{-3})	1.603	1.594
μ (mm^{-1})	4.665	1.853
GOF on F^2	2.0275	1.6832
θ range for data collection (°)	3.888–79.569	2.467–34.629
Index ranges	$-18 \leq h \leq 18$ $-11 \leq k \leq 11$ $-18 \leq l \leq 18$	$-21 \leq h \leq 20$ $-13 \leq k \leq 13$ $-20 \leq l \leq 20$
Reflections collected	46631	61522
Independent reflections	4297 [$R_{int} = 0.123$]	5414 [$R_{int} = 0.102$]
Data/restraints/ parameters	3408/61/343	4139/30/251
Largest diff. peak and hole (e Å^{-3})	0.95, −0.89	1.66, −1.27
Final R indices [I$\geq 2\sigma$(I)]	$R_1 = 0.0879$ $wR_2 = 0.1918$	$R_1 = 0.0847$ $wR_2 = 0.1847$
Final R indices [all data]	$R_1 = 0.1002$, $wR_2 = 0.2003$	$R_1 = 0.0990$, $wR_2 = 0.2002$